https://doi.org/10.5194/acp-2020-1158
Preprint. Discussion started: 2 December 2020

Atmospheric Chemistry and Physics Discussions

In-Situ observation of New Particle Formation in the upper troposphere / lower stratosphere of the Asian Monsoon Anticyclone

Ralf Weigel[1], Christoph Mahnke[2, 8], Manuel Baumgartner[1,3], Antonis Dragoneas[1,2], Bärbel Vogel[4], Felix Ploeger[4], Silvia Viciani[5], Francesco D'Amato[5]; Silvia Bucci[6], Bernard Legras[6], Beiping Luo[7], and Stephan Borrmann[1, 2]

[1]Institut für Physik der Atmosphäre, Johannes Gutenberg Universität, Mainz, Germany
[2]Partikelchemie, Max-Planck-Institut für Chemie, Mainz, Germany
[3]Zentrum für Datenverarbeitung, Johannes Gutenberg University, Mainz, Germany
[4]Institute of Energy and Climate Research (IEK-7), Forschungszentrum Jülich, Jülich, Germany
[5]National Institute of Optics - National Research Council (CNR-INO), Florence, Italy
[6]Laboratoire de Météorologie Dynamique, UMR 8539, CNRS – École Normale Spérieure / Université Pierre et MarieCurie / École Polytechnique, Paris, France
[7]Swiss Federal Institute of Technology, Institute for Atmospheric Science, ETH Zurich, Switzerland
[8]now at the Institute of Energy and Climate Research (IEK-8), Forschungszentrum Jülich, Jülich, Germany

Correspondence to: R. Weigel (weigelr@uni-mainz.de)

Abstract

During the monsoon season of the year 2017 the airborne StratoClim mission took place in Kathmandu, Nepal with eight mission flights of the M-55 *Geophysica* in the upper troposphere / lower stratosphere (UT/LS) of the Asian Monsoon Anticyclone (AMA) over northern India, Nepal and Bangladesh. More than hundred events of New Particle Formation (NPF) were observed. In total, more than two hours of flight time were spent under NPF conditions as indicated by the abundant presence of ultrafine aerosols, i.e. with particle diameters d_p smaller than 15 nm, which were *in-situ* detected by means of condensation nuclei counting techniques. Mixing ratios of ultrafine particles (n_{uf}) of up to ~ 50000 mg^{-1} were measured at heights of 15 – 16 km ($\theta \approx 370$ K). NPF was most frequently observed at ~ 12 - 16 km altitude ($\theta \approx 355 – 380$ K) and mainly below the tropopause , but n_{uf} remained elevated (~ 300 – 2000 mg^{-1}) up to altitudes of ~ 17.5 km ($\theta \approx 400$ K) while under NPF conditions the fraction (f) of submicrometre-sized non-volatile particle residues ($d_p > 10$ nm) remained below 50 %. At ~ 12 - 14 km ($\theta \approx 355 – 365$ K) the minimum of f (< 15 %) was found, and underneath the median f generally remains below 25 %. The persistence of particles at ultrafine sizes is limited to a few hours, mainly due to coagulation, as demonstrated by a numerical simulation. Thus, NPF is detectable only for a limited period of time and the frequency of NPF events observed during StratoClim 2017 underlines the importance of the UT/LS within the AMA as a source region for aerosols. The effective *in-situ* production of aerosol in the tropopause region and subsequent coagulation and/or condensation likely contribute to the formation and maintenance of the Asian Tropopause Aerosol Layer (ATAL). The observed abundance of NPF-produced ultrafine particles

https://doi.org/10.5194/acp-2020-1158
Preprint. Discussion started: 2 December 2020

Atmospheric Chemistry and Physics Discussions

within the AMA is not unambiguously attributable to (a) specific source regions in the boundary layer (according to backward trajectory analyses), or (b) the direct supply with precursor material by convective updraught (from correlations of NPF with carbon monoxide), or (c) the recent release of NPF-capable material from the convective outflow (according to air mass transport times in the TTL). Temperature anomalies of more than one Kelvin, as observed with a wavelength of ~ 90 km during a level flight over several hours, could be associated with the NPF process as a possible cause for the increasing supersaturation of the NPF precursor system. The frequency of NPF observed during StratoClim 2017 exceeds all previous NPF detections with COPAS at TTL levels over Brazil, Northern Australia, or West Africa. The observed NPF abundance and productivity of fresh aerosols during StratoClim 2017 indicates that NPF is capable of directly affecting the extent and persistence of the ATAL.

1. Introduction

Aerosol particles in the upper troposphere / lower stratosphere (UT/LS) influence the radiative balance of the Earth's atmosphere, stratospheric ozone chemistry, and properties of cirrus clouds near the tropopause (Kremser et al., 2016). UT/LS aerosols are mainly composed of sulphuric acid (H_2SO_4), nitric acid (HNO_3), water (H_2O), and organic compounds. Additionally, the particles include fractions of non-volatile (or refractory) material (e.g. Murphy et al. (1998); Murphy et al. (2006); Curtius et al. (2001); Heald et al. (2005); Froyd et al. (2010); Borrmann et al. (2010); Murphy et al. (2014); Schneider et al. (2020)). Non-volatile components of stratospheric aerosol particles originate from (1) natural tropospheric sources, e.g., volcanoes, biomass burning, or pyro-cumulonimbus, (2) from meteoric ablation, or (3) they are anthropogenic, as, for instance, space debris, rocket exhaust fumes, and products from combustion (Kremser et al. (2016)). Chemical and microphysical processes, which involve the stratospheric aerosol, could be influenced by solutes that, e.g., had previously been constituents of the refractory aerosol compounds. Soot, mineral dust, aerosol from biomass combustion, meteoric ablation material, inorganic salts, and other species probably make up the largest share of the non-volatile components of aerosol particles in the UT/LS. In the tropics, underneath the tropopause, the number of non-volatile fine-mode particles (i.e. smaller than 1 µm and larger than 10 nm in diameter d_p) typically exhibits a characteristic minimum, resulting in a fraction of ~ 20 % (and less) of non-volatile aerosol particles (cf. Borrmann et al. (2010); Weigel et al. (2011)). Above the tropopause, at potential temperatures greater than 390 - 400 K, a maximum contribution of non-volatile aerosol constituents seldom exceeds 50 % (*ibid.*). Schneider et al.

https://doi.org/10.5194/acp-2020-1158
Preprint. Discussion started: 2 December 2020


Atmospheric Chemistry and Physics Discussions

(2020) recently provided laser ablation mass spectrometric analyses of refractory particles in the LS region between the equator and the Arctic, which indicate detectable signatures of meteoric ablation material at all sample locations in the LS. They assume that the meteoric ablation material is partly present as solute or as insoluble inclusion within stratospheric H_2SO_4-H_2O-droplets.

In general, the typical particle size distribution of the stratospheric aerosol is characterised by processes such as formation of new particles and their coagulation, the condensation of saturated vapours, and the removal from the stratosphere into the troposphere. In the tropics, above the level of zero net radiative heating where scavenging is lacking in the absence of clouds, aerosol particles are available for isentropic dispersion or upward transport into the stratosphere. Sedimentation or isentropic transport and mixing remove particles from the stratosphere (Thomason and Peter (2006); Kremser et al. (2016)). Moreover, the aerosol removal from the stratosphere occurs with particular efficiency via large-scale air mass subsidence in the polar winter vortex in both, the Arctic (Weigel et al., 2014) and the Antarctic (Campbell and Deshler, 2014).

The process of homogeneous nucleation (also known as gas-to-particle-conversion), herein referred to as New Particle Formation (NPF), is considered as one of the most important sources of the H_2SO_4-H_2O solution droplets prevailing in the UT and Tropical Tropopause Layer (TTL). The reservoir of stratospheric H_2SO_4 is maintained by oxidation of gaseous precursors like sulphur dioxide (SO_2), carbonyl sulphide (OCS), and carbon disulphide (CS_2), or Dimethyl sulphide (Thomason and Peter (2006); Kremser et al. (2016)) from sea surface emissions, from volcanism or from anthropogenic pollution, which often undergoes long range transport before reaching the TTL (e.g. Law et al., 2010). Sporadically, explosive volcanism injects large quantities of SO_2 directly into the stratosphere (Vernier et al. (2011b); Kremser et al. (2016)). Within the planetary boundary layer, SO_2 is found in mixing ratios from 20 pmol mol^{-1} to more than 1 nmol mol^{-1}. SO_2 mixing ratios of up to several hundreds of nmol mol^{-1} are found in the vicinity of cities and highly polluted areas (Seinfeld and Pandis, 2016). From the boundary layer, SO_2 can be transported very efficiently by deep convection within cumulonimbus (Cb) clouds to UT heights. Although SO_2 is efficiently bound within clouds and dissolved in cloud hydrometeors, cloud-resolving model calculations suggest that a proportion of 40-90 % of SO_2 may reach the

https://doi.org/10.5194/acp-2020-1158
Preprint. Discussion started: 2 December 2020


Atmospheric Chemistry and Physics Discussions

outflow region of deep convection (Barth et al., 2001), and these calculations are largely consistent with estimates by Crutzen and Lawrence (2000). However, other model studies (Ekman et al., 2006) show that only 30 % of SO_2 from the boundary layer reaches the cloud top. Laboratory investigations by Jost et al. (2017) yielded a comparatively moderate retention coefficient (0.2 – 0.5) of SO_2 in the ice phase of clouds, compared to a retention of 100 % for hydrochloric acid (HCl) and for nitric acid (HNO_3) (*ibid.*). Hence, large fractions of the in-cloud dissolved SO_2 leave the cloud ice composite as soon as the cloud particles freeze or riming occurs. Alternatively, the SO_2, which remains in the cloud ice composite, is entirely released when the ice particles sublimate in the convective outflow region, or below, while the ice particles sediment. Crutzen and Lawrence (2000), as well as Barth et al. (2001), however, clarified that cloud's acidity determines its capacity to remove a soluble gas (such as SO_2). Results from airborne *in-situ* measurements of SO_2 at altitudes between 8 and 15 km were compiled by Thornton et al. (1999). Remote MIPAS observations were compared by Höpfner et al. (2015) with SO_2 data from *in-situ* measurements between 8 and 12 km altitude, which were carried out before the year 2001. At altitudes between 8 and 15 km, the mean values of SO_2 mixing ratio vary between 5 and 800 pmol mol^{-1} in the northern hemisphere, between 8 and 120 pmol mol^{-1} in the tropics, and between 5 and 20 pmol mol^{-1} in the southern hemisphere (Kremser et al., 2016). Enhanced SO_2 mixing ratios in the vicinity of the tropopause are often observed in connection with the uplift of polluted air masses by Warm Conveyor Belts (WBC) (*ibid.*). Apart from sulphuric acid, potentially also other species contribute to particle nucleation and growth, such as organics (Metzger et al. (2010); Kerminen et al. (2010)), amines (Kürten et al. (2018)) or ammonia (e.g. Kirkby et al. (2011); Kürten (2019)). Given the amount of organics (Murphy et al. (2006)) and ammonia species (Höpfner et al. (2019); Stroh et al. (2020)), which were found in aerosol particles at UT/TTL heights in the AMA during the StratoClim 2017 mission, such compounds very likely act as agents promoting NPF in the UT and TTL region.

1.1 New particle formation

New Particle Formation (NPF), comprises (1) the initial combination of molecules into clusters (of ~ 1 nm diameter) and (2) their subsequent growth to larger diameters (Kulmala et al., 2013). Nucleation mode (ultrafine) aerosol particles with diameter (d_p) of at least 3 nm frequently form in considerable quantities from gaseous precursors. Once formed, the particles are subject to

https://doi.org/10.5194/acp-2020-1158
Preprint. Discussion started: 2 December 2020


Atmospheric Chemistry and Physics Discussions

altering processes (e.g. coagulation, growth by condensation of water vapour and other gases, evaporation, scavenging). Within the entire atmosphere, NPF seems ubiquitous as was demonstrated by various studies and observations of NPF's occurrence:

- at or close to the surface (Kulmala et al. (2004); Nieminen et al. (2018)),
- at elevated altitudes within the boundary layer (e.g. Sellegri et al. (2019); Wehner et al. (2015), Crumeyrolle et al. (2010); Venzac et al. (2008)),
- in the boundary layer and in the free troposphere under the direct influence by volcanic activity (e.g. Sahyoun et al. (2019)),
- up to tropopause altitudes and the TTL region (Kerminen et al. (2018); Williamson et al. (2018); Williamson et al. (2019).

Modelling studies suggest that the NPF process constitutes one of the most important contributions (up to 45 %) to global mean tropospheric concentrations of Cloud Condensation Nuclei (CCN) activated at 0.2 % supersaturation (Merikanto et al., 2009). Uncertainties remain concerning the effectiveness of NPF, which complicates the implementation of the NPF mechanism in global scale simulations of aerosol number densities (Yu et al. (2010), Zhang et al. (2010)). Chamber experiments, conducted at temperatures similar to those prevailing in the UT, and numerical simulations also confirm that the UT constitutes an important source region for atmospheric particles (Kürten et al. (2016), Dunne et al. (2016)).

Based on airborne in-situ observations of high particle number concentrations together with high levels of particle volatility in the cloud-free tropical UT, the conditions of NPF occurrence were described for the first time by Brock et al. (1995). Between 7 and 20 km altitude, fields of recent NPF events were encountered in about 20 % of the probed flight segments (Lee et al. (2004)). NPF of largest intensity was observed particularly at the bottom TTL, as shown by airborne measurements during missions over Brazil and over North Australia (Weigel et al. (2011)). Recently, a survey of NPF occurrence in the free troposphere (~ 0.2 - 12 km altitude) suggests that the NPF-produced particles persist (zonally almost invariant) as a globally extending band within the tropical UT, thereby covering 40 % of the Earth's surface (Williamson et al., 2019).

https://doi.org/10.5194/acp-2020-1158
Preprint. Discussion started: 2 December 2020


Atmospheric Chemistry and Physics Discussions

All NPF observations, which were made during the StratoClim 2017 mission in the UT and TTL region at altitudes of up to 20 km in the Asian Monsoon Anticyclone, are discussed in their entirety within this study. The specific differentiation of NPF data is provided in Weigel et al. (2020b) where NPF encounters in the presence of cloud ice particles are separately studied and where it is shown that NPF proceeds largely unaffected by the faint ice clouds typically occurring in the TTL.

1.2 The StratoClim 2017 field campaigns in the Asian Monsoon Anticyclone

Between 27 July and 10 August 2017, during the Asian monsoon season, a total of eight scientific flights with the high-altitude research aircraft M-55 *Geophysica* over parts of the Indian subcontinent were performed from Kathmandu, Nepal (27° 42' 3'' N, 85° 21' 42'' E) during the StratoClim 2017 mission (see Figure 1, and see also Stroh et al. (2020)). Some of these flights partly spanned out of Nepalese airspace, to East India, Bangladesh, and to the northern part of the Bay of Bengal.

The Asian Monsoon Anticyclone (AMA) represents one of the most important circulation systems, mostly associated with deep convection, which mainly determines the circulation in the UT/LS during the monsoon season over the Indian subcontinent. From the beginning of June until about the end of August, the large-scale anticyclone persists at altitudes from the UT to the LS regions (e.g. Randel and Park (2006), Park et al. (2007)), extending over longitudes from East Asia to the Middle East/ East Africa (e.g. Vogel et al. (2014), Vogel et al. (2019)). The anticyclonic rotation of the system induces a horizontal transport barrier inside the UT/LS (Ploeger et al. (2015)), which abates the isentropic exchange between the AMA's interior and its surrounding. Air masses in the region of the Asian monsoon are rapidly lifted by convection up to the maximum level of convective outflow (~ 360 K, corresponding to ~ 13 km) followed by a slow diabatic lift superimposed on the anticyclonic motion (e.g. Vogel et al. (2019)). This mechanism transports young air to UT/LS altitudes during boreal summer and in this way various pollutants and other gaseous material (Glatthor et al. (2015); Chirkov et al. (2016); Pan et al. (2016); Santee et al. (2017)) and in particular water vapour (Ploeger et al. (2013)) are lifted into the UT/LS region within the AMA. Based on satellite studies, the existence of the aerosol layer at tropopause altitudes within the AMA region (ATAL – Asian Tropopause Aerosol Layer) was proven and investigated (Vernier et al. (2011a); Thomason and Vernier (2013)). The existence

https://doi.org/10.5194/acp-2020-1158
Preprint. Discussion started: 2 December 2020


Atmospheric Chemistry and Physics Discussions

of the ATAL is further confirmed by in situ balloon-borne backscatter measurements (Vernier et al. (2015); Vernier et al. (2018); Brunamonti et al. (2018); Hanumanthu et al. (2020)) in Lhasa (August 2013), Saudi Arabia (August 2015) and India (August 2016, 2017) as well as recently by aircraft measurements of Mahnke et al. (2020).

Hence, the constituents of the rising young air may also include precursor material from anthropogenic (Vernier et al. (2015), Yu et al. (2015)) and other sources, which maintain the observed ATAL. The NPF process in the TTL region could contribute significantly to the formation and persistence of ATAL as a source of additional aerosol material (He et al., 2019). Once the boundary layer material has reached UT/LS levels within the AMA, the elevated tropopause potential temperature during the monsoon season allows the material's isentropic dispersion into the "overworld" stratosphere (Pan et al. (2016)). Thereby, it is under debate whether the upward transport is best described with the model of a draughting "chimney" or of a pushing "blower" (Pan et al. (2016)). However, three-dimensional simulations with the Chemical Lagrangian Model of the Stratosphere (CLaMS) and backward trajectory analyses show that by end of August, during the 2008 monsoon season, comparatively young air masses (younger than 6 months) reach the top of the AMA at about 460 K potential temperature (corresponding to ~ 60 hPa). According to these simulations (Vogel et al. (2019)), air masses are lifted due to diabatic (mainly radiative) heating in an anticyclonic large-scale upward spiral with ascent rates of about 1 K potential temperature per day. The anticyclonic lift of air in the AMA occurs across the tropopause while elsewhere, in the extra-tropics, the tropopause typically acts as an obstacle for the immediate vertical transport (Vogel et al. (2019)). This capability of the tropopause to cap the troposphere seems largely diminished in connection with the AMA (*ibid.*), and is consistent with the conclusions of previous works (Bergman et al. (2012), Garny and Randel (2016), Ploeger et al. (2017)).

2 *In-situ* instrumentation

2.1 Total number concentration of sub-micrometre sized particles

Particle number concentrations were *in-situ* measured by means of a 4-channel condensation nuclei (CN) counter COPAS (COndensation PArticle counting System, cf. Weigel et al. (2009)) with continuous flow, using the chlorofluorocarbon FC-43 as working fluid. COPAS

https://doi.org/10.5194/acp-2020-1158
Preprint. Discussion started: 2 December 2020


Atmospheric Chemistry and Physics Discussions

measurements and data storage are performed at a frequency of 1 Hz. To reduce the statistical noise of the directly recorded raw signal of the scattered-light-detectors integrated in COPAS, the 1 Hz-raw data are preprocessed by applying a 15-second running average. Three of the four COPAS channels operate with different 50 % detection particle diameters d_{p50} (i.e. 6 nm, 10 nm and 15 nm). The fourth COPAS channel (with d_{p50} = 10 nm) detects particles downstream of a heated (270°C) sample flow line, resulting in measured particle mixing ratios of non-volatile (nv) or refractory particles (e.g. soot, mineral dust, metallic aerosol material, etc.).

2.1.1 COPAS operation during StratoClim 2017

The forward facing aerosol inlet of COPAS is located well outside the boundary layer of the aircraft. The inlet consists of two serial diffusers, which slow down the ambient air velocity to the flow speed of the instruments' sampling. For stratospheric particle concentrations, the COPAS measurement uncertainty of the StratoClim 2017 data discussed herein is about 15%, which is due to particle counting statistics and uncertainties in the volume flow. The measurement properties of COPAS are described in detail by Weigel et al. (2009), and its performance has been demonstrated by several studies (Curtius et al. (2005); de Reus et al. (2009); Borrmann et al. (2010); Frey et al. (2011); Weigel et al. (2011), and Weigel et al. (2014)). Compared to previous missions (*ibid.*), during StratoClim 2017 a new inlet configuration was required, which caused both COPAS instrument units to sample via a single aerosol inlet.

The coupled sampling flow through one common inlet bears the advantage of an increased super-isokinetic flow ratio at the inlet's entry as compared to previous operations. This way the flow speed through commonly used parts of the aerosol line setup is almost doubled, which effectively reduces diffusional particle loss (cf. Weigel et al. (2009)). However, this new instrument setup required a reanalysis of the corrections to account for particle loss as compared to the previous values documented in (Weigel et al. (2009)). Equivalently to the previously described procedure (*ibid.*), the pressure-dependent corrections for the used aerosol lines and given volume flows were re-calculated (Table 1) using the method introduced by von der Weiden et al. (2009) with modifications for low-pressure application. These corrections are applied to the number densities of particles in the ultrafine size mode (cf. Section 2.1.3).

The particle densities are typically measured by COPAS in particle number concentrations N (in cm^{-3}), but are also presented here as mixing ratio n in units of particles per milligram of ambient

https://doi.org/10.5194/acp-2020-1158
Preprint. Discussion started: 2 December 2020


Atmospheric Chemistry and Physics Discussions

air (mg^{-1}). This way the measurements from different pressure levels are consistently comparable and allow direct correlations between the mixing ratios of particles and of gaseous tracers. Hereafter, the notation n_{10} refers to the mixing ratio of sub-micrometre sized particles with diameters greater than 10 nm. The measurement of n_6 (of particles with $d_p > 6$ nm) and n_{15} ($d_p > 15$ nm) aims at the identification of recent NPF (cf. Section 2.1.3). The notation n_{10}nv refers to the mixing ratio of non-volatile particles with identical size range as specified for n_{10}. The proportion f of non-volatile particles is given as the ratio of n_{10}nv and n_{10} in percent (equivalently determined from the ratio of the measured number concentrations N_{10}nv and N_{10}), since only non-volatile particles with sizes $d_p > 10$ nm are detected (Section 2.1.2).

2.1.2 COPAS detection of non-volatile (refractory) aerosol particles

COPAS includes a denuder-type device based on an established and commonly used technique for exposing atmospheric aerosol samples to heat in order to obtain indications concerning the chemical properties a) of the volatile compounds of aerosol particles (when analysed e.g. by gas chromatography) or b) of the remnants, which survive the heat exposure. One of the four COPAS channels is equipped with a heated stainless steel tube, which is used to vaporise volatile compounds upstream of one of the particle detectors. In this way, the preheated COPAS channel detects the residual aerosol component by number per sample volume. The particles that remain after passing through the heated tube (at ~ 270°C) are considered and designated hereafter as non-volatile (or refractory) at given temperature (see Curtius et al. (2005), Weigel et al. (2009), and Borrmann et al. (2010)). The specific heating temperature is chosen with the aim to vaporise mainly stratospheric particle species, which typically consist of aqueous solutions of sulfuric acid (H_2SO_4-H_2O) and/or nitric acid (HNO_3-H_2O), which reportedly volatilise at 180°C (Rosen, 1971). In addition, most of volatile and several semi-volatile organic compounds can evaporate at temperatures below 270°C.

The working principle of the COPAS aerosol vaporiser was demonstrated by means of laboratory experiments with pure H_2SO_4-H_2O particles of several sizes and at pressure conditions between 70 – 300 hPa (Weigel et al., 2009); more than 98 % of the sub-micrometre sized H_2SO_4-H_2O particles were volatilised. As refractory material, which could be detectable with COPAS, is unlikely to be generated by the heater itself, instrumental artefacts may be excluded as a potential cause of false observation. To avoid artefacts as a result, e.g., of re-suspension of

https://doi.org/10.5194/acp-2020-1158
Preprint. Discussion started: 2 December 2020


Atmospheric Chemistry and Physics Discussions

aerosol material, which had been deposed on the tube's inner walls during previous operations, the sample lines were flush-cleaned with ethanol and distilled water, at least before every second mission flight. Inefficiencies of the vaporiser, e.g. due to diminished heat transfer from the tube's inner wall to the passing aerosol particles, particularly at low atmospheric pressures, would cause the number (fraction) of detected refractory particles to be unexpectedly high ($f \approx 100$ %) over extended measurement periods, which was not observed throughout the field missions (cf. Borrmann et al. (2010); Weigel et al. (2011)). Conversely, instrumental artefacts inherent with the vaporiser's tube length, e.g. particle loss, would lead to comparatively low number concentrations of detected refractory particles. Diffusional loss effects increase with decreasing pressure, but thermophoresis should counteract the particles' diffusion towards the hot tube walls. With the same vaporiser system, Weigel et al. (2014) observed rising mixing ratios of refractory aerosol, most likely from meteoric ablation, with altitude at stratospheric levels inside the polar vortex, while outside the vortex the amount of refractory aerosols nearly stagnated over the corresponding altitude range. This may additionally confirm the principle function of the vaporiser.

2.1.3 NPF criterion and event definition

To serve as an indication of recent NPF (within hours prior to the observation), the number concentration of ultrafine aerosol particles (hereafter referred to as N_{uf}) results from the difference N_6 - N_{15} = $N_{6\text{-}15}$, which moreover requires meeting the NPF criterion:

$$0.8 \cdot N_6 - 1.2 \cdot N_{15} > 0\,. \qquad (1)$$

This criterion was reassessed for the StratoClim 2017 data set based on the definition used by Weigel et al. (2011) to account for the COPAS detectors' signal-to-noise ratio and the counting statistics. The NPF criterion therefore sets a conservative threshold (*ibid.*) to take an overall uncertainty of up to 15 % of the individual COPAS channels into account. Resulting $N_{6\text{-}15}$ are then subject to corrections concerning particles' diffusional loss inside the aerosol lines as described in Section 2.1.1 (cf. also Table 1). The calculated number concentrations $N_{6\text{-}15}$ were multiplied by the correction factor κ_L (Table 1) being a function of static pressure during the measurements.

Provided that the NPF criterion is met, a series of measurement points is denoted as an event if the measured number concentration (or mixing ratio) of ultrafine particles remains

https://doi.org/10.5194/acp-2020-1158
Preprint. Discussion started: 2 December 2020


Atmospheric Chemistry and Physics Discussions

continuously greater than zero for at least 5 measurement seconds. Limitations of this event definition concern observations, which lasted over time periods between one and five seconds. Overall, 25 cases of a total of 130 individually encountered events are affected by this instance. Specifications such as the number of newly formed particles and the duration of such short events is uncertain: too short signal features (e.g. over one second) and thus fine spatial structures are smoothed by the data pre-processing or filtered out by applying the NPF criterion. Note, during one second the measurement platform has moved a horizontal distance of ~ 150 m and a vertical distance of up to ~ 10 m assuming cruising speed and a maximum ascent/descent rate of 10 m s^{-1}. Based on the mean flight speed of the M-55 *Geophysica* (~ 154 ± 39 m s^{-1}), this definition implies that an event (i.e. elevated N_{uf} for more than 5 seconds) covers a horizontal distance of ~ 770 m (into flight direction of a straight heading). The corresponding event definition applies also for investigations concerning the occurrence of NPF in the presence of cloud ice elements during the StratoClim 2017 mission (see Weigel et al. (2020b)).

The time period during which the event criterion (Equation 1) is fulfilled, i.e. during which the number of ultrafine particles remains at significantly elevated levels, is referred to hereafter as the NPF event duration. From this primary information of measured data, the horizontal extent of NPF fields is derivable with caveats. On the one hand, such estimates are limited by the assumption that an encounter of elevated N_{uf} (over tens of seconds and minutes) is actually due to a single NPF event and does not consist of a series of possibly overlapping events. On the other hand, the determined horizontal distances refer to the average flight speed (~ 154 ± 39 m s^{-1}) and the flight attitude is assumed as unchanged during the event duration.

Hereafter, an NPF event is denoted as *elevated* if detected aerosol densities of ultrafine particles exceed 10000 mg^{-1}. The terms *intermediate* or *weak* NPF are used in connection with number densities of particles in the ultrafine size mode in the range of 1000 $mg^{-1} < n_{uf} < 10000$ mg^{-1} or < 1000 mg^{-1}, respectively. This classification refers to laboratory studies by (Kirkby et al. (2011), Kürten et al. (2016)); according to these the NPF-rate and, hence, the NPF intensity (i.e. its new particle productivity) varies with the degree of supersaturation of the vapour from which the new particles form. However, it should be noted that hereafter the notation *most intense* NPF, i.e. events of particularly increased ultrafine particle production, is often used synonymously with *most recent* NPF. Due to the short persistence of the freshly formed particles in the ultrafine size

https://doi.org/10.5194/acp-2020-1158
Preprint. Discussion started: 2 December 2020


Atmospheric Chemistry and Physics Discussions

mode (cf. Section 4.5), an intense NPF event is still proceeding when observed, or it had phased-out very recently (within hours) before the detection. For NPF encounters with low or intermediate n_{uf}, the conclusions concerning the event's age remain ambiguous.

2.2 The Ultra-High Sensitive Aerosol Spectrometer UHSAS-A

The measurements of the aerosol particle size distributions during the StratoClim 2017 field campaign (Höpfner et al. (2019); Stroh et al. (2020)) were performed with an in-house modified airborne version of the Ultra High Sensitive Aerosol Spectrometer (UHSAS-A; manufacturer DMT Inc., Longmont, CO, USA). The modifications made to the flow and pumping system of the UHSAS-A enabled maintaining constant system-flows (sample-, sheath-, purge-flow) through the instrument even under ambient (stratospheric) pressures as low as 50 hPa. The airflow system of the UHSAS-A was characterised and calibrated in the laboratory prior to the StratoClim 2017 field campaign using a controlled low-pressure chamber. The size binning of the aerosol particle size distributions results from instrument's laboratory characterisations with size-classified particles (by means of a Differential Mobility Analyzer; DMA), such as Polystyrene Latex (PSL), Sodium Chloride, Ammonium Nitrate and Ammonium Sulfate. The particle sizing performance of the UHSAS-A throughout the field campaign was monitored by means of calibrations prior to each mission flight. For these calibrations, exclusively PSL particle standards were used. The uncertainty of the number concentration measured by the UHSAS-A with 1-Hz resolution was determined to be approximately 10 % for the particle diameter range of 65 nm < d_p < 1000 nm. This uncertainty is based on laboratory characterisations of the sample-flow measurement and of the counting efficiency of the instrument (Mahnke et al., 2020). Some of the results from the measured particle size distributions and a comparison with other instruments and the Cloud-Aerosol Lidar with Orthogonal Polarization (CALIOP) are also presented by Mahnke et al. (2020).

2.3 Carbon monoxide measurements

At tropospheric altitudes, the role of carbon monoxide (CO) is understood as a pollutant (Park et al. (2009)), thus, CO is often used as a representative pollution tracer (e.g. Pan et al. (2016)). The main sources of CO are natural as well as anthropogenic, including combustion, and the conversion from hydrocarbons due to oxidation. The entire tropospheric CO budget is assumed

https://doi.org/10.5194/acp-2020-1158
Preprint. Discussion started: 2 December 2020

Atmospheric Chemistry and Physics Discussions

to be maintained almost equivalently by: (1) its photochemical production and (2) its emission from ground sources. The atmosphere's CO content is mainly depleted via oxidation with hydroxyl radical (OH) (Logan et al. (1981), Seinfeld and Pandis (2016)). The CO's atmospheric lifetime is comparatively short and ranges at about two to three months (Zahn et al. (2002); Hoor et al. (2004); Hoor et al. (2005)). CO is frequently used as tropospheric tracer for investigations concerning the air mass transport in the troposphere, across the tropopause, and in the lowermost stratosphere. In the free troposphere, CO mixing ratios typically range between 50 nmol mol^{-1} (unpolluted) and values of up to 700 nmol mol^{-1} (polluted) next to emission sources (Clerbaux et al. (2008), Park et al. (2009)). CO mixing ratios remain comparatively high ($\gtrsim$ 100 nmol mol^{-1}) within the AMA and up to altitudes of ~ 15 km. Between 15 km and 20 km altitude, CO mixing ratios gradually decrease down to ~ 40 nmol mol^{-1} (Park et al. (2009)).

During the StratoClim 2017 mission, CO mixing ratios were determined by means of the tunable diode laser (TDL) detection principle, which the analyser Carbon Oxide Laser Detector-2 (COLD-2) spectrometer is based on. According to comprehensive comparisons to the previous instrument version COLD (Cryogenically Operated Laser Diode, 4 s temporal resolution, (Viciani et al., 2008)), the new system implies several improvements (Viciani et al., 2018). The laser source is now a room temperature Quantum Cascade Laser (QCL) that no longer requires a liquid nitrogen cooling, which also reduces size, weight and operational complexity. The measurement's temporal resolution is improved by a factor of four, the in-flight sensitivity of the COLD-2 spectrometer ranges at about 2 nmol mol^{-1} at integration times of 1 s, and an accuracy of 3 % is specified for the CO measurement with COLD-2 (Viciani et al., 2018).

2.4 Meteorological measurements

Atmospheric temperature and pressure data were taken from the Unit for Connection with the Scientific Equipment (UCSE, Sokolov and Lepuchov (1998)), which is a part of the navigational system of the M-55 *Geophysica*. UCSE data are available as 1-Hz-resolved ambient pressure (accuracy: ± 1 hPa) and temperature (± 2 K accuracy). Based on these UCSE data, the potential temperature θ along the mission flight tracks is calculated in compliance with the definition by the World Meteorological Organization (WMO (1966)).

https://doi.org/10.5194/acp-2020-1158
Preprint. Discussion started: 2 December 2020


Atmospheric Chemistry and Physics Discussions

3 Analytical methods

3.1 The height of the lapse-rate tropopause and the equivalent latitude

Meteorological data were also taken from ERA-Interim reanalyses by the European Centre of Medium-Range Weather Forecasts (ECMWF) (Dee et al., 2011). Hybrid reanalysis levels in the TTL are located at various pressure heights (i.e. around 177, 154, 133, 113, 96, 80, 67, 55 hPa, respectively) representing a vertical resolution of about one kilometre in this region.

The aircraft data are analysed in coordinates relative to the tropopause height and to the monsoon anticyclone center, respectively. The height of the lapse-rate based thermal tropopause was determined based on ERA-Interim data and following the WMO criterion (WMO, 1957) as the lowest altitude (z_0) where the temperature lapse-rate falls below 2 K km^{-1}, if the average lapse-rate within an overlying layer of 2 km thickness (i.e. z_0+2 km) remains below 2 K km^{-1}. The cold point tropopause definition often yielded ambiguous results for the tropopause heights within the AMA for the StratoClim 2017 period (cf. von Hobe et al. (2020)). The potential temperature at tropopause level was interpolated to the 1-Hz-resolved position along the flight track of the M-55 *Geophysica*, and the measurement data were sorted as a function of potential temperature distance to the local tropopause as vertical coordinate.

The centre of the AMA was determined based on the anomalous potential vorticity distribution within the monsoon region at the 380 K potential temperature level, where lowest values of the potential vorticity (PV) are found in the AMA centre. For that reason, the AMA-centred equivalent latitude was calculated for a given closed PV contour as a projection onto polar coordinates (Ploeger et al., 2015). Therefore, an equivalent latitude of 90° North corresponds to the center of the anticyclone (lowest PV), and the equivalent latitude decreases with increasing distance from the centre, or rather, towards the anticyclone's edge. Note, that the calculation of AMA-centred equivalent latitude is rigorously valid within a layer of about ± 10 K around 380 K potential temperature, where a clear negative PV anomaly occurs. The uncertainties of calculated equivalent latitude become significant at levels beyond the ± 30 K range above/below 380 K.

https://doi.org/10.5194/acp-2020-1158
Preprint. Discussion started: 2 December 2020

Atmospheric Chemistry and Physics Discussions

3.2 The Coagulation Model for investigating the particles' persistence in the ultrafine size mode

Particle coagulation comprises the processes of particle collisions and their subsequent coalescence. More specifically, if two particles with masses m_i and m_j collide and coalesce, a new particle with mass $m_i + m_j$ is formed. The coagulation rate of particles with masses m_i and m_j is described by $\beta_{i,j}\, n_i\, n_j$, where n_i and n_j are the number concentrations of particles with masses m_i and m_j, respectively. The coagulation kernel $\beta_{i,j}$ characterises the coagulation rate. The choice of the coagulation kernel depends on the type of coagulating particles, in particular, on their size. Coagulation of ultrafine aerosol particles is sufficiently well described by a Brownian coagulation kernel (Jacobson (2005), Equation 15.33 therein). The kernel includes a correction term to account also for particles in the transition regime, i.e. the transition between the free-molecular regime, where the particles are small compared to their mean free path, and the continuum regime, where the particles are large compared to their mean free path.

The model employed in this study numerically solves the discretised coagulation equation (cf., e.g., Jacobson (2005) and Equation 15.2 therein) as formulated in the numerical chemistry-climate model SOCOL (SOlar Climate Ozone Links; Stenke et al. (2013)). The particles are assumed as spherical, and the model is based on a discretisation of the volume space, wherein the ratio of two subsequent volume size bins is constant, $\frac{V_{k+1}}{V_k} = 1.4$. The particle size range of the first volume size-bin V_1 corresponds to particle diameters of 7.5 nm < $d_{p,1}$ < 8.5 nm. With a total number of 40 size bins, hence the largest particle size included in this investigation is about 635 nm ($= d_{p,40} = (1.4)^{\frac{39}{3}} \cdot d_{p,1}$).

The coagulation rate and, thus, the persistence of the ultrafine particles, was simulated under given background conditions during observation. As input for the simulation, the aerosol size distribution detected by the UHSAS-A (nominally covering 65 nm < d_p < 1000 nm, cf. Section 2.2 and Mahnke et al. (2020)) was extended towards smaller diameters by further particle size bins obtained from the measurements with COPAS. For this case study, the NPF event on 04 August 2017 (KTM 5) over 26 seconds between 04:04:40 and 04:05:06 UTC (pressure altitude: 110 hPa; ambient air temperature: 196 K) was selected. The detection ranges of three COPAS channels determine two regimes in the ultrafine size mode, i.e. 6 nm < d_p < 10 nm and 10 nm < d_p < 15 nm,

https://doi.org/10.5194/acp-2020-1158
Preprint. Discussion started: 2 December 2020

Atmospheric Chemistry and Physics Discussions

each of which are divided into three sub-bins, to exploit a higher particle size resolution of the coagulation model. The three sub-bins within the size classes 6 – 10 nm and 10 – 15 nm were uniformly set to one third of the respective concentration $N_{6\text{-}10}$ (~ 10000 cm^{-3}) and $N_{10\text{-}15}$ (~ 3600 cm^{-3}). The difference between the total number concentrations N_{15} (COPAS) and N_{65} (UHSAS-A) yields the number concentration of $N_{15\text{-}65}$. The number concentration $N_{15\text{-}65}$ (~ 5000 cm^{-3}) was interpolated over 13 sub-bins (with exponential degradation on increasing particles size) to achieve a continued transition of the size distribution towards the detection size range of the UHSAS-A. The size-segregated aerosol concentrations measured with the UHSAS-A were interpolated (with respect to particle size) to the resolution of the remaining 21 sub-bins of the coagulation simulation. The particle concentrations $N(d_p)$ over the entire particle size range from the ultrafine sizes to up to $d_p = 1$ µm were converted into an aerosol size distribution $\mathrm{d}N / \mathrm{d}\log d_p$ in cm^{-3} as a representation of an initial state and input for the coagulation simulation (for more details see the results in Section 4.5).

It is worth noting, that for the coagulation simulation, the NPF event is considered as expired, i.e. any fresh supply of ultrafine particles due to continuous or renascent NPF is excluded for the simulated runtime of the coagulation process over 24 hours. Generally, constant conditions of atmospheric pressure (p) and temperature (T) are assumed over the 24-hours period for the simulation, as the air is lifted very slowly at TTL levels within the AMA (by ~ 1 K potential temperature per day, cf. Vogel et al. (2019), corresponding to $\Delta p \approx$ 1-1.5 hPa and $\Delta T < 1$ K per day). However, for atmospheric layers where convective dynamics and air mass mixing are still effective, the assumption of constant ambient conditions may not hold for such simulations.

3.3 Analyses of trajectories and the air mass transport history

Fifty – days backward trajectories were calculated for each sample collected during the StratoClim 2017 mission using the trajectory module of the Chemical Lagrangian Model of the Stratosphere (CLaMS; McKenna et al. (2002), Konopka et al. (2012), Pommrich et al. (2014)). The CLaMS backward trajectory calculations are driven by horizontal winds and are based on the new high-resolution ERA-5 reanalysis (Hersbach and Dee (2016)) which was recently released by the ECMWF. The improved resolution of the ERA-5 data compared to the ERA interim data set should increase the reliability of tropospheric transport processes along the backward trajectory analysis and may strengthen the assignment to possible source regions.

https://doi.org/10.5194/acp-2020-1158
Preprint. Discussion started: 2 December 2020


Atmospheric Chemistry and Physics Discussions

481 ERA-5 data are given on a horizontal grid of about 0.3° × 0.3° , in 1-hour temporal resolution, in
482 137 hybrid levels from the surface to the 0.01 hPa pressure altitude. Hence, a much better
483 representation of convective updraught and tropical cyclones is realised with the ERA-5 dataset
484 (Hoffmann et al. (2019)) compared to earlier reanalyses (Dee et al. (2011)), in particular, in the
485 region of the Asian summer monsoon (Li et al. (2020)). However, further validation of the ERA-5
486 products is required, thus ERA-Interim reanalyses still represent the state-of-the-art.

487 For vertical air mass transport velocities, the diabatic approach was applied using the total
488 diabatic heating rate to extract the vertical velocity, thereby including the release of latent heat
489 (for details, see (Ploeger et al., 2010). The model boundary layer is set at ~ 2 – 3 km above the
490 surface following orography (cf. Pommrich et al. (2014), Vogel et al. (2015)).

491 In general, trajectory calculations have limitations due to trajectory dispersion depending on the
492 trajectory length. However, the frequently employed trajectory length to study transport
493 processes in the Asian monsoon region is ranging from a couple of weeks to a few months (e.g.
494 Chen et al. (2012); Bergman et al. (2013); Garny and Randel (2016); Müller et al. (2016); Li et al.
495 (2017) and Li et al. (2018)). The CLaMS trajectory products based on the ERA-5 dataset were
496 extensively investigated concerning their spatial and temporal resolution in connection with
497 strong vertical transport (e.g. Hoffmann et al. (2019)). However, Li et al. (2020) demonstrated,
498 by means of satellite-borne (FY-2D) brightness temperature data and balloon measurements in
499 China, that convective events over the Pacific Ocean associated with tropical cyclones are
500 resolved by CLaMS trajectory calculations with high accuracy.

501 The CLaMS backward trajectory calculations, which were initialized from each sampling position
502 along the flight track in 1-Hz resolution, were used to allocate the air's latest contact with the
503 model boundary layer at 2 – 3 km above the ground. This allows for investigating the location of
504 the sources influencing the mixing ratios in the air samples taken aboard the M-55 *Geophysica*.
505 To include the uncertainty of a certain backward trajectory, ERA-5 backward trajectories were
506 calculated for each second of air sampling during the flight.

507 **3.4 The age of air since release from convective outflow**

508 This approach aims at investigating the possible influence of recent convection on NPF, filtering
509 out small contributions from matured air, which may be mixed in an air parcel but have only a

https://doi.org/10.5194/acp-2020-1158
Preprint. Discussion started: 2 December 2020


Atmospheric Chemistry and Physics Discussions

minor influence on the overall air mass composition. The history of a convective air mass is analysed by making use of the TRACZILLA Lagrangian model (Pisso and Legras, 2008), which is a variation of FLEXPART (Stohl et al., 2005). In its recent version the model interpolates velocities and heating rates directly from the hybrid grid to the position of the parcel using logarithmic pressure or potential temperature as vertical coordinate. The simulations were based on the release of a cluster of 1000 back-trajectories, representative of a generic aerosol tracer, which is launched at respective, each trajectory cluster from a 1-second resolved time step along the flight path. The trajectories were traced back over a period of 30 days in the geographical domain, spanning a longitude and latitude range of 10°W-160°E and 0-50°N, respectively. The meteorological fields are taken from the ECMWF reanalysis ERA-5 with 1-hour-resolution, assuming diabatic vertical motion. The convective influence is then distinguished from uninfluenced cases by the high-frequency images (one image per 10 – 15 minutes) of cloud top altitudes from the geostationary satellites MSG1 and Himawari. For computational reasons Himawari images were analysed in time steps of 20 minutes. The cloud top height of convective clouds is derived from the cloud top temperature and height (CTTH) product, developed within the European Organisation for the Exploitation of Meteorological Satellites (EUMETSAT) Satellite Application Facility (SAF) by support of Nowcasting Very Short Range Forecasting (NWC) products (Derrien et al. (2010); Schulz et al. (2009)).

Convective sources are identified as such if the course of a trajectory within a certain geographical area coincides with the cloud top level, as similarly done by Tzella and Legras (2011) and Tissier and Legras (2016). The possible convective sources are classified into major source region categories. It is noteworthy that, while the adopted trajectory method bypasses the uncertainties related to the convective representation in the reanalysis by using observation-based information on the convective events, uncertainties still remain. Those arise mainly from uncertainties in the identification of the cloud top from image data of geostationary satellites, the impossibility to account for the entrainment – detrainment – processes, and reanalysis-related uncertainties concerning advection. For more details on the trajectory-convective clouds coupling methods see Bucci et al. (2020). In the presented analysis, the air mass age is computed as the difference between the time of release of the cluster and the convective cloud crossing. Since the trajectory cluster can spread in space and bring different contributions from different regions, only the mean age from the dominant convective source

https://doi.org/10.5194/acp-2020-1158
Preprint. Discussion started: 2 December 2020


Atmospheric Chemistry and Physics Discussions

(i.e. the mean age from the regions with the highest percentage of convective clouds crossings) is considered in this analysis.

4 Observations and results

Figure 1 shows the flight tracks of the eight mission flights conducted during StratoClim 2017. The vertical indices (Panel b) highlight the flight sections where significantly increased mixing ratios of ultrafine particles n_{uf} were encountered, which are most likely attributed to NPF. NPF of varying intensity occurred near or above the southern flank of Himalayan mountain chain (features over Nepal and towards Northeast India) and in certain distance from the mountains (near the coastline of Bangladesh or the Northeast Indian coast towards the Sea of Bengal). Of the entire COPAS measurement time (~ 22.5 hours) at altitudes above 10 km (≳ 350 K potential temperature) over almost one third (i.e. ~ 9 hours) of the air samples were taken north of 26° N, i.e. mainly in the immediate vicinity of the Himalayan Mountains, over Nepal and neighbouring areas of northeast India. Hence, during the monsoon season of the year 2017, the main transport of NPF precursor material into the UT/LS was apparently by convection above the foothills of the Himalayas. The present study aims at a classification of encountered NPF events with regard to:

- the height intervals and geographical positions of NPF observations,
- the time limits (event duration and day time of occurrence),
- spatial dependencies with regard to tropopause height and AMA geometry.

Moreover, the relationship between NPF and the air's origin and age is investigated. It is noteworthy that, during StratoClim 2017, NPF was frequently observed in the presence of ice cloud particles at the bottom TTL of the AMA. The particular occurrence of in-cloud NPF is discussed in Weigel et al. (2020b). Since the NPF turned out to be almost undisturbed by the presence of cloud elements (until a certain density and size of the ice particles are reached), for the present study the NPF encounters remain unseparated concerning clear-air or in-cloud conditions and are instead discussed in their entirety.

https://doi.org/10.5194/acp-2020-1158
Preprint. Discussion started: 2 December 2020


Atmospheric Chemistry and Physics Discussions

4.1 Vertical distribution of particle number concentrations with respect to observations in the tropics

Vertical profiles of the total particle number concentration obtained from various field campaigns in the tropics are shown as median with percentiles in Figure 2. The vertical CN profiles from tropical regions of South America and West Africa (TROCCINOX, 2005 and SCOUT-AMMA, 2006, Figure 2, Panels a and b) exhibit merged data of two independent CN-detectors with individual d_{p50} (i.e. N_6 for $\theta > 350$ K and N_4 for $\theta < 350$ K), which were deployed on individual aircraft, the M-55 *Geophysic*a and the DLR Falcon-20 (cf. Borrmann et al. (2010) and Weigel et al. (2011)). The observations from measurements within the AMA over the Indian subcontinent (StratoClim 2017) at altitudes of about 320 K < θ < 475 K potential temperature exclusively result from COPAS measurements aboard the M-55 *Geophysica*. The dark shaded areas of the vertical profiles illustrate the scatter of number concentrations between the 90th and 99th percentiles. At tropopause altitudes around 380 K (indicated by vertical bars), or rather at the bottom TTL, the variability of detected concentration reaches a maximum between 90th and 99th percentile (note the logarithmic scale of N). The increased data scatter indicates that the population of sub-micrometre sized particles is subject to NPF occurring at these TTL levels, resulting in elevated particle number concentrations, which are highly variable, as is the production-rate of particles due to NPF (cf. Section 2.1.3). Exclusively above the tropopause within the AMA (Figure 2 c), the scatter of the concentration values of sub-micrometre sized particles remains elevated at up to ~ 400 K potential temperature. Up to this point, the dark shaded area (90th to 99th percentile range) of the AMA profile is visibly increased compared to median values, while aerosol concentrations measured above the tropopause in other regions (Figure 2 a and b) exhibit a smoother transition into the stratosphere.

For comparison, in Panel d of Figure 2, particle number concentrations $N_{5.3}$ are compiled as a vertical median profile (with percentiles) obtained from airborne measurements with the Nuclei Mode Aerosol Spectrometer (NMASS; Brock et al. (2000)) during several years (2004 – 2007, including winter and summer season) over Central America. These observations additionally differentiate the bottom TTL (here 350 – 379 K) as the region where NPF predominantly occurs with the largest impact on the fine-mode (sub-micrometre sized) aerosol particle concentration (e.g. Borrmann et al. (2010) or Weigel et al. (2011)). However, this vertical profile (Figure 2 d)

https://doi.org/10.5194/acp-2020-1158
Preprint. Discussion started: 2 December 2020


Atmospheric Chemistry and Physics Discussions

implies additional features at altitudes above the mean tropopause altitude (assumedly at ~ 380 K). The locally increased concentrations with respect to the median become apparent at ~ 380 – 390 K and at ~ 400 - 410 K, respectively. Above tropopause levels, significantly increased concentrations of fine-mode particles, potentially caused by local NPF, were observed over both, Central America (Figure 2 d) and the Indian subcontinent within the AMA (Figure 2 c).

4.2 Mixing ratios of submicron particles, abundance and fraction of refractory particles from StratoClim 2017 observations

The entire StratoClim 2017 data set of measured (1-Hz-resolved) particle mixing ratios n_6 and n_{10} is summarized in Figure 3 a as function of potential temperature. The resulting median profile n_6 of the StratoClim 2017 measurements is shown with 25th and 75th percentile (blue profile). This allows for a direct comparison with the corresponding median profiles from earlier COPAS measurements at tropical regions (in red: TROCCINOX, Brazil, 2005 and in dark green: SCOUT-AMMA, West Africa, 2006, cf. Borrmann et al. (2010) and Weigel et al. (2011)). Figure 3 a includes also the median vertical profile of the mixing ratios of fine-mode particles (bright green line), which was obtained from measurements over Central Pacific, at tropical latitudes (Brock et al., 1995).

The profiles (n_6, n_{10}, and n_{uf}) appear to be structured as:

1) ~ 350 – 380 K: characterised by the largest scatter of the particle mixing ratios and the highest values of up to $5 \cdot 10^4$ mg^{-1}, thus, representing the height level of the profile's maximum.
2) ~ 380 - 400 K: the scatter of the particle mixing ratios is still increased though less expressed, which may also be a result of recent NPF.
3) ~ 400 -415 K: characterised by a comparatively weak but extant scatter level of particle mixing ratios, which also includes features of the median n_6 profile at 410 – 415 K within the AMA.

The general course of the median profiles exhibits largely similar characteristics. The common feature of all median profiles from the tropics is their almost consistently located maximum at about 350 – 360 K, while the AMA observations indicate a corresponding maximum at slightly

https://doi.org/10.5194/acp-2020-1158
Preprint. Discussion started: 2 December 2020


Atmospheric Chemistry and Physics Discussions

626 higher altitudes (i.e. 355 – 365 K). Further up, the particle mixing ratios obtained from different
627 locations decrease with altitude with an almost corresponding gradient. In the altitude range
628 between 360 K and 400 K, the tropical data obtained over South America (red) constitute the
629 lowest particle mixing ratios (by median values), whereas all other profiles are almost in line
630 with each other up to 400 K. The vertical median profile of particle mixing ratios determined in
631 the AMA (blue) during StratoClim 2017 exhibit, however, the highest mixing ratios at each
632 height level up to ~ 415 K. Additionally, the AMA profile features a substantial increase of the
633 median mixing ratio at altitudes of ~ 410 - 415 K, where the values exceed those from the
634 tropical regions by almost 35 %. Above 415 K, the continuation of the tropical profiles from west
635 Africa and Central America (coloured green) with altitude is largely consistent with the particle
636 mixing ratios measured throughout StratoClim 2017, while at these altitudes the measurements
637 from South America (red) show comparatively increased values. Above 440 K, the particle
638 mixing ratio over West Africa (dark green) significantly deviates from those of all other vertical
639 profiles, as it is expressed by a gradual increase of the particle mixing ratio with altitude, which
640 was attributed to the influence of the high-reaching volcanic injections of Soufriere Hills
641 (Borrmann et al., 2010). The 1-Hz-resolved StratoClim 2017 data (grey dots in Figure 3 a)
642 additionally illustrate how the scatter of measured particle mixing ratios relates to
643 corresponding median profiles.

644 Figure 3 b shows the vertical distribution of the mixing ratio of the ultrafine particles n_{uf} (cf.
645 Subsection 2.1.1). The flight-by-flight colouration of the data points indicates that increased n_{uf}
646 values were observed during each of the eight StratoClim 2017 mission flights. In addition,
647 Figure 3 b shows the wide range of altitudes over which the layers of increased n_{uf} were
648 observed during the individual flights. Remarkably high values of n_{uf} were detected up to
649 altitudes as high as 400K.

650 Figure 3 c exhibits the 1-Hz-resolved mixing ratios of the non-volatile particles n_{10}nv (cf.
651 Subsection 2.1.2) as a function of the potential temperature. The graphic also includes the
652 resulting median profile of n_{10}nv with 25th and 75th percentiles. Figure 3 c additionally depicts
653 the median profile of n_6 as in Figure 3 a, to evaluate the vertical course of n_{10}nv in direct
654 relationship to the total particle mixing ratio. In Figure 3 d, the vertical distribution of the

https://doi.org/10.5194/acp-2020-1158
Preprint. Discussion started: 2 December 2020


Atmospheric Chemistry and Physics Discussions

655 fraction *f* is shown in 1-Hz-resolution as well as the resulting median profile with 25th and 75th
656 percentiles.

657 At lower altitudes (< 350 K), the mixing ratio of non-volatile particles appears predominantly
658 low with a relatively large scatter. At altitudes where n_6 exhibits the maximum particle mixing
659 ratio (i.e. ~ 355 - 365 K), the n_{10}nv profile almost stagnates or even decreases slightly. The local
660 minimum in the fraction *f* is reached at about the same height (355 – 375 K), as result of the
661 significantly increased total particle mixing ratio (likely due to NPF) with simultaneously
662 declining n_{10}nv. On transition to 370 K, the mixing ratio n_{10}nv is again slightly elevated, and
663 above 370 K, the n_{10}nv profile follows the general decline with height. Nevertheless, up to 380 K,
664 the decrease of n_6 with altitude is steeper compared to that of n_{10}nv. On transition to the 390 K
665 level, a sharp drop in the median *f* profile mainly results from the sudden change of the n_6
666 gradient at this altitude, whereas the n_{10}nv profile exhibits no obvious feature at the same
667 height. Above 390 K, both mixing ratios (n_6 and n_{10}nv) decrease uniformly and the fraction *f*
668 remains almost constant at ~ 45 – 50 % for the altitude range up to 430 K. Towards 435 K, the
669 total mixing ratio n_6 almost stagnates whereas n_{10}nv exhibits slightly dropping mixing ratios.
670 Thus, at this point, the shape of the median *f* profile is mainly determined by a decrease of the
671 non-volatile proportion of the particle population. Further above, in transition to 440 K potential
672 temperature, both mixing ratios (n_6 and n_{10}nv) commonly exhibit a steep decrease.

673 In essence, the vertical profiles of the total particle mixing ratio n_6 and those of the non-volatile
674 particles n_{10}nv are divided into three ranges:

675 A) At the bottom TTL region (θ < 375 K), both n_6 and n_{10}nv seem to be mainly characterised
676 by NPF as indicated by the high mixing ratios of ultrafine particles n_{uf}. NPF causes a
677 significant addition to the scatter of the total mixing ratios towards high values, which
678 exceed the median by more than one order of magnitude. In this altitude range, a local
679 deficit of the non-volatile particle compounds is a favourable precondition for NPF to
680 occur.
681 B) Further above, i.e. ~ 375 K < θ < 415 K, continued albeit attenuated NPF is identified at
682 tropopause levels within the AMA. The non-volatile particle compounds are slightly
683 elevated compared to levels below 375 K. The fraction *f* however rises towards 40 %.

https://doi.org/10.5194/acp-2020-1158
Preprint. Discussion started: 2 December 2020

Atmospheric Chemistry and Physics Discussions

Nevertheless, n_{uf} of 400 - 2000 mg^{-1} at heights of up to ~ 400 K indicate unimpededly proceeding NPF.

C) Above 415 K, the values of the total mixing ratio n_6 approaches a course that corresponds to previous observations (e.g. Brock et al. (1995)). The scatter of n_6 and n_{10}nv is considerably decreased at these altitudes. NPF appears to have abated entirely, since at these heights sufficiently high n_{uf} were not observed at all. The median proportion *f* of non-volatile particles of ~40 – 50 % remains up to the highest altitude.

The steeply dropping vertical profile of the total mixing ratio of the sub-micrometre sized aerosols above ~ 415 K may subtly indicate the upper limit of the AMA's influence on the vertical mixing of the UT/LS. From the CO, ozone, and nitrous oxide content in air samples taken throughout StratoClim 2017, von Hobe et al. (2020) concluded that the AMA's interior was largely isolated from stratospheric in-mixing up to altitudes of 10 to 20 K above the tropopause (i.e. $\theta \approx 400$ K). Moreover, they found that mixing processes with stratospheric air are of increasing significance at levels between 400 K and 420 K (*ibid.*). At altitudes above $\theta \approx 440$ K, the median mixing ratios n_6 exhibit a vertically stable continuation after another sharp drop between 435 K and 440 K (Figure 3 a and b). Brunamonti et al. (2018) specified the 440 K level as the top of confinement (TOC) of the AMA for the 2017 monsoon season, thus, above 440 K potential temperature ($\gtrsim$ 18.5 – 19 km), the median n_6 (Figure 3 a and b) may represent stratospheric background values.

The ATAL (Vernier et al. (2011a), and see also Höpfner et al. (2019); Mahnke et al. (2020)) is mainly attributed to the uplift of pollution from the boundary layer as concluded from balloon-borne and satellite-based observations (Vernier et al., 2018). The described drop in the aerosol concentration (*ibid.*) at potential temperatures of ~ 400-420 K (well above tropopause levels) coincides with the uppermost altitude limit of main NPF activity at ~400 K (~ 17.5 km) observed during StratoClim 2017 (cf. Figure 3). Here, the most substantial decrease of both mixing ratios n_6 and n_{10}nv was observed on height change from ~ 410 K to ~ 415 K (at ~ 18 km).

4.3 Occurrence frequency of NPF events

In compliance with the event definition (cf. Subsection 2.1.3), all observed NPF events (130 individual events) are sorted by their duration and the result is displayed in Figure 4. Based on the average flight speed (Section 2.1.3), and assuming a constant heading during flight, the mean

https://doi.org/10.5194/acp-2020-1158
Preprint. Discussion started: 2 December 2020

Atmospheric Chemistry and Physics Discussions

714 horizontal distance per 10 seconds flight time ranges at about 1.5 km. The spatially most
715 extended uninterrupted NPF signature throughout StratoClim 2017 spanned a mean horizontal
716 distance of ~ 110 km. The majority of observed NPF events cover durations of several tens of
717 seconds or less. About 50 NPF events had very short durations of less than 10 s (Figure 4 a and
718 b), while an almost equal number of NPF events was observed over a continuous period of 10 –
719 55 s (~ 1.5 – 8.5 km; Figure 4 b). Longer lasting NPF events of about 40 – 80 s (~ 6 – 13 km)
720 occurred less than six times during the entire campaign period. All NPF events of even longer
721 duration (up to ~ 12 minutes) occurred mostly once, but never more than two times in total
722 throughout the mission period. The hitherto most extended NPF event observed with COPAS at
723 TTL level over South America (Weigel et al. (2011)) lasted over a continuous duration of
724 262 seconds (~ 35.5 km of covered flight distance). Another three individual NPF events were
725 observed above West Africa (*ibid.*) over 20, 83, and 98 seconds (~ 3 km, ~ 12 km, and ~ 13 km)
726 respectively. Approximately 45 % of 130 NPF events observed throughout StratoClim 2017
727 were of less than 20 seconds duration (~ 3 km), while the majority (~ 75 %) of NPF
728 observations above the Indian subcontinent extended over less than 80 seconds (~ 12 km).

729 The diurnal distribution of observed NPF events is exhibited in Figure 5. Initially, the frequency
730 of NPF event observations is analysed as a function of the local daytime (LT) at Kathmandu,
731 Nepal (Figure 5 a). Apart from one exception, the occurrence frequency of the NPF events seems
732 evenly distributed over the course of a day. The exception is a time window at about 10:00 a.m.
733 to 10:30 a.m. (LT) when recent particle formation was observed up to 2.5 times more often than
734 at other times of the day. In this time window, about one third of all NPF events (31 of 105
735 events with durations of more than 5 seconds) was observed, most of which (25 of 31 events)
736 lasted for less than 80 seconds (< 12 km mean horizontal distance). The measurements in this
737 time window occurred at two distinct altitude layers, ~ 360 - 370K and ~ 390 – 400 K. The
738 majority of the NPF events in this period (20 of 31 events) were from altitudes above 390 K
739 while ascertained mixing ratios $\overline{n_{uf.}}$ never ranged outside ~ 500 - 5000 mg^{-1} during this day
740 time. Throughout the StratoClim 2017 mission, no further NPF event was observed above 390 K
741 at any earlier day time and only two single events were encountered at these heights during
742 different flights at a later day time (~12:20 and ~17:30 LT, respectively). Hence, it is very likely
743 that this pronounced frequency of NPF occurrence at a certain time of day results from biasing
744 effects and that instead the diurnal distribution of NPF events is in fact more evenly distributed.

https://doi.org/10.5194/acp-2020-1158
Preprint. Discussion started: 2 December 2020


Atmospheric Chemistry and Physics Discussions

In addition, however, a preferred daytime was not identified at which NPF observations would have occurred with particular frequency. This would be expected if H_2SO_4 is assumed to be the main nucleating compound whose production maximum (from the reaction SO_2 + OH) at local noon-time correlates with the solar zenith (cf. Weigel et al. (2011)).

According to the flight-by-flight distribution of NPF events over the day (Figure 5 b), the impression could arise that NPF events were observed more frequently in the morning than at local noontime. The observations of events in the afternoon are widely distributed over several hours, compared to the morning. NPF was predominantly observed before local noontime during the mission flights KTM 2, KTM 3, KTM 5 and KTM 7, while all other observations were made mainly during the afternoon. The diurnal distribution of the events as a function of event duration (Figure 5 c) indicates that the number of very short events (25 events) over less than five seconds (i.e. < $10^{0.7}$ s on the logarithmic scale, blue data points) remains below 20 % of all encountered events (130 events) and predominantly occurred in the morning hours. The majority of data points stem from event encounters, which lasted from 5 to 60 seconds (~ $10^{0.7}$ - $10^{1.8}$ s, greenish colours). Such durations of NPF encounters correspond to mean horizontal distances of about one to ten kilometres. These events, as also all longer lasting events, were almost homogeneously distributed over the day. Furthermore, Figure 5 c may also indicate that the longest NPF events are not necessarily associated with highest mean mixing ratios $\overline{n_{uf}}$. The duration of an event is therefore primarily an indicator of the spatial extent of a region where NPF takes place. The derivation of the spatial extent from the duration of individual events, however, bears significant uncertainties, since changes in flight attitude, such as curve manoeuvres or changing flight levels during an event, are not taken into account.

However, the NPF events observed during StratoClim 2017 are among the most frequent and spatially most extended of all those, which have been identified by means of COPAS measurements during previous missions (cf. Borrmann et al. (2010); Weigel et al. (2011)). Only a few events were observed during StratoClim 2017, which lasted more than 100 seconds, but it cannot be excluded that they were actually composed of individual events of smaller extent. Very short events (< 10 s) make almost 40 % of all NPF events observed. Consequently, hereafter, all events shorter than five seconds (i.e. 25 out of 130 events) are discarded from further analyses for the reasons described in Subsection 2.1.3 and for avoiding biasing effects.

https://doi.org/10.5194/acp-2020-1158
Preprint. Discussion started: 2 December 2020

Atmospheric Chemistry and Physics Discussions

4.4 The occurrence of NPF relative to the tropopause height and the AMA's centre

ERA-interim reanalysis data were used to determine the altitude of the lapse-rate tropopause in accordance with the definition by the WMO (1957) for each measurement point along the flight path (cf. Section 3.1). For the individual NPF events, a mean tropopause height was obtained together with mean values of detected $\overline{n_{\mathrm{uf}}}$. The relationship between the measurement height and the lapse-rate tropopause height is expressed as difference $\Delta\theta$ in K. In addition to the vertical position of NPF events (i.e. in terms of absolute height or distance from the tropopause), the individual NPF events were examined with respect to their position within the AMA by means of the equivalent latitudes ϕ_{equ} (cf. Section 3.1).

Figure 6 illustrates the mean n_{uf} measured during the individual NPF events as a function of (1) the distance $\overline{\Delta\theta}$ to the lapse rate tropopause (Figure 6, Panels a and c) and (2) the mean equivalent latitude $\overline{\phi_{\mathrm{equ}}}$ (Figure 6, Panels b, d and e). NPF events above the lapse-rate tropopause (Figure 6 a, positive $\overline{\Delta\theta}$) were mainly observed during the first half of the StratoClim 2017 mission (KTM 2, KTM 3, and KTM 5; on 29 July, 31 July, and on 04 August 2017, respectively) or during the last mission flight (KTM 8, on 10 August 2017). All further observations were located below the lapse-rate tropopause (negative $\overline{\Delta\theta}$) or in its close vicinity ($\overline{\Delta\theta} \approx 0$ K, e.g. KTM 6, 06 August 2017). As indicated by Stroh et al. (2020), the first half of the StratoClim 2017 mission was characterised by weak convection, while in succession of the campaign the convective activity increased. NPF event observations throughout StratoClim 2017 were limited to an altitude interval between about – 35 K and + 30 K potential temperature around tropopause heights, corresponding to a pressure range of 70 – 340 hPa and ambient temperatures between 187 K and 257 K according to observational data. With respect to the AMA centre, most NPF events were encountered north of 60° equivalent latitude (Figure 6 b). An exception is a flight segment of flight KTM 3 (on 31 July 2017), where NPF with mixing ratios $\overline{n_{\mathrm{uf}}}$ of ~ 500 - 1300 mg^{-1} were detected at the farthest distance from the AMA centre (near the turning point at about 21.5° N and 80° E geographic coordinates, see Figure 1).

These measurements (at $\overline{\phi_{\mathrm{equ}}} < 60°$ N) were made well above the tropopause since mean CO mixing ratios of 45 - 50 nmol mol^{-1} (Figure 6, Panels c and d) are commonly found at $\overline{\Delta\theta}$ between + 5 K and + 10 K. Towards the AMA centre ($\overline{\phi_{\mathrm{equ}}} > 60°$N), the NPF events are distributed over the entire range of $\overline{\Delta\theta}$. Here, NPF with several hundreds of ultrafine particles

https://doi.org/10.5194/acp-2020-1158
Preprint. Discussion started: 2 December 2020


Atmospheric Chemistry and Physics Discussions

per milligram were observed at $\overline{\Delta\theta}$ of up to about + 28 K above the lapse-rate tropopause. The vertical distribution of the NPF events indicates that those events with the highest $\overline{n_{uf}}$ and mainly elevated CO mixing ratios (mean values of more than 65 nmol mol^{-1} and up to ~ 137 nmol mol^{-1}) were encountered exclusively below the lapse-rate tropopause (to minimum $\overline{\Delta\theta}$ of - 35 K). However, none of these NPF events with elevated n_{uf} was detected at equivalent latitudes $\overline{\phi_{equ}}$ < 60°N. Between 60°N and 90°N equivalent latitude, however, no indication is apparent that the mixing ratios of $\overline{n_{uf}}$ and CO depend on the position with respect to the AMA centre.

Panel e of Figure 6 shows the NPF event distribution in the combined coordinate space of the equivalent latitude and the vertical distance from the lapse-rate tropopause. NPF events with highest $\overline{n_{uf}}$ ($\gtrsim$ 1300 mg^{-1}) were found exclusively between 60° N and 90° N with respect to the AMA centre and often immediately underneath the lapse-rate tropopause ($\overline{\Delta\theta} \lesssim$ - 3 K, colour-range from blue to yellow). NPF events with low $\overline{n_{uf}}$ ($\lesssim$ 1300 mg^{-1}) were exclusively found at tropopause levels ($\overline{\Delta\theta} \approx 0 \pm 5$ K, orange colours) or well above the lapse-rate tropopause ($\overline{\Delta\theta}$ > 10 K, red data points). Close to the AMA centre (60°N - 90° N) and in an altitude range of almost ± 30 K around tropopause heights, both the distribution of CO-enriched air masses and the occurrence of NPF appear as largely independent from $\overline{\phi_{equ}}$.

4.5 Persistence of particles in the ultrafine size mode

Coagulation constitutes one of the main processes, which limits the persistence of ultrafine particles. Due to the high diffusivity of the ultrafine particles, especially at elevated number densities, the particles collide and coagulate amongst each other and with the present background aerosol particles on short time scales. Gaseous precursors, which are highly saturated under NPF conditions, may condense and additionally contribute to the growth of particles out of the ultrafine size range, which is considered hereafter, however, as a secondary process.

The aerosol size distribution, which was compiled from the measurements during a NPF event as input for the coagulation simulation (cf. Section 3.2), is depicted in Figure 7 (black circles with horizontal bars indicating the width of their respective particle size bins of the model). The simulated change of the initial aerosol size distribution due to coagulation is shown in 1-hour

https://doi.org/10.5194/acp-2020-1158
Preprint. Discussion started: 2 December 2020


Atmospheric Chemistry and Physics Discussions

834 steps in different colours and line types (Figure 7 a). From this simulation, the temporal decay of
835 N_{uf} was derived (Figure 7 b, solid black line), whereby the gradient of this decay illustrates the
836 coagulation rate. The sequence of the simulated size distributions indicates that the initial
837 amount of ultrafine particles is reduced by coagulation within a few hours. Coagulation is most
838 effective particularly in the particle size range of $d_p < 15$ nm. Within the first hour after an
839 expired NPF event the ultrafine particle mode is no longer predominant in the overall size
840 distribution, as seen from the maximum of the distribution at $d_p > 15$ nm after one hour of
841 simulated coagulation (solid red line in Figure 7 a). Hence, based on number concentrations of
842 particles in the ultrafine size mode, a clear signature of NPF is detectable only when a NPF event
843 is just proceeding or for a very short time right after an expired NPF event.

844 The concentration of ultrafine particles N_{uf} decreases steeply over time (Figure 7 b). From
845 initially ~ 13000 cm^{-3} of ultrafine particles (~ 75 % of N_{total}) at the earliest stage, N_{uf} falls below
846 1000 cm^{-3} (~ 20 % of N_{total}) within about 1 hour (the grey shaded areas may serve for reference).
847 The detection of 1000 cm^{-3} of ultrafine particles, however, could be interpreted as a NPF event of
848 intermediate strength. In addition, coagulation leads to N_{uf} below 100 cm^{-3} (< 5 % of N_{total})
849 during less than four hours, which significantly impedes the identification of NPF based on in-
850 situ detections. N_{uf} of less than 10 cm^{-3} (reached within nine hours) would not be identified as
851 NPF event by means of COPAS measurements.

852 The sensitivity of this simulation was investigated by varying the simulation input. Therefore,
853 exclusively the input in the ultrafine size range was modified while keeping constant
854 background aerosol conditions. In three further simulation runs, the initial N_{uf} was multiplied by
855 the factors 0.1, 10 and 100, respectively ($N_{uf,0.1}$, $N_{uf,10}$, $N_{uf,100}$, dashed lines in Figure 7 b).
856 Increased initial concentrations of ultrafine particles, $N_{uf,10}$ and $N_{uf,100}$, last only for about 15
857 minutes compared to the original N_{uf} (black line in Figure 7 b). The initial values ~ 10^5 or
858 ~ 10^6 cm^{-3} drop very quickly due to elevated coagulation rates, and in both of these cases, $N_{uf,10}$
859 and $N_{uf,100}$ fall below 1000 cm^{-3} within less than one hour. The threshold of 100 cm^{-3} is crossed
860 after less than 2 hours ($N_{uf,10}$) or after 30 minutes ($N_{uf,100}$). Therefore, NPF events, which
861 produce much higher concentrations of ultrafine particles, require even shorter time periods for
862 a successful detection (e.g. by COPAS) after their expiration. However, for the simulation of
863 decreased concentrations ($N_{uf,0.1}$), the coagulation rates remain nearly constant, as indicated

https://doi.org/10.5194/acp-2020-1158
Preprint. Discussion started: 2 December 2020


Atmospheric Chemistry and Physics Discussions

from the almost identical decays of $N_{uf,\,0.1}$ and N_{uf} (Figure 7 b). Simulated concentration of ultrafine particles fall below 100 cm^{-3} within almost the same time from the initial values $N_{uf,\,0.1}$ or $N_{uf,\,10}$, respectively.

Based on these estimations, the detection of elevated N_{uf} strongly indicates that an event with high NPF-rates is currently proceeding, or a recently expired NPF event was observed. Due to the short persistence of ultrafine particles (a few hours), the observations of events with elevated N_{uf} are considered as made "well in time". Detections of lower values of N_{uf} could indicate a) intermediate or weak (currently proceeding) NPF at low supersaturation of the NPF precursor or b) a NPF event (potentially of high particle productivity) that has phased-out several hours before the observation. NPF is measured *in-situ* while the formation event is currently in progress or at most a few hours later. Therefore, the short periods of time available for a clear NPF detection and the yet frequent NPF encounters on each measurement flight during StratoClim 2017 indicate the prevalence of such events within the AMA.

5 NPF's connection to ground sources and vertical transport

5.1 NPF in relationship to CO as pollution indicator

NPF events with moderate numbers of ultrafine particles (< 1000 cm^{-3}) in the lower TTL region were previously attributed to CO mixing ratios above ~ 70 nmol mol^{-1} (as a reference: 60 - 70 nmol mol^{-1} were assumed as a typical CO background in the pristine marine boundary layer, cf. Weigel et al. (2011)). Elevated amounts of ultrafine particles (of up to ~ 6000 cm^{-3}) at altitudes of 350 K < θ < 360 K were associated with significantly increased CO mixing ratios of more than 85 nmol mol^{-1} (*ibid.*). These results, based mainly on two individual NPF events over West Africa (SCOUT AMMA 2008), may suggest a relationship between NPF with high densities of ultrafine particles and high CO mixing ratios and thus, a high level of pollution. However, as already indicated in Section 4.4 and Figure 6 (Panels c and d) by almost a hundred of individual event observations, the relationship between pollution level and NPF-induced n_{uf} is less direct than expected. In Figure 8, the 1-Hz-resolved data of synchronous detections of CO and particle mixing ratio during the entire StratoClim 2017 mission are compared. The total particle mixing ratio n_6 is shown in the background (grey dots) of the mixing ratio of ultrafine particles n_{uf}, (coloured data points in reference to θ) to illustrate the scatter range of both n_6 and of n_{uf}.

https://doi.org/10.5194/acp-2020-1158
Preprint. Discussion started: 2 December 2020

Atmospheric Chemistry and Physics Discussions

At altitudes below the tropopause (below ~ 380 K), where NPF causes the highest n_{uf}, the relationship between the 1-Hz-resolved n_6 or n_{uf} and the CO mixing ratio is highly variable. At CO levels of 80 – 100 nmol mol^{-1}, the scatter of the data covers the n_{uf} range from 700 mg^{-1} to the absolute maximum of about 50000 mg^{-1}. This maximum n_{uf} is exclusively reached at CO mixing ratios of 100 ± 2.5 nmol mol^{-1}. This is in qualitative agreement with earlier results from NPF detections at the bottom TTL over West Africa (Weigel et al., 2011) with a maximum of ultrafine particles at CO mixing ratios of up to 95 nmol mol^{-1}. However, compared to these results, the StratoClim 2017 data set is significantly extended towards much higher CO mixing ratios (up to 150 nmol mol^{-1}) coinciding with elevated but variable n_{uf}. At the maximum of the CO mixing ratio (i.e. ~ 150 nmol mol^{-1}) mixing ratios n_{uf} of about 6000 mg^{-1} (median value) were detected. Within a range of CO content between 85 and 130 nmol mol^{-1}, the n_{uf} (median) mixing ratios ranged consistently between 2000 and 10000 mg^{-1}, apart from the notable exception at about 100 nmol mol^{-1}.

At CO mixing ratios below 80 nmol mol^{-1} and on decrease to about 60 nmol mol^{-1}, the measurements were made just below or at tropopause levels (yellow to orange colours). Here, a decrease of n_{uf} from about 3000 mg^{-1} to values below 1000 mg^{-1} was observed. For CO mixing ratios below 60 nmol mol^{-1}, however, n_{uf} almost stagnates between 300 and 1300 mg^{-1}. Towards and across tropopause levels, n_{uf} and CO mixing ratios supposedly follow a systematic trend, which is not necessarily due to a correlation. On the one hand, the convective transport of CO from the ground does not directly reach tropopause levels or altitudes above the tropopause (cf. also Figure 6 c). On the other hand, on uplift further above 370 K potential temperature, CO is increasingly subject to depletion (cf. Section 2.3 and also von Hobe et al. (2020)). The NPF process likewise depends on the supply by NPF precursors, which also hardly reach up to heights above the tropopause by direct transport. Hence, at tropopause levels and aloft, the decreasing CO mixing ratio as well as abating NPF (expressed in decreasing n_{uf} values) very likely result from the lacking supply of precursor material by direct transport. According to von Hobe et al. (2020) any indication is missing that convection penetrated the tropopause during the StratoClim 2017 period. However, Lee et al. (2019) are investigate the TTL-hydrating influence of an overshooting event that occurred in the Sichuan Basin about 1.5 days before the StratoClim measurements southbound of Kathmandu over northeast India (M-55 *Geophysica*, KTM 7 on 8 August, 2017).

https://doi.org/10.5194/acp-2020-1158
Preprint. Discussion started: 2 December 2020


Atmospheric Chemistry and Physics Discussions

924 Hence, there is no clear indication for a direct relationship between CO enriched (polluted) air
925 and the intensity of NPF. Both CO and NPF precursors may commonly be transported by
926 convection and deposited in the lower TTL region. Therefore, both the highest CO and n_{uf} mixing
927 ratios are detectable within the lower TTL, but not coincidently. However, the comparatively
928 short atmospheric persistence of particles in the ultrafine size mode requires particular
929 consideration for this evaluation. Ultrafine particles in such high n_{uf} mixing ratios (> 10000 mg^{-1}
930 and up to 50000 mg^{-1}) have a persistence of hours in the atmosphere (cf. Section 4.5). Thus, on
931 observation of such significantly elevated n_{uf}, the NPF must either be in full progress or must
932 have happened within a very few hours prior to the measurement. If CO mixing ratios (as
933 indicator of the recent uplift of polluted air) had a direct impact on the NPF-rate, then the
934 detections of elevated n_{uf} should coincide with correspondingly high CO mixing ratios.
935 Conversely, however, high CO content does not necessarily imply strong NPF, as the limited time
936 the particles persist in the ultrafine size mode does not allow for distinguishing a currently
937 proceeding event of moderate NPF-rate from a strong NPF burst, which has occurred hours ago
938 (cf. Section 4.5).

939 **5.2 NPF and air mass origin in the boundary layer**

940 The apportioning of specific measurement sections, which feature elevated n_{uf}, to the locations
941 on the ground as possible precursor source regions is carried out in two steps:

942 (1) The backward trajectories were traced down to the boundary layer (BL) for each
943 measurement point (cf. Section 3.3) at which NPF was detected according to the passed criterion
944 (Figure 9 a and b).

945 (2) The ERA-5 reanalysis data were examined with regard to the transport time of the
946 trajectories between the position in the BL and the coordinates of the measurement point (Fig
947 9 c and d).

948 The top two panels of Figure 9 (a and c) illustrate the geographic position of the air's last BL
949 contact prior to the observations (1-Hz resolved) of elevated n_{uf} ($\gtrsim$ 300 mg^{-1}) throughout the
950 entire StratoClim 2017 mission. The bottom panels of Figure 9 (b and d) show the geographical
951 coordinates where the air mass experienced the fastest uplift in its transport history towards
952 each point of n_{uf} detection. Of course, the accuracy of the individual coordinates should not be

https://doi.org/10.5194/acp-2020-1158
Preprint. Discussion started: 2 December 2020


Atmospheric Chemistry and Physics Discussions

overestimated, for the reasons described in Section 3.3 and since the local resolutions of the observational data from in-situ measurements and of the reanalysis data are not equivalent. Particularly the spatial resolution of the reanalysis data is vertically variable. However, the panels of Figure 9 convey two aspects: (1) how widespread the distribution of the air masses origins is within the BL, from where an influence on the composition of the air samples could have occurred, and (2) in which geographical region the high-reaching convection has efficiently lifted the material to the level of air sampling. The numerous NPF observations and the currently highest resolution level of the ERA-5 data set should allow for identifying a systematic relationship, if existing, between the observed NPF and the trajectories' contact to the BL.

According to the distribution of the trajectories' latest BL contact (Figure 9 a) and the maximum vertical updraught (Figure 9 b) with reference to the n_{uf} mixing ratio, hardly any systematic structure is visible. The possible source regions are distributed over the entire monsoon region almost independently of the NPF intensity. Some of the trajectories' last BL contact point to locations far away from the monsoon region (e.g. in the West: the east coast of Africa and the Gulf of Aden; in the East: Indochina, the South China Sea and as far as the Philippine Sea). The entire possible source area of NPF precursors ranges from the north of India and the Arabian Sea, Pakistan, Afghanistan, Southwest China, Taiwan, the Philippines and the Bay of Bengal. South of ~ 10° N geographic latitude, the number of possible source regions decreases significantly. Locations of strongest vertical updraught are more compactly distributed (Figure 9 b) and better reflect the contours of the monsoon region. Hence, for the duration of the StratoClim 2017 mission, the convective uplift may largely have occurred within the AMA. This more compact regional distribution of vertical uplift is possibly related to the occurrence of a *vertical conduit* for upward transport in the monsoon, as conjectured by Bergman et al. (2013). Nevertheless, the almost homogeneous distribution of the n_{uf} mixing ratios within the displayed region of strongest convective uplift does not allow for identifying specific locations as potential source regions of NPF precursors. Furthermore, Figure 9 b indicates air masses of elevated n_{uf}, which have experienced convective uplift over Tajikistan and northern Afghanistan as well as over regions around the Yellow Sea, the Korean Peninsula or Japan, hence, far away from the AMA system.

https://doi.org/10.5194/acp-2020-1158
Preprint. Discussion started: 2 December 2020


Atmospheric Chemistry and Physics Discussions

With regard to the air mass transport time from the BL, the ERA-5 reanalysis data were examined over 50 days prior to the in-situ measurements (Section 3.3). For transport times exceeding 25 days, however, the data points in the Panels c and d of Figure 9 are displayed in grey. According to Figure 9 c, the air masses with the shortest transport times from the BL are found compactly around the region of the Himalayan mountain chain and its foothills. In Figure 9 c and d, the contour of the Himalayan chain is clearly reflected by the distribution of the data points (transport times of less than ~ 5 days and fastest vertical updraught). The highest n_{uf} mixing ratios were not detected in air from this region (Figure 9 a). The distribution shown in Figure 9 c also indicates that in air masses from remote locations (Gulf of Aden, Arabian Sea; or Philippine Sea, South China Sea, Bay of Bengal) also strongly elevated n_{uf} (> 10^4 mg^{-1}) were detected after comparatively long transport times of up to 25 days. Several other cases of elevated n_{uf} are visible in Figure 9 a, for which the transport times from the BL even exceeded 25 days (grey points in Figure 9 c). The Figure 9 d finally shows that the region of the air's last BL contact and the location of the fastest vertical uplift do not necessarily coincide. Hence, it may be surmised that, within the free troposphere, the air is subject to loading from various source regions (not exclusively from the location of the last BL contact) prior to its convective uplift. Of course, this finding may complicate an unambiguous apportioning of NPF to specific source regions of precursors in the BL.

The vertical distribution of the n_{uf} mixing ratios as a function of the air mass transport time from the BL is shown in Figure 10:

1) Above 380 K, almost all observations of enhanced n_{uf} are associated with air mass transport times of more than 12 days (note that the evaluation of the reanalysis covers up to 50 days of transport time in total). At 380 ±3 K, none of the detected n_{uf} is connected to air mass transport times of less than 12 days. Several times higher n_{uf} (with 10^3-10^4 mg^{-1}) were detected below 380 K in air masses, which had experienced more than 25 days of transport time from the BL.

2) Below 380 K, the transport times are variably distributed over the altitude range between 350 K and 380 K. The air masses with shortest transport times are located in the height interval between 360 K and 370 K. These air masses have presumably reached the ~ 360 K level (altitude of the main convective outflow) very quickly by an effective convective transport and

https://doi.org/10.5194/acp-2020-1158
Preprint. Discussion started: 2 December 2020


Atmospheric Chemistry and Physics Discussions

are then moved further aloft, towards 370 K, with much lower ascent rates (Vogel et al., 2019) due to the prevailing air mass uplift within the AMA.

3) On occasion, very short transport times were found with maximum n_{uf} at altitudes of about 367 K and 370 K. However, the highest n_{uf} are mostly not observed in air with such short transport times. Within 370 ± 3 K, detected n_{uf} reach almost extreme values (~ 50000 mg^{-1}) in air with transport times of up to 15 days. Above 370 K and below 355 K none of the maximum n_{uf} is associated with transport times of less than 6 days, and here, the highest n_{uf} were detected in air with transport times of up to 25 days. Therefore, based on the observations and the trajectories analysed here, the altitude band of the main convective outflow is limited to a range between 355 – 370 K.

5.3 The relationship between NPF and convective outflow

For the following analysis, which is summarised in Figure 11, the vertical distribution of the mean mixing ratios $\overline{n_{uf}}$ of respective NPF events (cf. Sections 2.1.3 and 4.4) are juxtaposed with

a) a measure for the convective contribution to the composition of the probed air mass and
b) the mean transport time within the TTL since their release from the top of individual convective cells (cf. Section 3.4 for both variables).

According to Figure 11 a, two vertical sections may be separated: At altitudes above ~ 380 K, the $\overline{n_{uf}}$ values remain below 2000 mg^{-1}, while the convective contribution to the probed air mostly remains below 35 %. At altitudes below ~ 380 K, most of the observed events exceeded $\overline{n_{uf}}$ values of 2000 mg^{-1}. About two thirds of all events that occurred below 380 K are connected to convective influence by more than 75 %. However, a remarkable proportion of observations below 380 K indicate convective contributions of less than 60 % and down to 25 %. Below ~ 375 K, mean mixing ratios $\overline{n_{uf}}$ of 1000-2000 mg^{-1} were associated with 100 % convective contribution, and mixing ratios of more than 10000 mg^{-1} were sometimes observed in air masses with ~ 30 % convective contribution.

For the observed NPF events, Figure 11 b shows the mean age of the probed air masses since their release from the top of individual convective cells. Above ~ 380 K, the air escaped at the convection top mainly 12 days (or more) prior to its probing. Two events at ~ 382 K and at ~ 385 K, respectively (e.g. likely connected to overshooting convection), indicate a more recent

https://doi.org/10.5194/acp-2020-1158
Preprint. Discussion started: 2 December 2020


Atmospheric Chemistry and Physics Discussions

convective uplift, within 5 days before the air was sampled. Despite the comparatively short transport times, here, the observed $\overline{n_{uf}}$ remained below 2000 mg^{-1}. At altitudes below ~ 380 K, the air predominantly resided within the TTL region for less than 5 days prior to the observation. Nevertheless, some of the comparatively intensive NPF events (with $\overline{n_{uf}} \approx$ 7000 – 15000 mg^{-1} at ~ 373 K, ~ 365 K, and at ~ 360 K) were also observed in air, which has been released from associated clouds' top more than a week (and up to two weeks) prior to the measurements. It should be considered, however, that short air mass transport times within the TTL are indicated also for NPF events with minor convective contribution (< 50 %).

Despite the limited data base, it can be concluded from these analyses that NPF at the lower TTL (i.e. below tropopause) within the AMA occurs in air masses that have been raised, even if only partially, by convection within the last 5 days to about two weeks. It remains undetermined, however, whether in some of the observed events the air samples were taken at a very advanced stage of NPF or how often the short period of time was missed during which NPF is detectable by aircraft-based measurements. Potential uncertainties remain to be considered in connection with the uncertainty of the reanalysis data and the representation of the transport history of the air masses.

6 Potential impact of gravity waves on vapors' supersaturation

The NPF precursor substances may primarily originate from sources on the ground and in the BL. The convective uplift doubtlessly constitutes one of the most effective transport mechanisms for lifting the material to altitudes of the lower TTL. As the prerequisite for NPF to take place within the TTL, however, the gaseous precursor material

a) must survive the convective uplift and must be released in sufficient quantities in the outflow region and at the lower TTL, and

b) in the TTL region, the NPF precursor material is required to be enriched to sufficient supersaturation.

If the uplifted precursor material was suitable for NPF immediately after its release from the convective outflow, the relationship between elevated n_{uf} and convective transport should be clearer than observed (cf. Section 5). The lack of an unambiguous relationship may indicate that

https://doi.org/10.5194/acp-2020-1158
Preprint. Discussion started: 2 December 2020


Atmospheric Chemistry and Physics Discussions

the recently transported material has yet to be converted into a NPF precursor within the UT/LS. Such a process would be, for example, the conversion of SO_2 to H_2SO_4, which occurs at stratospheric altitudes (Kremser et al., 2016) from tropospheric sulphur species, mainly OCS and others (cf. Section 1). The presence of ammonium species (Höpfner et al., 2019) or organics could then promote the NPF of H_2SO_4 in the TTL even at low supersaturations (Metzger et al. (2010); Kerminen et al. (2010); Kirkby et al. (2011); Kürten (2019)). The *in-situ* measurements with the aerosol mass spectrometer (AMS), the ERICA–AMS (ERICA, ERc instrument for the chemical composition of aerosols) during StratoClim 2017 showed that aerosols at the tropopause levels contain elevated amounts of nitrate (Höpfner et al., 2019). According to these observations, the nitrate concentration in the particle phase was higher than the particles' sulphate content at altitudes below 380 K. Nitric acid (HNO_3) is oxidised within a few days from NOx, which may be partly transported out of the BL or partly generated *in-situ* by lightning (Huntrieser et al., 2016). The presence of HNO_3, combined with ammonia may enhance the gas to growth of new particles (Wang et al., 2020).

The supersaturation required for initiating NPF could temporally also result from local cooling. It is conceivable that the NPF process and its intensity is locally triggered, e.g., by gravity waves. Gravity waves (GWs) represent low-frequency inertial perturbations of the initial atmospheric state. Such a perturbation is expressed particularly by a change in velocity of the vertical wind component. The passage of a GW is associated with a change in the vertical displacement of an air parcel and thus causes locally an adiabatic heating/cooling by a certain absolute value ΔT.

Piani et al. (2000) provided simulations of GWs initiated by deep convections. Their studies reveal a concentric propagation of GWs at altitudes above 15 km and up to ~ 40 km, which was effected by convective systems underneath. Horizontal wavelengths of about 40 km and vertical wavelengths of ~ 4 - 7 km were ascertained (*ibid.*). Similar wavelengths were found to be typical by other simulation studies concerning the propagation of GWs, which have been initiated, e.g., by convection at mid-latitudes (Song et al. (2003) and Chun and Kim (2008)) or by tropical convection (Lane and Moncrieff, 2008). Investigations related to GWs in connection with the monsoon are sparse, e.g. Wright and Gille (2011) and Ern and Preusse (2012) used satellite observations (High Resolution Dynamics Limb Sounder) which, however, are limited to detections of GWs with horizontal wavelengths greater than ~ 300 km. Despite the numerous

https://doi.org/10.5194/acp-2020-1158
Preprint. Discussion started: 2 December 2020


Atmospheric Chemistry and Physics Discussions

observational studies concerning GW properties (Alexander et al., 2010), the indirect retrieval of GWs' horizontal wavelengths remains uncertain by a factor of two (or more), whereas instrumental limitations inhibit the GW detection at horizontal wavelengths smaller than 100 km.

Observations using data sampled on commercial aircraft (Fritts and Nastrom, 1992) reported ~ 1 K^2 temperature variances (or rather variance enhancements by a factor 6.1 compared to undisturbed conditions) on passages of convection-induced GWs through the tropopause region. Based on radiosonde measurements (Vincent and Alexander, 2000), a 6-year averaged amplitude of 1.5 K is reported as an effect of GWs, with a single-case example of ~ 4 K-amplitude around 20 km altitude in the tropics. Hence, GW-induced temperature anomalies are observable up to a maximum ΔT of ~ 4 K, although smaller-scale perturbations occur more frequently. GW-induced negative temperature anomalies from an initial state T_0 increase a precursor's saturation ratio and the effect of such an anomaly on the degree of supersaturation applies qualitatively to any gaseous substance. Also in the homogeneous heteromolecular nucleation of more complex systems, the respective gas species or gas mixtures convert into particles as soon as the supersaturation exceeds the level required for the occurrence of NPF. Such more complex systems of precursor substances, e.g. with ammonia, nitric acid and/or organic components, are most likely involved in the formation process and promote NPF (Kirkby et al. (2011); Kürten (2019); Wang et al. (2020)).

Satellite images over the Indian subcontinent (e.g. from MSG-1 or HIMAWARI, cf. https://www.eorc.jaxa.jp/ptree/index.html) indicate quite frequent occurrences of convective plumes in the sampling areas and during the StratoClim 2017 mission period, which occasionally even arranged in chains of convective cells along the Himalayan foothills. The StratoClim flight KTM 6 on 06 August 2017 enabled NPF observations immediately connected to convection, which shot-through the flight level on passage at constant flight altitude. Corresponding part of the time series shown in Figure 12 covers the probing period in the air sector over Bangladesh and the Bay of Bengal (cf. Figure 1). Two phases of NPF observations are highlighted (oblique hatched areas in Figure 12), immediately before and after the period between 09:20 and 09:30 (UTC), during which the flight altitude changed from 16.2 km to about 13.8 km with subsequent re-ascent to 16.2 km. The manoeuvre above the northern part of the Bay of Bengal also marks the turning point of the mission flight path and the two flanking NPF phases were encountered

https://doi.org/10.5194/acp-2020-1158
Preprint. Discussion started: 2 December 2020


Atmospheric Chemistry and Physics Discussions

over the mainland near the coastlines of East India and Bangladesh (cf. Figure 1 b). The outbound and return sections of the flight passed through the same convectively active region, and the same convective system was likely probed at opposite positions.

Within the limits of the displayed time series (Figure 12 a) constant flight altitude and pressure level were maintained, except for the turning manoeuvre, which is therefore not subject of following discussion. The mixing ratios n_6, n_{10} and n_{15} coincidentally exhibited a clear positive signal of variable strength (Figure 12 b). The productivity of observed NPF events is derivable from the mixing ratio of the ultrafine particles n_{uf} (Figure 12 c), whereas during both NPF phases the particle mixing ratios reached peak values of more than 20000 mg^{-1} or they often remained elevated (> 10000 mg^{-1}). The course of n_{uf} is not mirrored at all by the CO signal (Figure 12 d), e.g. n_{uf} is at maximum values when CO is still at intermediate levels of ~ 110 nmol mol^{-1}. In accordance with the results discussed in Section 5.1 and illustrated in Figure 8, high n_{uf} seems not directly coupled to the supply of pollutants by convective transport (Figure 12 c and d). Furthermore, in both NPF phases, the peaks of air's CO content (130 - 140 nmol mol^{-1}, Figure 12 d) were accompanied by increasing mixing ratios n_{10}nv by a factor of up to two compared to the background (Figure 12 b), indicating the passage through the convective outflow plume, which also contained non-volatile aerosol material that was lifted together with gaseous pollutants.

During the periods of the NPF observations, however, the ambient air temperature T_{amb} (Figure 12 e) visibly fluctuates in the order of ± 1 K around the respective mean temperature (T_{mean} = 193 K with standard deviation below 1 K). Over the NPF period, the time series of the temperature fluctuation (T_{amb} - T_{mean}, Figure 12 e) exhibits the shape of a wave. In reference to the first NPF phase and assuming an average airspeed of 170 m s^{-1} throughout this period, the time series of the temperature fluctuation covers a peak-to-peak duration, which converts into a horizontal distance of ~ 90 km. It would go beyond the scope of this study to clearly attribute this temperature fluctuation to the GW activity initiated by a specific convective system. However, the amplitude and wavelength of the observed fluctuation correspond qualitatively and quantitatively to the values typical for GWs. If NPF is initialised by a negative temperature anomaly under supersaturated conditions, the newly formed ultrafine particles hardly

https://doi.org/10.5194/acp-2020-1158
Preprint. Discussion started: 2 December 2020

Atmospheric Chemistry and Physics Discussions

evaporate at re-rising temperatures (e.g. when the GW-induced temperature anomaly becomes positive).

The horizontal extent of GW-induced temperature anomalies, which can range from a few to hundreds of kilometres, is generally comparable with the magnitude of the horizontal extent of observed NPF fields (cf. Sections 2.1.3 and 4.3 as well as Figure 5 c). Since the time offset between NPF observation and NPF initiation is not exactly known, it is not straightforward to connect individual NPF events to specific incidents of GW-induced temperature anomalies. Moreover, during the monsoon season, several widely distributed, convective systems may induce GWs at the same time and the resulting, spatially propagating, temperature anomalies could interfere under each other at TTL heights. The amplification of temperature anomalies inherent with such interferences is neither locally resolvable nor quantifiable. Hence, GW-induced temperature anomalies may additionally promote the occurrence of NPF, particularly in cases, in which the enhancement of the NPF precursor saturation ratio, as prerequisite for NPF initiation, is not ascribable to direct (convective) uplift from the surface.

7 Summary and Conclusions

Between 27 July and 10 August 2017 the airborne StratoClim 2017 mission took place in Kathmandu, Nepal, with eight mission flights (~ 22.5 hours of COPAS measurement time above 10 km, $\theta \gtrsim 350$ K) up to altitudes of 20 km ($\theta \approx 475$ K) with the Russian high-altitude research aircraft M-55 *Geophysica*. The presented analysis comprises the description and discussion of numerous events of New Particle Formation (NPF), which were observed in the UT/LS region of the Asian Monsoon Anticyclone (AMA) over northern India, Nepal and Bangladesh.

During the StratoClim 2017 mission, a total duration of 2 hours and 38.5 minutes was spent under NPF conditions in the region of the Tropical Tropopause Layer (TTL), where enhanced quantities of ultrafine particles of up to ~ 50000 mg^{-1} (≈ 11000 cm^{-3}) were detected at heights of 15 – 16 km (~ 370 K). The majority of NPF observations with large amounts of ultrafine particles (6 nm < d_p < 15 nm) were observed at the lower TTL (~ 12-16 km, ~ 355 – 380 K) and below the tropopause. Nevertheless, NPF with enrichments of intermediate (~ 1000 – 2000 mg^{-1}) or low (~ 300 – 500 mg^{-1}) mixing ratios of ultrafine particles were also observed at levels around the tropopause (~ 380 K) and up to about 17.5 km altitude (400 K). The frequency of NPF observations during StratoClim 2017 over durations of ~ 10 seconds (< 1.5 km horizontal

https://doi.org/10.5194/acp-2020-1158
Preprint. Discussion started: 2 December 2020


Atmospheric Chemistry and Physics Discussions

distance) and with n_{uf} peaking up to 50000 mg^{-1} indicates a very effective and spacious source region of aerosols at TTL levels within the AMA. The numerous encounters of enhanced n_{uf} over several consecutive minutes (cf. Section 4.3 and Figure 4) indicate the NPF occurrence over extended fields of approximately 10 to 100 km (at event durations of 60 - 600 seconds).

The persistence of ultrafine particles (d_p < 15 nm) in the presence of the background aerosol population is largely determined by coagulation and limited to few hours only. Within the supersaturated environment under NPF conditions, co-condensation of gaseous species other than those involved in NPF may further promote the growth of ultrafine particles. The comparatively short persistence of the particles in the ultrafine size mode implies:

- After an expired NPF event, the number concentration of ultrafine particles decays due to coagulation by more than one order of magnitude within 2 hours.
- About 3-4 hours after a NPF event, the reduced number of ultrafine particles impedes the identification of NPF events based on aircraft-borne *in-situ* measurements.
- The interpretation of low and intermediate amounts of ultrafine particles is limited, as they may result from either moderate and just proceeding NPF or from an event with elevated NPF-rate that has phased-out over more than two hours before the measurement.
- High amounts of ultrafine particles i.e. (> 10000 mg^{-1}), however, indicate that NPF had occurred very shortly (less than one hour) prior to the measurement or was just proceeding when detected.

The supersaturated conditions, under which NPF occurs, however, may also favour the co-condensation of gaseous substances (Yu et al., 2017). Whether coagulation or condensation predominantly contributes to the composition of the background aerosol remains open. Most likely, both processes impact the formation and persistence of the ATAL (Vernier et al. (2011a), and see also Höpfner et al. (2019); Mahnke et al. (2020)), which was mainly attributed to the uplift of pollution from the boundary layer by means of balloon-borne and satellite-based observations (Vernier et al. (2018); Brunamonti et al. (2018); Hanumanthu et al. (2020)). In general, a refractory core with diameter greater than 10 nm was detected in almost every second particle above 395 K up to 475 K. This indicates the supply of other particulate material due to the updraught within the AMA (cf. also Section 6), although meteoric particles from higher altitudes (Schneider et al., 2020) may also play a role.

https://doi.org/10.5194/acp-2020-1158
Preprint. Discussion started: 2 December 2020


Atmospheric Chemistry and Physics Discussions

An indirect supply of the stratospheric (Junge) aerosol layer (Junge et al., 1961) at an altitude of ~ 25 km by freshly formed particles (at altitudes of up to 17.5 km) seems possible if a sufficiently effective transport mechanism is available. However, whether aerosol material subsides from TTL levels to mid-tropospheric altitudes and possibly contributes to cloud formation, as suggested by Andreae et al. (2018) to happen in the Amazon region, depends on the efficiency of downward transport, and on the aerosol's capability as CCN. Condensation of gaseous species other than those involved in the NPF process, and internal chemical conversion of various solutes within a particle could influence the aerosols' CCN capabilities. The transport times to altitudes far above or below the TTL appear long (several days and weeks) compared to the short persistence (hours) of ultrafine particles.

Three different approaches were used to correlate the occurrence frequency of most recent NPF (most enhanced n_{uf}) with possible source regions of precursor material in the BL and to find a direct connection of NPF to recent convective uplift and air mass transport times. Exceptionally elevated abundances of ultrafine particles (about ten to hundred times above the level of background aerosol concentrations) are used as indication for very recent occurrence of NPF. Intermediate or lower number densities of ultrafine particles could lead to ambiguous conclusions (cf. Section 4.5):

(1) The measurements indicate that highest n_{uf} values were predominantly found to coincide with intermediate to elevated CO mixing ratios of ~ 100 nmol mol^{-1}. Beyond that level, the mixing ratio of ultrafine particles is largely independent of the CO content (between 80 and 145 nmol mol^{-1}) of the air at the lower TTL.

(2) The most intensive uplift of air was confirmed to occur over the Himalayan mountain chain and its foothills. However, particular source regions of NPF precursors were not ascertainable within the BL. Furthermore, no indication was found that the most intense NPF was connected to short durations of air mass transport from the BL into the TTL.

(3) The convective contribution did not immediately determine the intensity of the observed NPF. The release of the precursor material in the outflow region of the convective top may have occurred up to 6 days before the NPF observation. Occasionally, however, air mass residence times of more than 6 days and up to 14 days were found at TTL levels prior to the NPF detection.

https://doi.org/10.5194/acp-2020-1158
Preprint. Discussion started: 2 December 2020


Atmospheric Chemistry and Physics Discussions

Consequently, the observed intensity of NPF is not unambiguously attributable to a) a specific source region on the ground or in the BL, or b) the effectiveness of the convective vertical transport, or c) the recent release of NPF-capable material from the convective outflow.

Nevertheless, it should be the convective uplift, which intermittently supplies the lower TTL by NPF precursor material. At altitudes well above tropopause levels, such an immediate supply by convection is lacking and could alternatively only proceed by the slow uplift superimposed on the anticyclonic ascent of the AMA (~ 1 K per day, Vogel et al. (2019); von Hobe et al. (2020) and Section 1.2). Generally, the question arises whether air mass transport and supply by convective updraught alone are sufficient to increase precursors' supersaturation such that NPF is initialised. At TTL levels in AMA, diabatic cooling by emission of infrared (IR) radiation constitutes a spatially large-scaled process that potentially increases the supersaturation of an NPF precursor system, but which occurs mainly during night hours, i.e. in the absence of solar irradiation. Alternatively, adiabatic cooling, however, could induce sufficient supersaturation of a precursor and thus play a role as a trigger for NPF. Temperature anomalies associated with gravity waves (GW) could very well increase the supersaturation of a precursor by that crucial bit above the NPF threshold. Interfering gravity waves, such as those likely initiated during the convectively very active Asian monsoon season, may increase the probability that occurring temperature anomalies are adequately large. Furthermore, the vertical propagation of GW-induced temperature anomalies could initialise NPF above tropopause levels, a) where ambient air temperatures increase with altitude (from observational data with $\Delta T \approx 1.5$ K per $\Delta\theta = 10$ K), which principally counteracts the supersaturation of a precursor, and b) where in the absence of overshooting convection a direct supply of precursor material from below is lacking.

The frequency of NPF observed during StratoClim 2017 exceeds all previous NPF detections with COPAS in the TTL over Brazil, Australia and West Africa (TROCCINOX 2005, SCOUT-O3 2005, SCOUT-AMMA 2006, cf. Borrmann et al. (2010); Weigel et al. (2011)). The maximum of detected ultrafine particles (~ 50000 mg^{-1}, correspondent to ~ 11000 cm^{-3} under ambient conditions at 360 K < θ < 370 K) is in comparable orders of magnitude to the earlier COPAS observations (*ibid*). Moreover, the horizontal extent of the NPF fields during StratoClim 2017, ranging from a few hundred metres to about one hundred kilometres, well compares to previous COPAS observations, although caveats inhere in the distinction of individual but closely adjacent

https://doi.org/10.5194/acp-2020-1158
Preprint. Discussion started: 2 December 2020


Atmospheric Chemistry and Physics Discussions

NPF fields due to the COPAS measurement resolution in conjunction with the flight speed of the M-55 *Geophysica*. The observations made during StratoClim 2017 indicate that frequent NPF with high production of ultrafine particles is capable of directly affecting the extent and persistence of the Asian Tropopause Aerosol Layer (ATAL). The continuous supply of freshly formed aerosol material, which coagulates both, internally and with the background aerosol, and which itself provides surface for the condensation of supersaturated gaseous substances, may contribute significantly to the aerosol composition of the ATAL up to altitudes of ~ 17.5 km (400 K). The chemical composition of the ATAL aerosol may include significant fractions of the material, which was previously involved in the NPF process and the particles' condensational growth, but this is subject to further investigation using the StratoClim 2017 data set.

Data availability:

The data shown in this study are available at the StratoClim campaign database at

https://stratoclim.icg.kfa-juelich.de/AfcMain/CampaignDataBase

or they may be provided by respective PI upon request

Author contribution

RW evaluated the data, created the figures, and draughted the manuscript with contributions by CM, MB, and AD. SB participated in the data analyses and the manuscript draughting. The code of the coagulation simulation was provided by BPL, and the code was adapted by MB while the calculations were performed by CM. BV, FP contributed with meteorological re-analyses, BV, SiB, and BL performed the air mass trajectory analyses. SV and FD'A took care of the CO data. UCSE data were delivered by GB. The manuscript was critically reviewed by CM, MB, AD, BV, FP, SV, FD'A, SiB, BL, BPL, and SB.

Competing interests

The authors declare no competing interests.

Acknowledgements

The contributions from the technical staff at the workshops of the MPI for Chemistry and the Institute for Physics of the Atmosphere (Mainz University), as well as the Myasishchev Design Bureau (MDB) were essential. We thank Y.-H. Kim, P. Spichtinger, H. Tost, M. Szakáll, A. Theis, and A. Miltenberger for helpful discussions. Many thanks to T. Peter for the planning of flight KTM 6 on 06 August 2017. In particular, we acknowledge support of T. Böttger, M. Flanz and W.

https://doi.org/10.5194/acp-2020-1158
Preprint. Discussion started: 2 December 2020

A. Schneider. The extraordinary commitment of F. Stroh in realisation of the campaign and the leadership of the entire StratoClim project by M. Rex are gratefully acknowledged. We very much thank the MDB crew and the M-55 *Geophysica* pilots. Some of our research leading to the presented results received funding from the European Research Council under the European Union's Seventh Framework Program (FP/2007-2013)/ERC Grant Agreement No. 321040 (EXCATRO). The StratoClim project was funded by the EU (FP7/2007–2018 Grant No. 603557) and also supported by the German "Bundesministerium für Bildung und Forschung" (BMBF) under the joint ROMIC-project SPITFIRE (01LG1205A). We explicitly thank the officials of the Nepalese government authorities, research institutions and Tribhuvan Airport as well as of the German Embassy for their extraordinary support and hospitality, which enabled our field campaign and research.

https://doi.org/10.5194/acp-2020-1158
Preprint. Discussion started: 2 December 2020

Atmospheric Chemistry and Physics Discussions

References

Alexander, M. J., Geller, M., McLandress, C., Polavarapu, S., Preusse, P., Sassi, F., Sato, K., Eckermann, S., Ern, M., Hertzog, A., Kawatani, Y., Pulido, M., Shaw, T. A., Sigmond, M., Vincent, R., and Watanabe, S.: Recent developments in gravity-wave effects in climate models and the global distribution of gravity-wave momentum flux from observations and models, Q J Roy Meteor Soc, 136, 1103-1124, 10.1002/qj.637, 2010.

Andreae, M. O., Afchine, A., Albrecht, R., Holanda, B. A., Artaxo, P., Barbosa, H. M. J., Borrmann, S., Cecchini, M. A., Costa, A., Dollner, M., Fütterer, D., Järvinen, E., Jurkat, T., Klimach, T., Konemann, T., Knote, C., Krämer, M., Krisna, T., Machado, L. A. T., Mertes, S., Minikin, A., Pöhlker, C., Pöhlker, M. L., Pöschl, U., Rosenfeld, D., Sauer, D., Schlager, H., Schnaiter, M., Schneider, J., Schulz, C., Spanu, A., Sperling, V. B., Voigt, C., Walser, A., Wang, J., Weinzierl, B., Wendisch, M., and Ziereis, H.: Aerosol characteristics and particle production in the upper troposphere over the Amazon Basin, Atmos Chem Phys, 18, 921-961, 10.5194/acp-18-921-2018, 2018.

Barth, M. C., Stuart, A. L., and Skamarock, W. C.: Numerical simulations of the July 10, 1996, Stratospheric-Tropospheric Experiment: Radiation, Aerosols, and Ozone (STERAO)-Deep Convection experiment storm: Redistribution of soluble tracers, J Geophys Res-Atmos, 106, 12381-12400, Doi 10.1029/2001jd900139, 2001.

Bergman, J. W., Jensen, E. J., Pfister, L., and Yang, Q.: Seasonal differences of vertical-transport efficiency in the tropical tropopause layer: On the interplay between tropical deep convection, large-scale vertical ascent, and horizontal circulationes, J Geophys Res-Atmos, 117, Artn D0530210.1029/2011jd016992, 2012.

Bergman, J. W., Fierli, F., Jensen, E. J., Honomichl, S., and Pan, L. L.: Boundary layer sources for the Asian anticyclone: Regional contributions to a vertical conduit, J Geophys Res-Atmos, 118, 2560-2575, 10.1002/jgrd.50142, 2013.

Borrmann, S., Kunkel, D., Weigel, R., Minikin, A., Deshler, T., Wilson, J. C., Curtius, J., Volk, C. M., Homan, C. D., Ulanovsky, A., Ravegnani, F., Viciani, S., Shur, G. N., Belyaev, G. V., Law, K. S., and Cairo, F.: Aerosols in the tropical and subtropical UT/LS: in-situ measurements of submicron particle abundance and volatility, Atmos Chem Phys, 10, 5573-5592, DOI 10.5194/acp-10-5573-2010, 2010.

Brock, C. A., Hamill, P., Wilson, J. C., Jonsson, H. H., and Chan, K. R.: Particle Formation in the Upper Tropical Troposphere: A Source of Nuclei for the Stratospheric Aerosol, Science, 270, 1650-1653, 10.2307/2887916, 1995.

Brock, C. A., Schröder, F., Kärcher, B., Petzold, A., Busen, R., and Fiebig, M.: Ultrafine particle size distributions measured in aircraft exhaust plumes, Journal of Geophysical Research: Atmospheres, 105, 26555-26567, 10.1029/2000jd900360, 2000.

Brunamonti, S., Jorge, T., Oelsner, P., Hanumanthu, S., Singh, B. B., Kumar, K. R., Sonbawne, S., Meier, S., Singh, D., Wienhold, F. G., Luo, B. P., Boettcher, M., Poltera, Y., Jauhiainen, H., Kayastha, R., Karmacharya, J., Dirksen, R., Naja, M., Rex, M., Fadnavis, S., and Peter, T.: Balloon-borne measurements of temperature, water vapor, ozone and aerosol backscatter on the southern slopes of the Himalayas during StratoClim 2016-2017, Atmos Chem Phys, 18, 15937-15957, 10.5194/acp-18-15937-2018, 2018.

Bucci, S., Legras, B., Sellitto, P., D'Amato, F., Viciani, S., Montori, A., Chiarugi, A., Ravegnani, F., Ulanovsky, A., Cairo, F., and Stroh, F.: Deep convective influence on the UTLS composition in the Asian Monsoon Anticyclone region: 2017 StratoClim campaign results, Atmos. Chem. Phys. Discuss., 2020, 1-29, 10.5194/acp-2019-1053, 2020.

https://doi.org/10.5194/acp-2020-1158
Preprint. Discussion started: 2 December 2020

1364 Campbell, P., and Deshler, T.: Condensation nuclei measurements in the midlatitude (1982–
1365 2012) and Antarctic (1986–2010) stratosphere between 20 and 35 km, Journal of Geophysical
1366 Research: Atmospheres, 119, 2013JD019710, 10.1002/2013jd019710, 2014.

1367 Chen, B., Xu, X. D., Yang, S., and Zhao, T. L.: Climatological perspectives of air transport from
1368 atmospheric boundary layer to tropopause layer over Asian monsoon regions during boreal
1369 summer inferred from Lagrangian approach, Atmos Chem Phys, 12, 5827-5839, 10.5194/acp-
1370 12-5827-2012, 2012.

1371 Chirkov, M., Stiller, G. P., Laeng, A., Kellmann, S., von Clarmann, T., Boone, C. D., Elkins, J. W.,
1372 Engel, A., Glatthor, N., Grabowski, U., Harth, C. M., Kiefer, M., Kolonjari, F., Krummel, P. B., Linden,
1373 A., Lunder, C. R., Miller, B. R., Montzka, S. A., Muhle, J., O'Doherty, S., Orphal, J., Prinn, R. G., Toon,
1374 G., Vollmer, M. K., Walker, K. A., Weiss, R. F., Wiegele, A., and Young, D.: Global HCFC-22
1375 measurements with MIPAS: retrieval, validation, global distribution and its evolution over 2005-
1376 2012, Atmos Chem Phys, 16, 3345-3368, 10.5194/acp-16-3345-2016, 2016.

1377 Chun, H.-Y., and Kim, Y.-H.: Secondary waves generated by breaking of convective gravity waves
1378 in the mesosphere and their influence in the wave momentum flux, Journal of Geophysical
1379 Research: Atmospheres, 113, 10.1029/2008jd009792, 2008.

1380 Clerbaux, C., George, M., Turquety, S., Walker, K. A., Barret, B., Bernath, P., Boone, C., Borsdorff, T.,
1381 Cammas, J. P., Catoire, V., Coffey, M., Coheur, P. F., Deeter, M., De Maziere, M., Drummond, J.,
1382 Duchatelet, P., Dupuy, E., de Zafra, R., Eddounia, F., Edwards, D. P., Emmons, L., Funke, B., Gille, J.,
1383 Griffith, D. W. T., Hannigan, J., Hase, F., Hopfner, M., Jones, N., Kagawa, A., Kasai, Y., Kramer, I., Le
1384 Flochmoen, E., Livesey, N. J., Lopez-Puertas, M., Luo, M., Mahieu, E., Murtagh, D., Nedelec, P.,
1385 Pazmino, A., Pumphrey, H., Ricaud, P., Rinsland, C. P., Robert, C., Schneider, M., Senten, C., Stiller,
1386 G., Strandberg, A., Strong, K., Sussmann, R., Thouret, V., Urban, J., and Wiacek, A.: CO
1387 measurements from the ACE-FTS satellite instrument: data analysis and validation using
1388 ground-based, airborne and spaceborne observations, Atmos Chem Phys, 8, 2569-2594, DOI
1389 10.5194/acp-8-2569-2008, 2008.

1390 Crumeyrolle, S., Manninen, H. E., Sellegri, K., Roberts, G., Gomes, L., Kulmala, M., Weigel, R., Laj, P.,
1391 and Schwarzenboeck, A.: New particle formation events measured on board the ATR-42 aircraft
1392 during the EUCAARI campaign, Atmos. Chem. Phys., 10, 6721-6735, 10.5194/acp-10-6721-2010,
1393 2010.

1394 Crutzen, P. J., and Lawrence, M. G.: The impact of precipitation scavenging on the transport of
1395 trace gases: A 3-dimensional model sensitivity study, J Atmos Chem, 37, 81-112, Doi
1396 10.1023/A:1006322926426, 2000.

1397 Curtius, J., Sierau, B., Arnold, F., de Reus, M., Strom, J., Scheeren, H. A., and Lelieveld, J.:
1398 Measurement of aerosol sulfuric acid 2. Pronounced layering in the free troposphere during the
1399 second Aerosol Characterization Experiment (ACE 2), J Geophys Res-Atmos, 106, 31975-31990,
1400 Doi 10.1029/2001jd000605, 2001.

1401 Curtius, J., Weigel, R., Vossing, H. J., Wernli, H., Werner, A., Volk, C. M., Konopka, P., Krebsbach, M.,
1402 Schiller, C., Roiger, A., Schlager, H., Dreiling, V., and Borrmann, S.: Observations of meteoric
1403 material and implications for aerosol nucleation in the winter Arctic lower stratosphere derived
1404 from in situ particle measurements, Atmos Chem Phys, 5, 3053-3069, DOI 10.5194/acp-5-3053-
1405 2005, 2005.

1406 de Reus, M., Borrmann, S., Bansemer, A., Heymsfield, A. J., Weigel, R., Schiller, C., Mitev, V., Frey,
1407 W., Kunkel, D., Kurten, A., Curtius, J., Sitnikov, N. M., Ulanovsky, A., and Ravegnani, F.: Evidence
1408 for ice particles in the tropical stratosphere from in-situ measurements, Atmos Chem Phys, 9,
1409 6775-6792, DOI 10.5194/acp-9-6775-2009, 2009.

https://doi.org/10.5194/acp-2020-1158
Preprint. Discussion started: 2 December 2020

Atmospheric Chemistry and Physics Discussions

1410 Dee, D. P., Uppala, S. M., Simmons, A. J., Berrisford, P., Poli, P., Kobayashi, S., Andrae, U.,
1411 Balmaseda, M. A., Balsamo, G., Bauer, P., Bechtold, P., Beljaars, A. C. M., van de Berg, L., Bidlot, J.,
1412 Bormann, N., Delsol, C., Dragani, R., Fuentes, M., Geer, A. J., Haimberger, L., Healy, S. B., Hersbach,
1413 H., Hólm, E. V., Isaksen, L., Kållberg, P., Köhler, M., Matricardi, M., McNally, A. P., Monge-Sanz, B.
1414 M., Morcrette, J. J., Park, B. K., Peubey, C., de Rosnay, P., Tavolato, C., Thépaut, J. N., and Vitart, F.:
1415 The ERA-Interim reanalysis: configuration and performance of the data assimilation system, Q J
1416 Roy Meteor Soc, 137, 553-597, 10.1002/qj.828, 2011.

1417 Derrien, M., Le Gleau, H., and Raoul, M.-P.: The use of the high resolution visible in SAFNWC/MSG
1418 cloud mask, in, 2010.

1419 Dunne, E. M., Gordon, H., Kürten, A., Almeida, J., Duplissy, J., Williamson, C., Ortega, I. K., Pringle,
1420 K. J., Adamov, A., Baltensperger, U., Barmet, P., Benduhn, F., Bianchi, F., Breitenlechner, M., Clarke,
1421 A., Curtius, J., Dommen, J., Donahue, N. M., Ehrhart, S., Flagan, R. C., Franchin, A., Guida, R., Hakala,
1422 J., Hansel, A., Heinritzi, M., Jokinen, T., Kangasluoma, J., Kirkby, J., Kulmala, M., Kupc, A., Lawler, M.
1423 J., Lehtipalo, K., Makhmutov, V., Mann, G., Mathot, S., Merikanto, J., Miettinen, P., Nenes, A.,
1424 Onnela, A., Rap, A., Reddington, C. L. S., Riccobono, F., Richards, N. A. D., Rissanen, M. P., Rondo, L.,
1425 Sarnela, N., Schobesberger, S., Sengupta, K., Simon, M., Sipilä, M., Smith, J. N., Stozkhov, Y., Tomé,
1426 A., Tröstl, J., Wagner, P. E., Wimmer, D., Winkler, P. M., Worsnop, D. R., and Carslaw, K. S.: Global
1427 atmospheric particle formation from CERN CLOUD measurements, Science, 354, 1119-1124,
1428 10.1126/science.aaf2649, 2016.

1429 Ekman, A. M. L., Wang, C., Strom, J., and Krejci, R.: Explicit simulation of aerosol physics in a
1430 cloud-resolving model: Aerosol transport and processing in the free troposphere, Journal of the
1431 Atmospheric Sciences, 63, 682-696, Doi 10.1175/Jas3645.1, 2006.

1432 Ern, M., and Preusse, P.: Gravity wave momentum flux spectra observed from satellite in the
1433 summertime subtropics: Implications for global modeling, Geophys Res Lett, 39,
1434 10.1029/2012gl052659, 2012.

1435 Frey, W., Borrmann, S., Kunkel, D., Weigel, R., de Reus, M., Schlager, H., Roiger, A., Voigt, C., Hoor,
1436 P., Curtius, J., Kramer, M., Schiller, C., Volk, C. M., Homan, C. D., Fierli, F., Di Donfrancesco, G.,
1437 Ulanovsky, A., Ravegnani, F., Sitnikov, N. M., Viciani, S., D'Amato, F., Shur, G. N., Belyaev, G. V.,
1438 Law, K. S., and Cairo, F.: In situ measurements of tropical cloud properties in the West African
1439 Monsoon: upper tropospheric ice clouds, Mesoscale Convective System outflow, and subvisual
1440 cirrus, Atmos Chem Phys, 11, 5569-5590, DOI 10.5194/acp-11-5569-2011, 2011.

1441 Fritts, D. C., and Nastrom, G. D.: Sources of Mesoscale Variability of Gravity Waves. Part II:
1442 Frontal, Convective, and Jet Stream Excitation, Journal of the Atmospheric Sciences, 49, 111-127,
1443 10.1175/1520-0469(1992)049<0111:Somvog>2.0.Co;2, 1992.

1444 Froyd, K. D., Murphy, D. M., Lawson, P., Baumgardner, D., and Herman, R. L.: Aerosols that form
1445 subvisible cirrus at the tropical tropopause, Atmos Chem Phys, 10, 209-218, DOI 10.5194/acp-
1446 10-209-2010, 2010.

1447 Garny, H., and Randel, W. J.: Transport pathways from the Asian monsoon anticyclone to the
1448 stratosphere, Atmos. Chem. Phys., 16, 2703-2718, 10.5194/acp-16-2703-2016, 2016.

1449 Glatthor, N., Hopfner, M., Baker, I. T., Berry, J., Campbell, J. E., Kawa, S. R., Krysztofiak, G., Leyser,
1450 A., Sinnhuber, B. M., Stiller, G. P., Stinecipher, J., and von Clarmann, T.: Tropical sources and sinks
1451 of carbonyl sulfide observed from space, Geophys Res Lett, 42, 10082-10090,
1452 10.1002/2015gl066293, 2015.

1453 Hanumanthu, S., Vogel, B., Müller, R., Brunamonti, S., Fadnavis, S., Li, D., Ölsner, P., Naja, M., Singh,
1454 B. B., Kumar, K. R., Sonbawne, S., Jauhiainen, H., Vömel, H., Luo, B., Jorge, T., Wienhold, F. G.,

https://doi.org/10.5194/acp-2020-1158
Preprint. Discussion started: 2 December 2020

Atmospheric Chemistry and Physics Discussions

1455 Dirkson, R., and Peter, T.: Strong variability of the Asian Tropopause Aerosol Layer (ATAL) in
1456 August 2016 at the Himalayan foothills, Atmos. Chem. Phys. Discuss., 2020, 1-42, 10.5194/acp-
1457 2020-552, 2020.

1458 He, Q., Ma, J., Zheng, X., Yan, X., Vömel, H., Wienhold, F. G., Gao, W., Liu, D., Shi, G., and Cheng, T.:
1459 Observational evidence of particle hygroscopic growth in the upper troposphere–lower
1460 stratosphere (UTLS) over the Tibetan Plateau, Atmos. Chem. Phys., 19, 8399-8406, 10.5194/acp-
1461 19-8399-2019, 2019.

1462 Heald, C. L., Jacob, D. J., Park, R. J., Russell, L. M., Huebert, B. J., Seinfeld, J. H., Liao, H., and Weber,
1463 R. J.: A large organic aerosol source in the free troposphere missing from current models,
1464 Geophys Res Lett, 32, Artn L1880910.1029/2005gl023831, 2005.

1465 Hersbach, H., and Dee, D. P.: ERA5 reanalysis is in production, ECMWF Newsletter, 147, 7, 2016.

1466 Hoffmann, L., Günther, G., Li, D., Stein, O., Wu, X., Griessbach, S., Heng, Y., Konopka, P., Müller, R.,
1467 Vogel, B., and Wright, J. S.: From ERA-Interim to ERA5: the considerable impact of ECMWF's
1468 next-generation reanalysis on Lagrangian transport simulations, Atmos Chem Phys, 19, 3097-
1469 3124, 10.5194/acp-19-3097-2019, 2019.

1470 Hoor, P., Gurk, C., Brunner, D., Hegglin, M. I., Wernli, H., and Fischer, H.: Seasonality and extent of
1471 extratropical TST derived from in-situ CO measurements during SPURT, Atmos Chem Phys, 4,
1472 1427-1442, DOI 10.5194/acp-4-1427-2004, 2004.

1473 Hoor, P., Fischer, H., and Lelieveld, J.: Tropical and extratropical tropospheric air in the
1474 lowermost stratosphere over Europe: A CO-based budget, Geophys Res Lett, 32, Artn
1475 L0780210.1029/2004gl022018, 2005.

1476 Höpfner, M., Boone, C. D., Funke, B., Glatthor, N., Grabowski, U., Günther, A., Kellmann, S., Kiefer,
1477 M., Linden, A., Lossow, S., Pumphrey, H. C., Read, W. G., Roiger, A., Stiller, G., Schlager, H., von
1478 Clarmann, T., and Wissmüller, K.: Sulfur dioxide (SO_2) from MIPAS in the upper troposphere and
1479 lower stratosphere 2002-2012, Atmos Chem Phys, 15, 7017-7037, 10.5194/acp-15-7017-2015,
1480 2015.

1481 Höpfner, M., Ungermann, J., Borrmann, S., Wagner, R., Spang, R., Riese, M., Stiller, G., Appel, O.,
1482 Batenburg, A. M., Bucci, S., Cairo, F., Dragoneas, A., Friedl-Vallon, F., Hünig, A., Johansson, S.,
1483 Krasauskas, L., Legras, B., Leisner, T., Mahnke, C., Möhler, O., Molleker, S., Müller, R., Neubert, T.,
1484 Orphal, J., Preusse, P., Rex, M., Saathoff, H., Stroh, F., Weigel, R., and Wohltmann, I.: Ammonium
1485 nitrate particles formed in upper troposphere from ground ammonia sources during Asian
1486 monsoons, Nat Geosci, 12, 608-612, 10.1038/s41561-019-0385-8, 2019.

1487 Huntrieser, H., Lichtenstern, M., Scheibe, M., Aufmhoff, H., Schlager, H., Pucik, T., Minikin, A.,
1488 Weinzierl, B., Heimerl, K., Pollack, I. B., Peischl, J., Ryerson, T. B., Weinheimer, A. J., Honomichl, S.,
1489 Ridley, B. A., Biggerstaff, M. I., Betten, D. P., Hair, J. W., Butler, C. F., Schwartz, M. J., and Barth, M.
1490 C.: Injection of lightning-produced NOx, water vapor, wildfire emissions, and stratospheric air to
1491 the UT/LS as observed from DC3 measurements, Journal of Geophysical Research: Atmospheres,
1492 121, 6638-6668, 10.1002/2015jd024273, 2016.

1493 Jacobson, M. Z.: Fundamentals of Atmospheric Modeling, Cambridge University Press., New York,
1494 813 pp., 2005.

1495 Jost, A., Szakáll, M., Diehl, K., Mitra, S. K., and Borrmann, S.: Chemistry of riming: the retention of
1496 organic and inorganic atmospheric trace constituents, Atmos. Chem. Phys., 17, 9717-9732,
1497 10.5194/acp-17-9717-2017, 2017.

https://doi.org/10.5194/acp-2020-1158
Preprint. Discussion started: 2 December 2020

Atmospheric Chemistry and Physics Discussions

1498 Kerminen, V. M., Petaja, T., Manninen, H. E., Paasonen, P., Nieminen, T., Sipila, M., Junninen, H.,
1499 Ehn, M., Gagne, S., Laakso, L., Riipinen, I., Vehkamaki, H., Kurten, T., Ortega, I. K., Dal Maso, M.,
1500 Brus, D., Hyvarinen, A., Lihavainen, H., Leppa, J., Lehtinen, K. E. J., Mirme, A., Mirme, S., Horrak, U.,
1501 Berndt, T., Stratmann, F., Birmili, W., Wiedensohler, A., Metzger, A., Dommen, J., Baltensperger,
1502 U., Kiendler-Scharr, A., Mentel, T. F., Wildt, J., Winkler, P. M., Wagner, P. E., Petzold, A., Minikin, A.,
1503 Plass-Dulmer, C., Poschl, U., Laaksonen, A., and Kulmala, M.: Atmospheric nucleation: highlights
1504 of the EUCAARI project and future directions, Atmos Chem Phys, 10, 10829-10848,
1505 10.5194/acp-10-10829-2010, 2010.

1506 Kerminen, V. M., Chen, X. M., Vakkari, V., Petäjä, T., Kulmala, M., and Bianchi, F.: Atmospheric new
1507 particle formation and growth: review of field observations, Environ Res Lett, 13, Artn
1508 10300310.1088/1748-9326/Aadf3c, 2018.

1509 Kirkby, J., Curtius, J., Almeida, J., Dunne, E., Duplissy, J., Ehrhart, S., Franchin, A., Gagne, S., Ickes,
1510 L., Kurten, A., Kupc, A., Metzger, A., Riccobono, F., Rondo, L., Schobesberger, S., Tsagkogeorgas, G.,
1511 Wimmer, D., Amorim, A., Bianchi, F., Breitenlechner, M., David, A., Dommen, J., Downard, A., Ehn,
1512 M., Flagan, R. C., Haider, S., Hansel, A., Hauser, D., Jud, W., Junninen, H., Kreissl, F., Kvashin, A.,
1513 Laaksonen, A., Lehtipalo, K., Lima, J., Lovejoy, E. R., Makhmutov, V., Mathot, S., Mikkila, J.,
1514 Minginette, P., Mogo, S., Nieminen, T., Onnela, A., Pereira, P., Petaja, T., Schnitzhofer, R., Seinfeld, J.
1515 H., Sipila, M., Stozhkov, Y., Stratmann, F., Tome, A., Vanhanen, J., Viisanen, Y., Vrtala, A., Wagner, P.
1516 E., Walther, H., Weingartner, E., Wex, H., Winkler, P. M., Carslaw, K. S., Worsnop, D. R.,
1517 Baltensperger, U., and Kulmala, M.: Role of sulphuric acid, ammonia and galactic cosmic rays in
1518 atmospheric aerosol nucleation, Nature, 476, 429-U477, 10.1038/nature10343, 2011.

1519 Konopka, P., Ploeger, F., and Müller, R.: Entropy- and static stability-based Lagrangian model
1520 grids in: Geophysical Monograph Series: Lagrangian Modeling of the Atmosphere, edited by Lin,
1521 J., 200, 99-109, https://doi.org/10.1029/2012GM001253, 2012.

1522 Kremser, S., Thomason, L. W., von Hobe, M., Hermann, M., Deshler, T., Timmreck, C., Toohey, M.,
1523 Stenke, A., Schwarz, J. P., Weigel, R., Fueglistaler, S., Prata, F. J., Vernier, J.-P., Schlager, H., Barnes,
1524 J. E., Antuña-Marrero, J.-C., Fairlie, D., Palm, M., Mahieu, E., Notholt, J., Rex, M., Bingen, C.,
1525 Vanhellemont, F., Bourassa, A., Plane, J. M. C., Klocke, D., Carn, S. A., Clarisse, L., Trickl, T., Neely,
1526 R., James, A. D., Rieger, L., Wilson, J. C., and Meland, B.: Stratospheric aerosol - Observations,
1527 processes, and impact on climate, Rev Geophys, 2015RG000511, 10.1002/2015rg000511, 2016.

1528 Kulmala, M., Vehkamaki, H., Petaja, T., Dal Maso, M., Lauri, A., Kerminen, V. M., Birmili, W., and
1529 McMurry, P. H.: Formation and growth rates of ultrafine atmospheric particles: a review of
1530 observations, J Aerosol Sci, 35, 143-176, 10.1016/j.jaerosci.2003.10.003, 2004.

1531 Kulmala, M., Kontkanen, J., Junninen, H., Lehtipalo, K., Manninen, H. E., Nieminen, T., Petaja, T.,
1532 Sipila, M., Schobesberger, S., Rantala, P., Franchin, A., Jokinen, T., Jarvinen, E., Aijala, M.,
1533 Kangasluoma, J., Hakala, J., Aalto, P. P., Paasonen, P., Mikkila, J., Vanhanen, J., Aalto, J., Hakola, H.,
1534 Makkonen, U., Ruuskanen, T., Mauldin, R. L., Duplissy, J., Vehkamaki, H., Back, J., Kortelainen, A.,
1535 Riipinen, I., Kurten, T., Johnston, M. V., Smith, J. N., Ehn, M., Mentel, T. F., Lehtinen, K. E. J.,
1536 Laaksonen, A., Kerminen, V. M., and Worsnop, D. R.: Direct Observations of Atmospheric Aerosol
1537 Nucleation, Science, 339, 943-946, 10.1126/science.1227385, 2013.

1538 Kürten, A., Bianchi, F., Almeida, J., Kupiainen-Maatta, O., Dunne, E. M., Duplissy, J., Williamson, C.,
1539 Barmet, P., Breitenlechner, M., Dommen, J., Donahue, N. M., Flagan, R. C., Franchin, A., Gordon, H.,
1540 Hakala, J., Hansel, A., Heinritzi, M., Ickes, L., Jokinen, T., Kangasluoma, J., Kim, J., Kirkby, J., Kupc,
1541 A., Lehtipalo, K., Leiminger, M., Makhmutov, V., Onnela, A., Ortega, I. K., Petaja, T., Praplan, A. P.,
1542 Riccobono, F., Rissanen, M. P., Rondo, L., Schnitzhofer, R., Schobesberger, S., Smith, J. N., Steiner,
1543 G., Stozhkov, Y., Tome, A., Trostl, J., Tsagkogeorgas, G., Wagner, P. E., Wimmer, D., Ye, P. L.,
1544 Baltensperger, U., Carslaw, K., Kulmala, M., and Curtius, J.: Experimental particle formation rates

https://doi.org/10.5194/acp-2020-1158
Preprint. Discussion started: 2 December 2020

Atmospheric Chemistry and Physics Discussions

1545 spanning tropospheric sulfuric acid and ammonia abundances, ion production rates, and
1546 temperatures, J Geophys Res-Atmos, 121, 12377-12400, 10.1002/2015jd023908, 2016.

1547 Kürten, A., Li, C., Bianchi, F., Curtius, J., Dias, A., Donahue, N. M., Duplissy, J., Flagan, R. C., Hakala,
1548 J., Jokinen, T., Kirkby, J., Kulmala, M., Laaksonen, A., Lehtipalo, K., Makhmutov, V., Onnela, A.,
1549 Rissanen, M. P., Simon, M., Sipilä, M., Stozhkov, Y., Tröstl, J., Ye, P., and McMurry, P. H.: New
1550 particle formation in the sulfuric acid–dimethylamine–water system: reevaluation of CLOUD
1551 chamber measurements and comparison to an aerosol nucleation and growth model, Atmos.
1552 Chem. Phys., 18, 845-863, 10.5194/acp-18-845-2018, 2018.

1553 Kürten, A.: New particle formation from sulfuric acid and ammonia: nucleation and growth
1554 model based on thermodynamics derived from CLOUD measurements for a wide range of
1555 conditions, Atmos. Chem. Phys., 19, 5033-5050, 10.5194/acp-19-5033-2019, 2019.

1556 Lane, T. P., and Moncrieff, M. W.: Stratospheric Gravity Waves Generated by Multiscale Tropical
1557 Convection, Journal of the Atmospheric Sciences, 65, 2598-2614, 10.1175/2007jas2601.1, 2008.

1558 Lee, K. O., Dauhut, T., Chaboureau, J. P., Khaykin, S., Kramer, M., and Rolf, C.: Convective hydration
1559 in the tropical tropopause layer during the StratoClim aircraft campaign: pathway of an
1560 observed hydration patch, Atmos Chem Phys, 19, 11803-11820, 10.5194/acp-19-11803-2019,
1561 2019.

1562 Lee, S. H., Wilson, J. C., Baumgardner, D., Herman, R. L., Weinstock, E. M., LaFleur, B. G., Kok, G.,
1563 Anderson, B., Lawson, P., Baker, B., Strawa, A., Pittman, J. V., Reeves, J. M., and Bui, T. P.: New
1564 particle formation observed in the tropical/subtropical cirrus clouds, J Geophys Res-Atmos, 109,
1565 Artn D2020910.1029/2004jd005033, 2004.

1566 Li, D., Vogel, B., Bian, J. C., Müller, R., Pan, L. L., Günther, G., Bai, Z. X., Li, Q., Zhang, J. Q., Fan, Q. J.,
1567 and Vömel, H.: Impact of typhoons on the composition of the upper troposphere within the Asian
1568 summer monsoon anticyclone: the SWOP campaign in Lhasa 2013, Atmos Chem Phys, 17, 4657-
1569 4672, 10.5194/acp-17-4657-2017, 2017.

1570 Li, D., Vogel, B., Müller, R., Bian, J. C., Günther, G., Li, Q., Zhang, J. Q., Bai, Z. X., Vömel, H., and Riese,
1571 M.: High tropospheric ozone in Lhasa within the Asian summer monsoon anticyclone in 2013:
1572 influence of convective transport and stratospheric intrusions, Atmos Chem Phys, 18, 17979-
1573 17994, 10.5194/acp-18-17979-2018, 2018.

1574 Li, D., Vogel, B., Muller, R., Bian, J. C., Gunther, G., Ploeger, F., Li, Q., Zhang, J. Q., Bai, Z. X., Vomel, H.,
1575 and Riese, M.: Dehydration and low ozone in the tropopause layer over the Asian monsoon
1576 caused by tropical cyclones: Lagrangian transport calculations using ERA-Interim and ERA5
1577 reanalysis data, Atmos Chem Phys, 20, 4133-4152, 10.5194/acp-20-4133-2020, 2020.

1578 Logan, J. A., Prather, M. J., Wofsy, S. C., and Mcelroy, M. B.: Tropospheric Chemistry - a Global
1579 Perspective, J Geophys Res-Oceans, 86, 7210-7254, DOI 10.1029/JC086iC08p07210, 1981.

1580 Mahnke, C., Weigel, R., Cairo, F., Vernier, J.-P., Afchine, A., Krämer, M., Mitev, V., Matthey, R.,
1581 Viciani, S., D'Amato, F., Ploeger, F., Deshler, T., and Borrmann, S.: The ATAL within the 2017
1582 Asian Monsoon Anticyclone: Microphysical aerosol properties derived from aircraft-borne in
1583 situ measurements, in preparation for submission to Atmos. Chem. Phys., 2020.

1584 McKenna, D. S., Konopka, P., Grooss, J. U., Günther, G., Müller, R., Spang, R., Offermann, D., and
1585 Orsolini, Y.: A new Chemical Lagrangian Model of the Stratosphere (CLaMS) - 1. Formulation of
1586 advection and mixing, J Geophys Res-Atmos, 107, Artn 430910.1029/2000jd000114, 2002.

1587 Merikanto, J., Spracklen, D. V., Mann, G. W., Pickering, S. J., and Carslaw, K. S.: Impact of nucleation
1588 on global CCN, Atmos Chem Phys, 9, 8601-8616, 10.5194/acp-9-8601-2009, 2009.

https://doi.org/10.5194/acp-2020-1158
Preprint. Discussion started: 2 December 2020

1589 Metzger, A., Verheggen, B., Dommen, J., Duplissy, J., Prevot, A. S. H., Weingartner, E., Riipinen, I.,
1590 Kulmala, M., Spracklen, D. V., Carslaw, K. S., and Baltensperger, U.: Evidence for the role of
1591 organics in aerosol particle formation under atmospheric conditions, P Natl Acad Sci USA, 107,
1592 6646-6651, 10.1073/pnas.0911330107, 2010.

1593 Müller, S., Hoor, P., Bozem, H., Gute, E., Vogel, B., Zahn, A., Bönisch, H., Keber, T., Krämer, M., Rolf,
1594 C., Riese, M., Schlager, H., and Engel, A.: Impact of the Asian monsoon on the extratropical lower
1595 stratosphere: trace gas observations during TACTS over Europe 2012, Atmos Chem Phys, 16,
1596 10573-10589, 10.5194/acp-16-10573-2016, 2016.

1597 Murphy, D. M., Thomson, D. S., and Mahoney, T. M. J.: In situ measurements of organics,
1598 meteoritic material, mercury, and other elements in aerosols at 5 to 19 kilometers, Science, 282,
1599 1664-1669, DOI 10.1126/science.282.5394.1664, 1998.

1600 Murphy, D. M., Cziczo, D. J., Froyd, K. D., Hudson, P. K., Matthew, B. M., Middlebrook, A. M., Peltier,
1601 R. E., Sullivan, A., Thomson, D. S., and Weber, R. J.: Single-particle mass spectrometry of
1602 tropospheric aerosol particles, J Geophys Res-Atmos, 111, Artn D23s32Doi
1603 10.1029/2006jd007340, 2006.

1604 Murphy, D. M., Froyd, K. D., Schwarz, J. P., and Wilson, J. C.: Observations of the chemical
1605 composition of stratospheric aerosol particles, Q J Roy Meteor Soc, 140, 1269-1278,
1606 10.1002/qj.2213, 2014.

1607 Nieminen, T., Kerminen, V. M., Petaja, T., Aalto, P. P., Arshinov, M., Asmi, E., Baltensperger, U.,
1608 Beddows, D. C. S., Beukes, J. P., Collins, D., Ding, A. J., Harrison, R. M., Henzing, B., Hooda, R., Hu,
1609 M., Horrak, U., Kivekas, N., Komsaare, K., Krejci, R., Kristensson, A., Laakso, L., Laaksonen, A.,
1610 Leaitch, W. R., Lihavainen, H., Mihalopoulos, N., Nemeth, Z., Nie, W., O'Dowd, C., Salma, I., Sellegri,
1611 K., Svenningsson, B., Swietlicki, E., Tunved, P., Ulevicius, V., Vakkari, V., Vana, M., Wiedensohler,
1612 A., Wu, Z. J., Virtanen, A., and Kulmala, M.: Global analysis of continental boundary layer new
1613 particle formation based on long-term measurements, Atmos Chem Phys, 18, 14737-14756,
1614 10.5194/acp-18-14737-2018, 2018.

1615 Pan, L. L., Honomichl, S. B., Kinnison, D. E., Abalos, M., Randel, W. J., Bergman, J. W., and Bian, J.:
1616 Transport of chemical tracers from the boundary layer to stratosphere associated with the
1617 dynamics of the Asian summer monsoon, Journal of Geophysical Research: Atmospheres, 121,
1618 14,159-114,174, 10.1002/2016jd025616, 2016.

1619 Park, M., Randel, W. J., Gettelman, A., Massie, S. T., and Jiang, J. H.: Transport above the Asian
1620 summer monsoon anticyclone inferred from Aura Microwave Limb Sounder tracers, J Geophys
1621 Res-Atmos, 112, Artn D1630910.1029/2006jd008294, 2007.

1622 Park, M., Randel, W. J., Emmons, L. K., and Livesey, N. J.: Transport pathways of carbon monoxide
1623 in the Asian summer monsoon diagnosed from Model of Ozone and Related Tracers (MOZART), J
1624 Geophys Res-Atmos, 114, Artn D0830310.1029/2008jd010621, 2009.

1625 Piani, C., Durran, D., Alexander, M. J., and Holton, J. R.: A Numerical Study of Three-Dimensional
1626 Gravity Waves Triggered by Deep Tropical Convection and Their Role in the Dynamics of the
1627 QBO, Journal of the Atmospheric Sciences, 57, 3689-3702, 10.1175/1520-
1628 0469(2000)057<3689:Ansotd>2.0.Co;2, 2000.

1629 Pisso, I., and Legras, B.: Turbulent vertical diffusivity in the sub-tropical stratosphere, Atmos.
1630 Chem. Phys., 8, 697-707, 10.5194/acp-8-697-2008, 2008.

1631 Ploeger, F., Konopka, P., Günther, G., Grooss, J. U., and Müller, R.: Impact of the vertical velocity
1632 scheme on modeling transport in the tropical tropopause layer, J Geophys Res-Atmos, 115, Artn
1633 D0330110.1029/2009jd012023, 2010.

https://doi.org/10.5194/acp-2020-1158
Preprint. Discussion started: 2 December 2020

1634 Ploeger, F., Günther, G., Konopka, P., Fueglistaler, S., Müller, R., Hoppe, C., Kunz, A., Spang, R.,
1635 Grooss, J. U., and Riese, M.: Horizontal water vapor transport in the lower stratosphere from
1636 subtropics to high latitudes during boreal summer, J Geophys Res-Atmos, 118, 8111-8127,
1637 10.1002/jgrd.50636, 2013.

1638 Ploeger, F., Gottschling, C., Griessbach, S., Grooss, J. U., Günther, G., Konopka, P., Müller, R., Riese,
1639 M., Stroh, F., Tao, M., Ungermann, J., Vogel, B., and von Hobe, M.: A potential vorticity-based
1640 determination of the transport barrier in the Asian summer monsoon anticyclone, Atmos Chem
1641 Phys, 15, 13145-13159, 10.5194/acp-15-13145-2015, 2015.

1642 Ploeger, F., Konopka, P., Walker, K., and Riese, M.: Quantifying pollution transport from the Asian
1643 monsoon anticyclone into the lower stratosphere, Atmos Chem Phys, 17, 7055-7066,
1644 10.5194/acp-17-7055-2017, 2017.

1645 Pommrich, R., Müller, R., Grooss, J. U., Konopka, P., Ploeger, F., Vogel, B., Tao, M., Hoppe, C. M.,
1646 Günther, G., Spelten, N., Hoffmann, L., Pumphrey, H. C., Viciani, S., D'Amato, F., Volk, C. M., Hoor,
1647 P., Schlager, H., and Riese, M.: Tropical troposphere to stratosphere transport of carbon
1648 monoxide and long-lived trace species in the Chemical Lagrangian Model of the Stratosphere
1649 (CLaMS), Geosci Model Dev, 7, 2895-2916, 10.5194/gmd-7-2895-2014, 2014.

1650 Randel, W. J., and Park, M.: Deep convective influence on the Asian summer monsoon anticyclone
1651 and associated tracer variability observed with Atmospheric Infrared Sounder (AIRS), J Geophys
1652 Res-Atmos, 111, Artn D1231410.1029/2005jd006490, 2006.

1653 Rosen, J. M.: The Boiling Point of Stratospheric Aerosols, J Appl Meteorol, 10, 1044-1046,
1654 10.1175/1520-0450(1971)010<1044:tbposa>2.0.co;2, 1971.

1655 Sahyoun, M., Freney, E., Brito, J., Duplissy, J., Gouhier, M., Colomb, A., Dupuy, R., Bourianne, T.,
1656 Nowak, J. B., Yan, C., Petäjä, T., Kulmala, M., Schwarzenboeck, A., Planche, C., and Sellegri, K.:
1657 Evidence of New Particle Formation Within Etna and Stromboli Volcanic Plumes and Its
1658 Parameterization From Airborne In Situ Measurements, Journal of Geophysical Research:
1659 Atmospheres, 124, 5650-5668, 10.1029/2018jd028882, 2019.

1660 Santee, M. L., Manney, G. L., Livesey, N. J., Schwartz, M. J., Neu, J. L., and Read, W. G.: A
1661 comprehensive overview of the climatological composition of the Asian summermonsoon
1662 anticyclone based on 10 years of Aura Microwave Limb Sounder measurements, J Geophys Res-
1663 Atmos, 122, 5491-5514, 10.1002/2016jd026408, 2017.

1664 Schneider, J., Weigel, R., Klimach, T., Dragoneas, A., Appel, O., Hünig, A., Molleker, S., Köllner, F.,
1665 Clemen, H.-C., Eppers, O., Hoppe, P., Hoor, P., Mahnke, C., Krämer, M., Rolf, C., Grooß, J.-U., Zahn,
1666 A., Obersteiner, F., Ravegnani, F., Ulanovsky, A., Schlager, H., Scheibe, M., Diskin, G. S., DiGangi, J.
1667 P., Nowak, J. B., Zöger, M., and Borrmann, S.: Aircraft-based observation of meteoric material in
1668 lower stratospheric aerosol particles between 15 and 68° N, Atmos. Chem. Phys. Discuss., in
1669 review, https://doi.org/10.5194/acp-2020-660, 2020.

1670 Schulz, J., Albert, P., Behr, H. D., Caprion, D., Deneke, H., Dewitte, S., Dürr, B., Fuchs, P., Gratzki, A.,
1671 Hechler, P., Hollmann, R., Johnston, S., Karlsson, K. G., Manninen, T., Müller, R., Reuter, M., Riihelä,
1672 A., Roebeling, R., Selbach, N., Tetzlaff, A., Thomas, W., Werscheck, M., Wolters, E., and Zelenka, A.:
1673 Operational climate monitoring from space: the EUMETSAT Satellite Application Facility on
1674 Climate Monitoring (CM-SAF), Atmos. Chem. Phys., 9, 1687-1709, 10.5194/acp-9-1687-2009,
1675 2009.

1676 Seinfeld, J. H., and Pandis, S. N.: Atmospheric chemistry and physics: from air pollution to climate
1677 change, in, Third edition. ed., John Wiley & Sons, Hoboken, New Jersey, 1 online resource, 2016.

https://doi.org/10.5194/acp-2020-1158
Preprint. Discussion started: 2 December 2020

1678 Sellegri, K., Rose, C., Marinoni, A., Lupi, A., Wiedensohler, A., Andrade, M., Bonasoni, P., and Laj, P.:
1679 New Particle Formation: A Review of Ground-Based Observations at Mountain Research
1680 Stations, Atmosphere-Basel, 10, Artn 49310.3390/Atmos10090493, 2019.

1681 Sokolov, L., and Lepuchov, B.: Protocol of interaction between Unit for Connection with Scientific
1682 Equipment (UCSE) and on-board scientific equipment of Geophysica aircraft (Second edition),
1683 Myasishchev Design Bureau (MDB), 1998.

1684 Song, I.-S., Chun, H.-Y., and Lane, T. P.: Generation Mechanisms of Convectively Forced Internal
1685 Gravity Waves and Their Propagation to the Stratosphere, Journal of the Atmospheric Sciences,
1686 60, 1960-1980, 10.1175/1520-0469(2003)060<1960:Gmocfi>2.0.Co;2, 2003.

1687 Stenke, A., Schraner, M., Rozanov, E., Egorova, T., Luo, B., and Peter, T.: The SOCOL version 3.0
1688 chemistry-climate model: description, evaluation, and implications from an advanced transport
1689 algorithm, Geosci Model Dev, 6, 1407-1427, 10.5194/gmd-6-1407-2013, 2013.

1690 Stohl, A., Forster, C., Frank, A., Seibert, P., and Wotawa, G.: Technical note: The Lagrangian
1691 particle dispersion model FLEXPART version 6.2, Atmos. Chem. Phys., 5, 2461-2474,
1692 10.5194/acp-5-2461-2005, 2005.

1693 Stroh, F., Rex, M., and the StratoClim group: First detailed airborne and balloon measurements of
1694 microphysical, dynamical, and chemical processes in the Asian Summer Monsoon Anticyclone:
1695 Overview and First Results of the 2016/2017 StratoClim field campaigns., in preparation for
1696 submission to Atmos. Chem. Phys., 2020.

1697 Thomason, L., and Peter, T.: SPARC assessment of stratospheric aerosol properties, WCRP-124,
1698 WMO/TD-No. 1295, SPARC Report, 2006.

1699 Thomason, L. W., and Vernier, J. P.: Improved SAGE II cloud/aerosol categorization and
1700 observations of the Asian tropopause aerosol layer: 1989-2005, Atmos Chem Phys, 13, 4605-
1701 4616, 10.5194/acp-13-4605-2013, 2013.

1702 Thornton, D. C., Bandy, A. R., Blomquist, B. W., Driedger, A. R., and Wade, T. P.: Sulfur dioxide
1703 distribution over the Pacific Ocean 1991-1996, J Geophys Res-Atmos, 104, 5845-5854, Doi
1704 10.1029/1998jd100048, 1999.

1705 Tissier, A. S., and Legras, B.: Convective sources of trajectories traversing the
1706 tropical tropopause layer, Atmos. Chem. Phys., 16, 3383-3398, 10.5194/acp-16-3383-2016,
1707 2016.

1708 Tzella, A., and Legras, B.: A Lagrangian view of convective sources for transport of air across the
1709 Tropical Tropopause Layer: distribution, times and the radiative influence of clouds, Atmos.
1710 Chem. Phys., 11, 12517-12534, 10.5194/acp-11-12517-2011, 2011.

1711 Venzac, H., Sellegri, K., Laj, P., Villani, P., Bonasoni, P., Marinoni, A., Cristofanelli, P., Calzolari, F.,
1712 Fuzzi, S., Decesari, S., Facchini, M. C., Vuillermoz, E., and Verza, G. P.: High frequency new particle
1713 formation in the Himalayas, P Natl Acad Sci USA, 105, 15666-15671, 10.1073/pnas.0801355105,
1714 2008.

1715 Vernier, J.-P., Fairlie, T. D., Deshler, T., Ratnam, M. V., Gadhavi, H., Kumar, B. S., Natarajan, M.,
1716 Pandit, A. K., Raj, S. T. A., Kumar, A. H., Jayaraman, A., Singh, A. K., Rastogi, N., Sinha, P. R., Kumar,
1717 S., Tiwari, S., Wegner, T., Baker, N., Vignelles, D., Stenchikov, G., Shevchenko, I., Smith, J., Bedka,
1718 K., Kesarkar, A., Singh, V., Bhate, J., Ravikiran, V., Rao, M. D., Ravindrababu, S., Patel, A., Vernier,
1719 H., Wienhold, F. G., Liu, H., Knepp, T. N., Thomason, L., Crawford, J., Ziemba, L., Moore, J.,
1720 Crumeyrolle, S., Williamson, M., Berthet, G., Jégou, F., and Renard, J.-B.: BATAL: The Balloon

https://doi.org/10.5194/acp-2020-1158
Preprint. Discussion started: 2 December 2020

Atmospheric Chemistry and Physics Discussions

1721 Measurement Campaigns of the Asian Tropopause Aerosol Layer, B Am Meteorol Soc, 99, 955-
1722 973, 10.1175/bams-d-17-0014.1, 2018.

1723 Vernier, J. P., Thomason, L. W., and Kar, J.: CALIPSO detection of an Asian tropopause aerosol
1724 layer, Geophys Res Lett, 38, Artn L0780410.1029/2010gl046614, 2011a.

1725 Vernier, J. P., Thomason, L. W., Pommereau, J. P., Bourassa, A., Pelon, J., Garnier, A., Hauchecorne,
1726 A., Blanot, L., Trepte, C., Degenstein, D., and Vargas, F.: Major influence of tropical volcanic
1727 eruptions on the stratospheric aerosol layer during the last decade, Geophys Res Lett, 38, Artn
1728 L12807Doi 10.1029/2011gl047563, 2011b.

1729 Vernier, J. P., Fairlie, T. D., Natarajan, M., Wienhold, F. G., Bian, J., Martinsson, B. G., Crumeyrolle,
1730 S., Thomason, L. W., and Bedka, K. M.: Increase in upper tropospheric and lower stratospheric
1731 aerosol levels and its potential connection with Asian pollution, J Geophys Res-Atmos, 120,
1732 1608-1619, 10.1002/2014jd022372, 2015.

1733 Viciani, S., D'Amato, F., Mazzinghi, P., Castagnoli, F., Toci, G., and Werle, P.: A cryogenically
1734 operated laser diode spectrometer for airborne measurement of stratospheric trace gases,
1735 Applied Physics B, 90, 581-592, 10.1007/s00340-007-2885-2, 2008.

1736 Viciani, S., Montori, A., Chiarugi, A., and D'Amato, F.: A Portable Quantum Cascade Laser
1737 Spectrometer for Atmospheric Measurements of Carbon Monoxide, Sensors, 18,
1738 doi:10.3390/s18072380, 2018.

1739 Vincent, R. A., and Alexander, M. J.: Gravity waves in the tropical lower stratosphere: An
1740 observational study of seasonal and interannual variability, Journal of Geophysical Research:
1741 Atmospheres, 105, 17971-17982, 10.1029/2000jd900196, 2000.

1742 Vogel, B., Günther, G., Müller, R., Grooss, J. U., Hoor, P., Krämer, M., Müller, S., Zahn, A., and Riese,
1743 M.: Fast transport from Southeast Asia boundary layer sources to northern Europe: rapid uplift
1744 in typhoons and eastward eddy shedding of the Asian monsoon anticyclone, Atmos Chem Phys,
1745 14, 12745-12762, 10.5194/acp-14-12745-2014, 2014.

1746 Vogel, B., Günther, G., Müller, R., Grooss, J. U., and Riese, M.: Impact of different Asian source
1747 regions on the composition of the Asian monsoon anticyclone and of the extratropical
1748 lowermost stratosphere, Atmos Chem Phys, 15, 13699-13716, 10.5194/acp-15-13699-2015,
1749 2015.

1750 Vogel, B., Müller, R., Günther, G., Spang, R., Hanumanthu, S., Li, D., Riese, M., and Stiller, G. P.:
1751 Lagrangian simulations of the transport of young air masses to the top of the Asian monsoon
1752 anticyclone and into the tropical pipe, Atmos Chem Phys, 19, 6007-6034, 10.5194/acp-19-6007-
1753 2019, 2019.

1754 von der Weiden, S. L., Drewnick, F., and Borrmann, S.: Particle Loss Calculator - a new software
1755 tool for the assessment of the performance of aerosol inlet systems, Atmos Meas Tech, 2, 479-
1756 494, DOI 10.5194/amt-2-479-2009, 2009.

1757 von Hobe, M., Ploeger, F., Konopka, P., Kloss, C., Ulanowski, A., Yushkov, V., Ravegnani, F., Volk, C.
1758 M., Pan, L. L., Honomichl, S. B., Tilmes, S., Kinnison, D. E., Garcia, R. R., and Wright, J. S.: Upward
1759 transport into and within the Asian monsoon anticyclone as inferred from StratoClim trace gas
1760 observations, Atmos. Chem. Phys. Discuss., 2020, 1-31, 10.5194/acp-2020-891, 2020.

1761 Wang, M., Kong, W., Marten, R., He, X.-C., Chen, D., Pfeifer, J., Heitto, A., Kontkanen, J., Dada, L.,
1762 Kürten, A., Yli-Juuti, T., Manninen, H. E., Amanatidis, S., Amorim, A., Baalbaki, R., Baccarini, A.,
1763 Bell, D. M., Bertozzi, B., Bräkling, S., Brilke, S., Murillo, L. C., Chiu, R., Chu, B., De Menezes, L.-P.,
1764 Duplissy, J., Finkenzeller, H., Carracedo, L. G., Granzin, M., Guida, R., Hansel, A., Hofbauer, V.,

https://doi.org/10.5194/acp-2020-1158
Preprint. Discussion started: 2 December 2020

Atmospheric Chemistry and Physics Discussions

1765 Krechmer, J., Lehtipalo, K., Lamkaddam, H., Lampimäki, M., Lee, C. P., Makhmutov, V., Marie, G.,
1766 Mathot, S., Mauldin, R. L., Mentler, B., Müller, T., Onnela, A., Partoll, E., Petäjä, T., Philippov, M.,
1767 Pospisilova, V., Ranjithkumar, A., Rissanen, M., Rörup, B., Scholz, W., Shen, J., Simon, M., Sipilä, M.,
1768 Steiner, G., Stolzenburg, D., Tham, Y. J., Tomé, A., Wagner, A. C., Wang, D. S., Wang, Y., Weber, S. K.,
1769 Winkler, P. M., Wlasits, P. J., Wu, Y., Xiao, M., Ye, Q., Zauner-Wieczorek, M., Zhou, X., Volkamer, R.,
1770 Riipinen, I., Dommen, J., Curtius, J., Baltensperger, U., Kulmala, M., Worsnop, D. R., Kirkby, J.,
1771 Seinfeld, J. H., El-Haddad, I., Flagan, R. C., and Donahue, N. M.: Rapid growth of new atmospheric
1772 particles by nitric acid and ammonia condensation, Nature, 581, 184-189, 10.1038/s41586-020-
1773 2270-4, 2020.

1774 Wehner, B., Werner, F., Ditas, F., Shaw, R. A., Kulmala, M., and Siebert, H.: Observations of new
1775 particle formation in enhanced UV irradiance zones near cumulus clouds, Atmos Chem Phys, 15,
1776 11701-11711, 10.5194/acp-15-11701-2015, 2015.

1777 Weigel, R., Hermann, M., Curtius, J., Voigt, C., Walter, S., Bottger, T., Lepukhov, B., Belyaev, G., and
1778 Borrmann, S.: Experimental characterization of the COndensation PArticle counting System for
1779 high altitude aircraft-borne application, Atmos Meas Tech, 2, 243-258,
1780 https://doi.org/10.5194/amt-2-243-2009, 2009.

1781 Weigel, R., Borrmann, S., Kazil, J., Minikin, A., Stohl, A., Wilson, J. C., Reeves, J. M., Kunkel, D., de
1782 Reus, M., Frey, W., Lovejoy, E. R., Volk, C. M., Viciani, S., D'Amato, F., Schiller, C., Peter, T., Schlager,
1783 H., Cairo, F., Law, K. S., Shur, G. N., Belyaev, G. V., and Curtius, J.: In situ observations of new
1784 particle formation in the tropical upper troposphere: the role of clouds and the nucleation
1785 mechanism, Atmos Chem Phys, 11, 9983-10010, 10.5194/acp-11-9983-2011, 2011.

1786 Weigel, R., Volk, C. M., Kandler, K., Hosen, E., Gunther, G., Vogel, B., Grooss, J. U., Khaykin, S.,
1787 Belyaev, G. V., and Borrmann, S.: Enhancements of the refractory submicron aerosol fraction in
1788 the Arctic polar vortex: feature or exception?, Atmos Chem Phys, 14, 12319-12342, DOI
1789 10.5194/acp-14-12319-2014, 2014.

1790 Weigel, R., Mahnke, C., Baumgartner, M., Krämer, M., Spichtinger, P., Spelten, N., Afchine, A., Rolf,
1791 C., Viciani, S., D'Amato, F., Tost , H., Belyaev, G. V., and Borrmann, S.: In situ observation of new
1792 particle formation inside ice clouds in the tropopause and outflow region of the Asian Monsoon
1793 Anticyclone, in preparation for submission to Atmos. Chem. Phys., 2020b.

1794 Williamson, C., Kupc, A., Wilson, J., Gesler, D. W., Reeves, J. M., Erdesz, F., McLaughlin, R., and
1795 Brock, C. A.: Fast time response measurements of particle size distributions in the 3-60 nm size
1796 range with the nucleation mode aerosol size spectrometer, Atmos Meas Tech, 11, 3491-3509,
1797 10.5194/amt-11-3491-2018, 2018.

1798 Williamson, C. J., Kupc, A., Axisa, D., Bilsback, K. R., Bui, T., Campuzano-Jost, P., Dollner, M., Froyd,
1799 K. D., Hodshire, A. L., Jimenez, J. L., Kodros, J. K., Luo, G., Murphy, D. M., Nault, B. A., Ray, E. A.,
1800 Weinzierl, B., Wilson, J. C., Yu, F., Yu, P., Pierce, J. R., and Brock, C. A.: A large source of cloud
1801 condensation nuclei from new particle formation in the tropics, Nature, 574, 399-403,
1802 10.1038/s41586-019-1638-9, 2019.

1803 WMO: Meteorology -- A three-dimensional science, WMO Bull, 134--138, 1957.

1804 WMO: International Meteorological Tables, WMO-No.188.TP97, edited by: Letestu, S., Secretariat
1805 of the World Meteorological Organization, Geneva, Switzerland, 1966.

1806 Wright, C. J., and Gille, J. C.: HIRDLS observations of gravity wave momentum fluxes over the
1807 monsoon regions, Journal of Geophysical Research: Atmospheres, 116, 10.1029/2011jd015725,
1808 2011.

https://doi.org/10.5194/acp-2020-1158
Preprint. Discussion started: 2 December 2020

Atmospheric Chemistry and Physics Discussions

1809 Yu, F. Q., Luo, G., Bates, T. S., Anderson, B., Clarke, A., Kapustin, V., Yantosca, R. M., Wang, Y. X., and
1810 Wu, S. L.: Spatial distributions of particle number concentrations in the global troposphere:
1811 Simulations, observations, and implications for nucleation mechanisms, J Geophys Res-Atmos,
1812 115, Artn D1720510.1029/2009jd013473, 2010.

1813 Yu, P., Rosenlof, K. H., Liu, S., Telg, H., Thornberry, T. D., Rollins, A. W., Portmann, R. W., Bai, Z.,
1814 Ray, E. A., Duan, Y., Pan, L. L., Toon, O. B., Bian, J., and Gao, R.-S.: Efficient transport of
1815 tropospheric aerosol into the stratosphere via the Asian summer monsoon anticyclone,
1816 Proceedings of the National Academy of Sciences, 114, 6972-6977, 10.1073/pnas.1701170114,
1817 2017.

1818 Yu, P. F., Toon, O. B., Neely, R. R., Martinsson, B. G., and Brenninkmeijer, C. A. M.: Composition and
1819 physical properties of the Asian Tropopause Aerosol Layer and the North American
1820 Tropospheric Aerosol Layer, Geophys Res Lett, 42, 2540-2546, 10.1002/2015gl063181, 2015.

1821 Zahn, A., Brenninkmeijer, C. A. M., Asman, W. A. H., Crutzen, P. J., Heinrich, G., Fischer, H.,
1822 Cuijpers, J. W. M., and van Velthoven, P. F. J.: Budgets of O-3 and CO in the upper troposphere:
1823 CARIBIC passenger aircraft results 1997-2001, J Geophys Res-Atmos, 107, Artn
1824 433710.1029/2001jd001529, 2002.

1825 Zhang, Y., McMurry, P. H., Yu, F. Q., and Jacobson, M. Z.: A comparative study of nucleation
1826 parameterizations: 1. Examination and evaluation of the formulations, J Geophys Res-Atmos,
1827 115, Artn D2021210.1029/2010jd014150, 2010.

1828

https://doi.org/10.5194/acp-2020-1158
Preprint. Discussion started: 2 December 2020

Atmospheric Chemistry and Physics Discussions

Figure captions

Figure 1: (a) Flight patterns conducted throughout the StratoClim 2017 mission over Nepal, India, and Bangladesh. (b) Regions with elevated number concentrations of ultrafine particles (N_{uf}) of sizes in the diameter range 6 nm < d_p < 15 nm as observed by means of COPAS measurements are indicated by the colour-code and by symbol size along the fight tracks.

Figure 2: Synopsis of vertical profiles of the total number concentration (median with 10th, 25th, 75th, 90th, and 99th percentiles) of sub-micrometre sized particles as a function of potential temperature obtained from condensation nuclei (CN) detections over (a) Brazil (TROCCINOX, 2005), over (b) West Africa (SCOUT-AMMA, 2006) and over (c) the Indian subcontinent (StratoClim 2017). During TROCCINOX (a) and SCOUT-AMMA (b) the number concentrations N_4 at lower heights (θ < 350 K) were measured aboard the DLR Falcon (cf. (Borrmann et al., 2010) and (Weigel et al., 2011)). All high-altitude measurements (θ > 350 K) and the entire StratoClim 2017 data set result from COPAS measurements. (c) The median profile of $N_{5.3}$ from repeated measurements (over the years 2004 – 2007) with the NMASS multi-channel CN counter over Central America (aboard the NASA WB-57F, data courtesy of J. C. Wilson, Denver University, 2011).

Figure 3: (a) 1-Hz-resolved particle mixing ratios n_6 and n_{10} (grey-shaded COPAS data points) with n_6 median profile from StratoClim 2017 with COPAS data from tropical regions (over Brazil, TROCCINOX 2005 and over West Africa, SCOUT-AMMA 2006, cf. (Borrmann et al., 2010)). The median profile of measurements in the tropics over the Americas (Brock et al., 1995) is added. (b) The vertical distribution of the mixing ratio of ultrafine particle ($n_{uf} = n_{6\text{-}15}$) in compliance with the NPF criterion (cf. Section 2.1.3). (c) The 1-Hz-resolved mixing ratio of non-volatile particles (i.e. thermostable at ~ 270°C) from COPAS measurements throughout StratoClim 2017 with corresponding median profile, including 25th and 75th percentile. Herein, the n_6 median profile is recalled for comparison from Panel a. (d) The fraction f ($= n_{10}\text{nv}/n_{10} \cdot 100$) of non-volatile particles with median, and with 25th and 75th percentiles. Median data points are connected with lines to guide the reader's eyes.

Figure 4: Frequency distribution of the duration of observed NPF events (cf. Section 2.1.3 for definition) throughout the StratoClim 2017 mission. (a) The general view, (b) the close up views of the shortest events, and (c) of the least frequent events.

Figure 5: (a) Diurnal variation of the occurrence frequency of NPF events (cf. Section 2.1.3 for definition). (b) The diurnal distribution of NPF events' mean particle mixing ratio $\overline{n_{uf}}$ with standard deviation σ, coloured by flight date, and (c) in colours of the (logarithmic) duration of respective event. Note, the mean horizontal distance is derived from the event duration based on a mean flight speed of 154 m s^{-1} (σ = ± 39 m s^{-1}, variable flight attitude remains unconsidered) and is understood as equivalent horizontal extension of a NPF event.

Figure 6: Mean particle mixing ratio $\overline{n_{uf}}$ of individual NPF events as function of (left column) the vertical distance from the mean lapse-rate tropopause ($\overline{\Delta\theta}$), and of (right column) the equivalent latitude (90° represents the centre of the AMA as projected to polar coordinates). Data points are coloured by flight date (Panels a and b) and by CO mixing ratios (Panels c and d). (e) The mean particle mixing ratio $\overline{n_{uf}}$ as function of the equivalent latitude is colour-coded by the values $\overline{\Delta\theta}$ (colour scale on the left of panel (e)).

https://doi.org/10.5194/acp-2020-1158
Preprint. Discussion started: 2 December 2020

Atmospheric Chemistry and Physics Discussions

Figure 7: Results of a coagulation simulation based on the assumption of a distinct and expired burst-like event. The simulation's initial particle size distribution (black circles; horizontal bars indicate the width of each size bin) is merged from data of three COPAS detectors (for N_6, N_{10}, and N_{15}) and of the UHSAS-A (65 nm < d_p < 1 µm) as detected during NPF encountered on 04 August 2017, between 04:04:40 and 04:05:06 UTC. (a): The processing particle size distribution (coloured lines) over several hours. (b): The concentration of ultrafine particles (N_{uf}) over the simulation's run time and its fractional contribution to the total particle number concentration (N_{total}). Furthermore, the simulated decay of variably multiplied N_{uf} (by factors 0.1, 10, and 100) as initial input of the simulation under constant background conditions (dashed lines).

Figure 8: Particle mixing ratio of fine-mode particles n_6 (grey dots in the background) and of ultrafine particles n_{uf} (colour-coded with reference to the potential temperature) in relationship to the CO mixing ratio. The median n_{uf} with the 25th and 75th percentile is shown in bin widths of 2.5 nmol mol^{-1} of the CO mixing ratio (black dots), which are connected by lines to guide the eyes of the reader.

Figure 9: Upper panels: geographic position of the last boundary layer (BL) contact of the NPF-connected air mass backward trajectories. Bottom panels: geographic position of the maximum ascent rate of these trajectories. By means of the chemistry transport model ClaMS and based on ERA-5 data the backward trajectories were analysed over the last 50 days prior to the NPF detection as starting point of each trajectory. Points are coloured with reference to the (logarithmic) mixing ratio n_{uf} of ultrafine particles (Panels a and b) or to the air mass transport time since the last BL contact (Panels c and d), grey data points indicate transport times > 25 days.

Figure 10: Vertical profile of the 1-Hz-resolved particle mixing ratio of ultrafine particles n_{uf} colour-coded by the air mass transport time (days) from the boundary layer (BL). By means of the chemistry transport model CLaMS and based on ERA-5 data the backward trajectories were analysed over the last 50 days prior to the NPF detection as starting point of each trajectory, grey data points indicate transport times > 25 days.

Figure 11: Vertical profile of the event-wise mean particle mixing ratio of ultrafine particles $\overline{n_{uf}}$ with standard deviation σ (bars) as a function of the mean potential temperature (± σ). (a) The data points are colour-coded by the proportion of convective contribution to the air sample. (b) The data points are coloured by the time (days) since the release of the air mass at the top of a convective cell.

Figure 12: Time series of data sampled during a section of a StratoClim 2017 flight (KTM 6) on 06 August 2017. Except the manoeuvre period between 09:20 and 09:30 (UTC), a strictly constant altitude and pressure level (Panel a) were maintained. Particle mixing ratios n_6, n_{10} and n_{15} and n_{10}nv (Panel b), the mixing ratio of the ultrafine particles n_{uf} (Panel c), the CO mixing ratio (Panel d), the ambient air temperature (T_{amb}), and the temperature fluctuation (T_{amb} - T_{mean}) (Panel e) feature different characteristics and sequence during two NPF phases (oblique hatched areas).

https://doi.org/10.5194/acp-2020-1158
Preprint. Discussion started: 2 December 2020

Atmospheric Chemistry and Physics Discussions

Figures

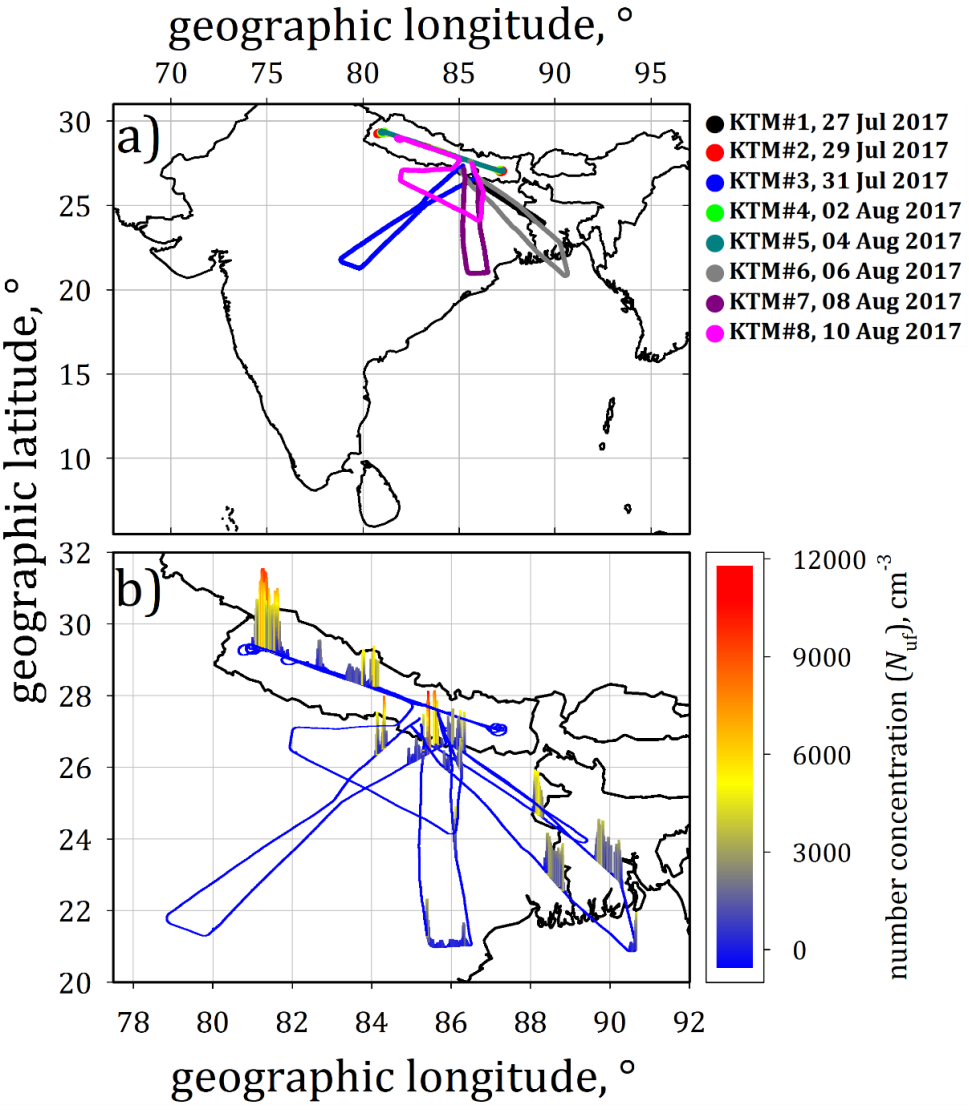

Figure 1

https://doi.org/10.5194/acp-2020-1158
Preprint. Discussion started: 2 December 2020

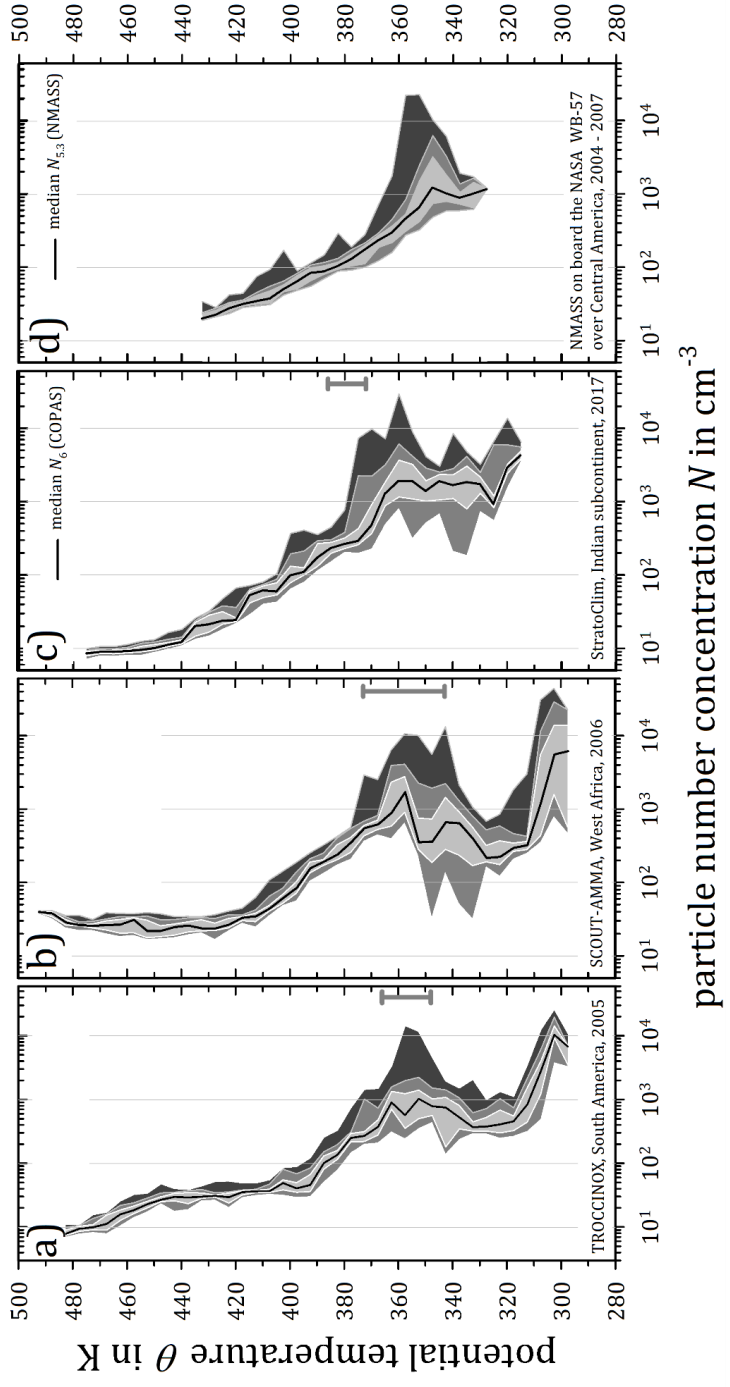

Figure 2

https://doi.org/10.5194/acp-2020-1158
Preprint. Discussion started: 2 December 2020

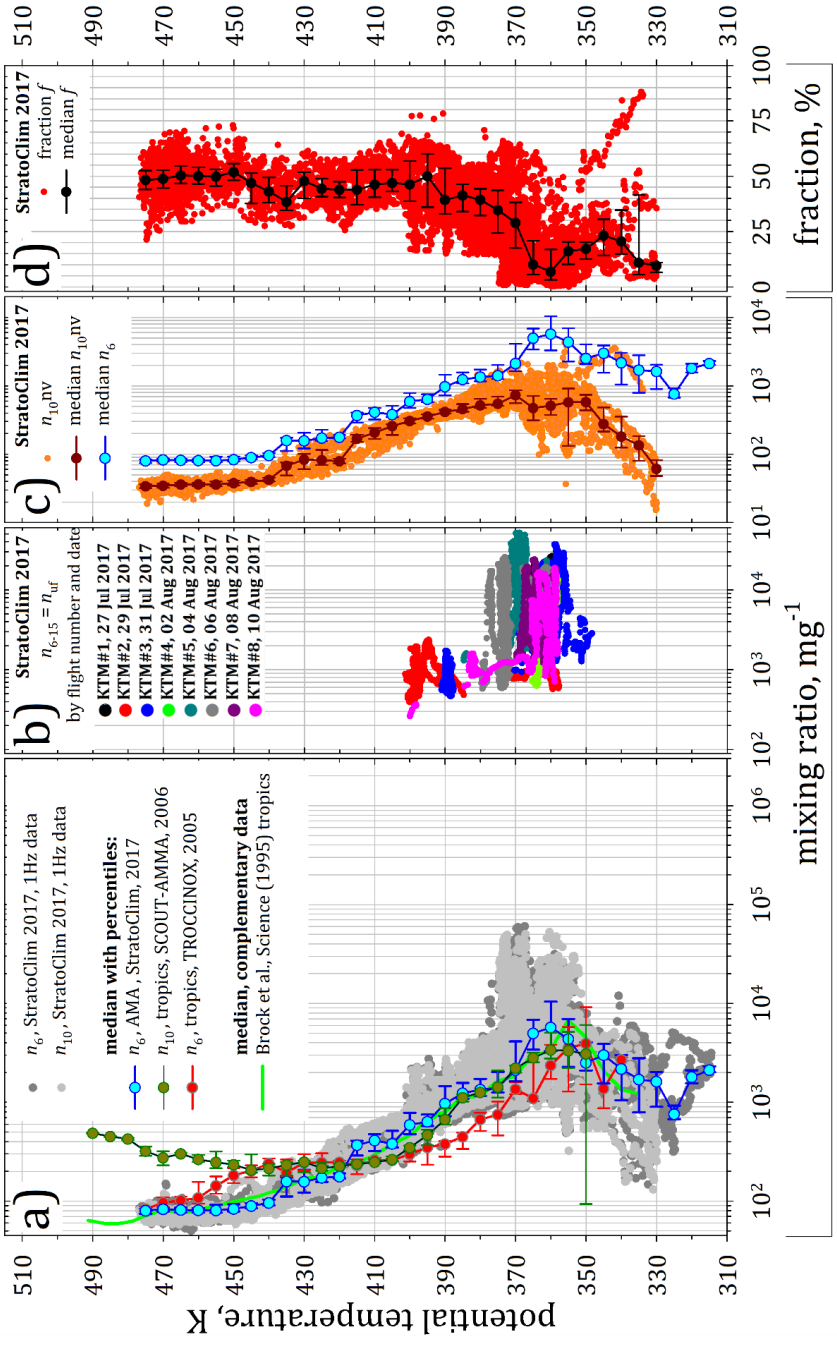

Figure 3

https://doi.org/10.5194/acp-2020-1158
Preprint. Discussion started: 2 December 2020

Atmospheric Chemistry and Physics Discussions

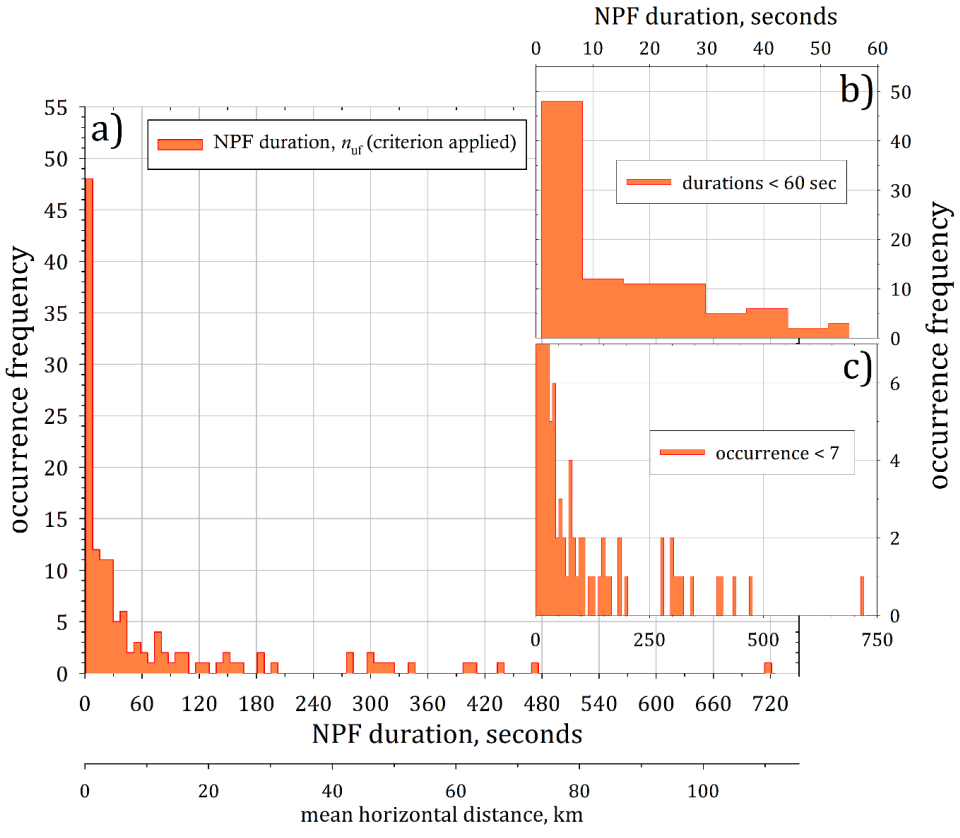

Figure 4

https://doi.org/10.5194/acp-2020-1158
Preprint. Discussion started: 2 December 2020

Atmospheric Chemistry and Physics Discussions

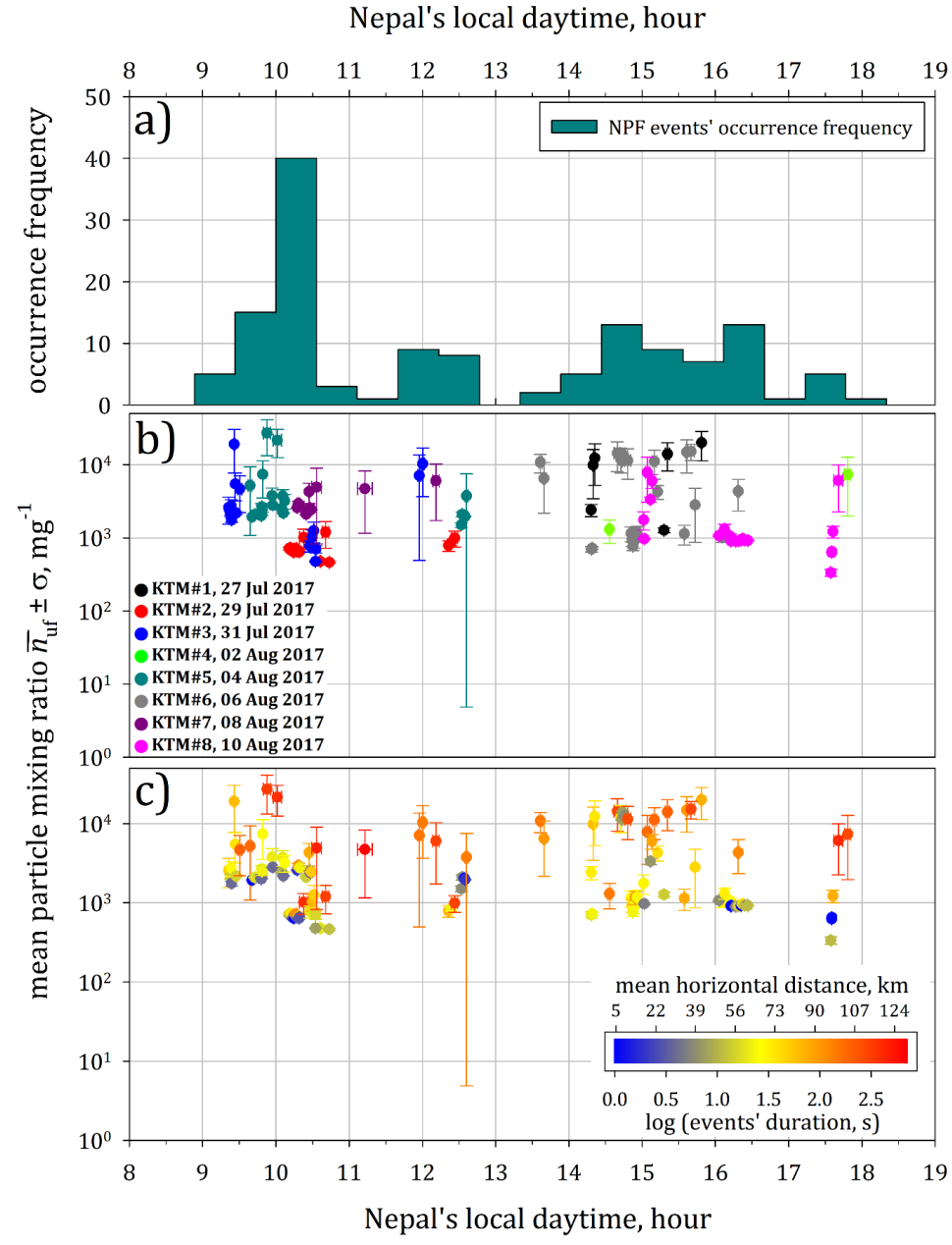

Figure 5

https://doi.org/10.5194/acp-2020-1158
Preprint. Discussion started: 2 December 2020

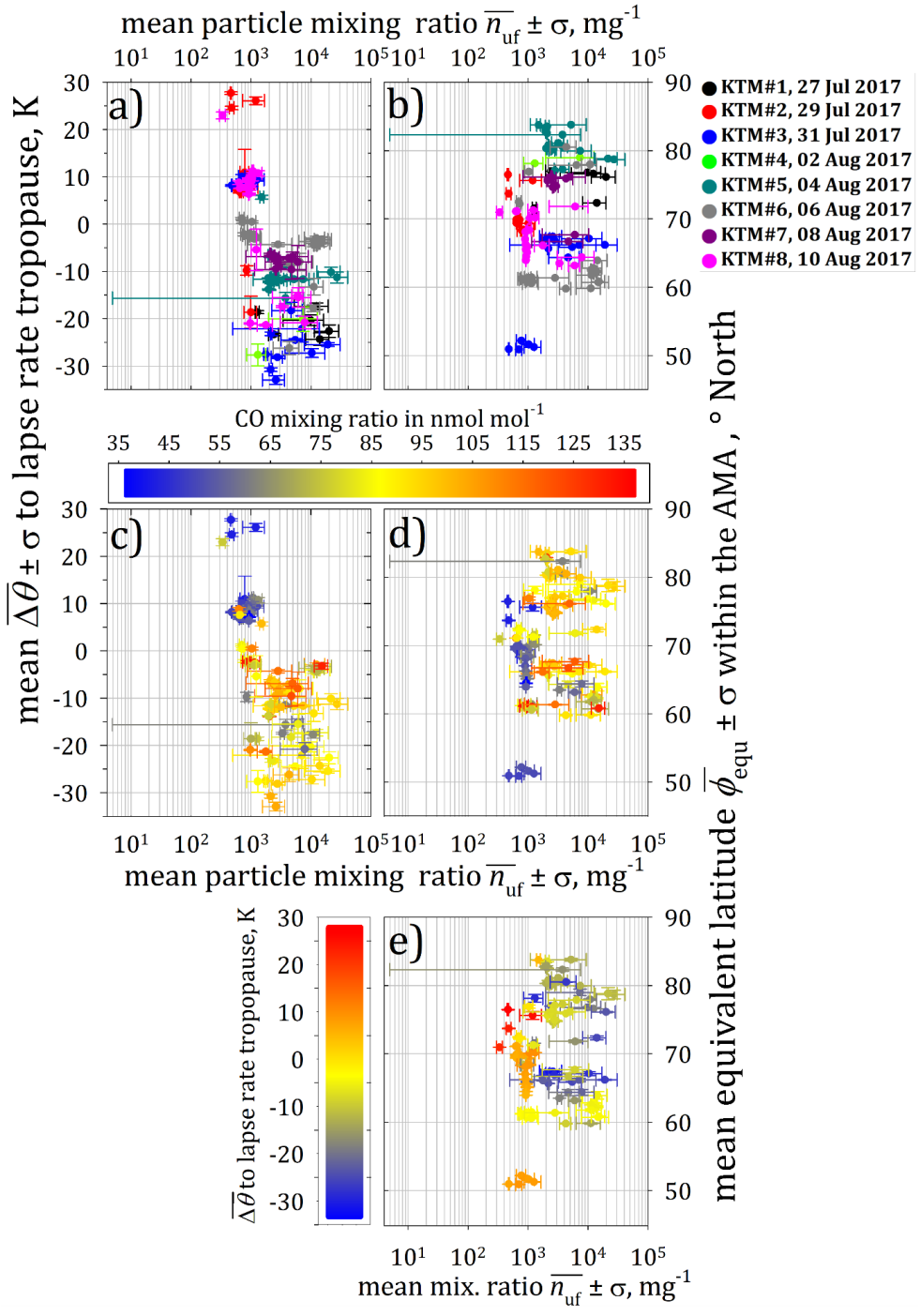

Figure 6

https://doi.org/10.5194/acp-2020-1158
Preprint. Discussion started: 2 December 2020

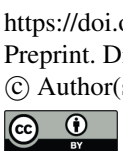

Atmospheric Chemistry and Physics Discussions

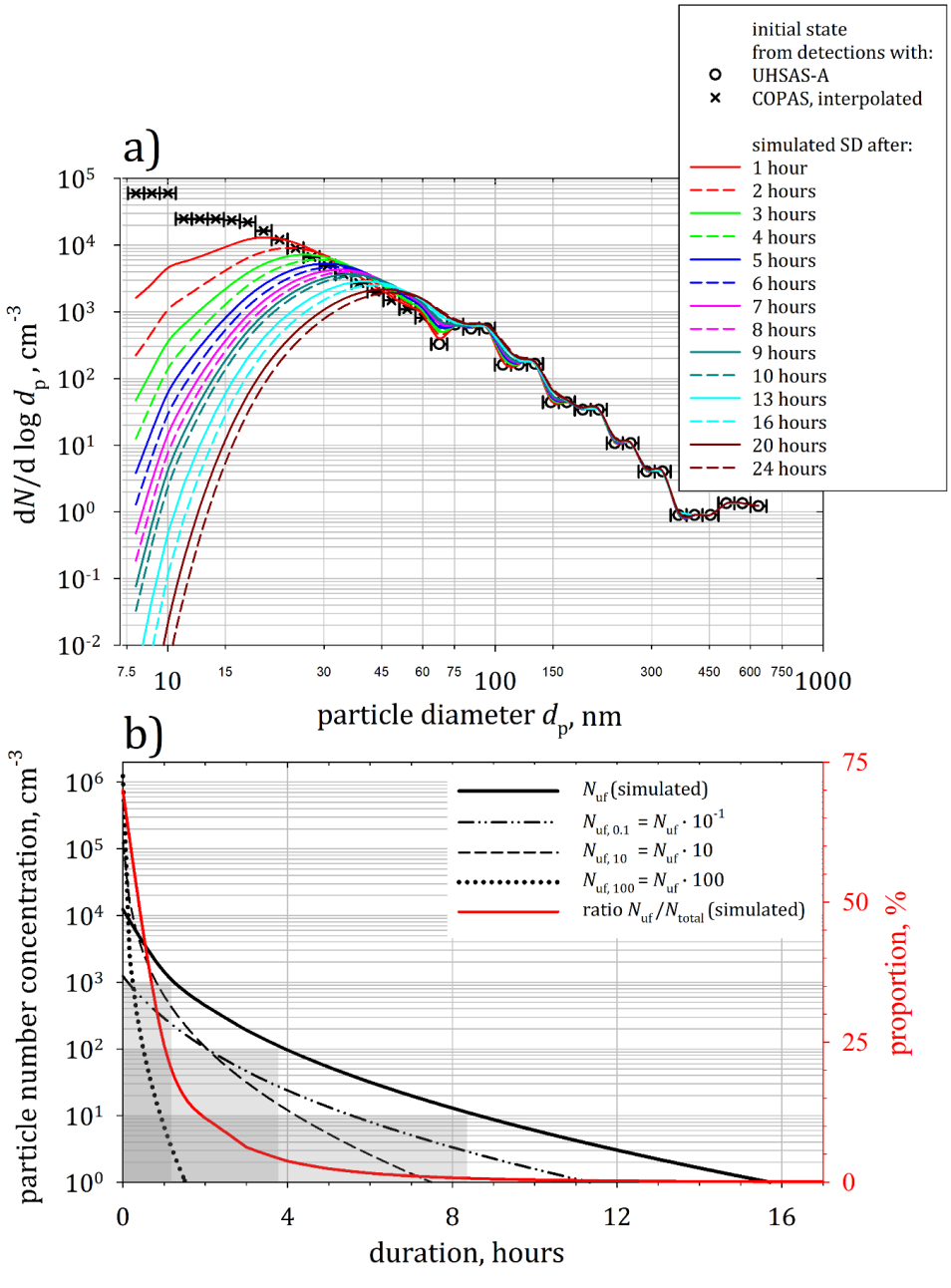

Figure 7

https://doi.org/10.5194/acp-2020-1158
Preprint. Discussion started: 2 December 2020

Atmospheric Chemistry and Physics Discussions

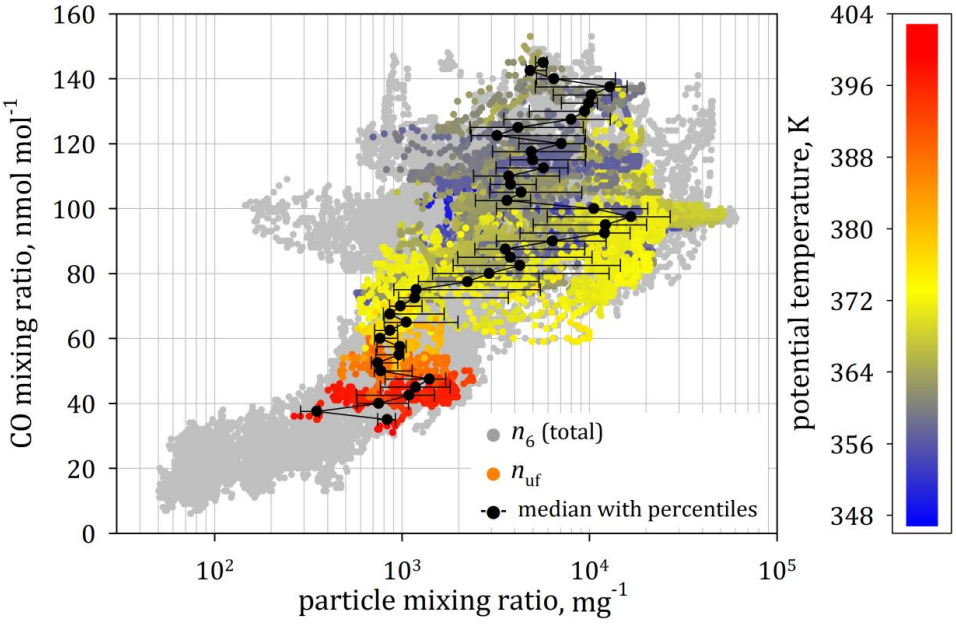

Figure 8

https://doi.org/10.5194/acp-2020-1158
Preprint. Discussion started: 2 December 2020

Atmospheric Chemistry and Physics Discussions

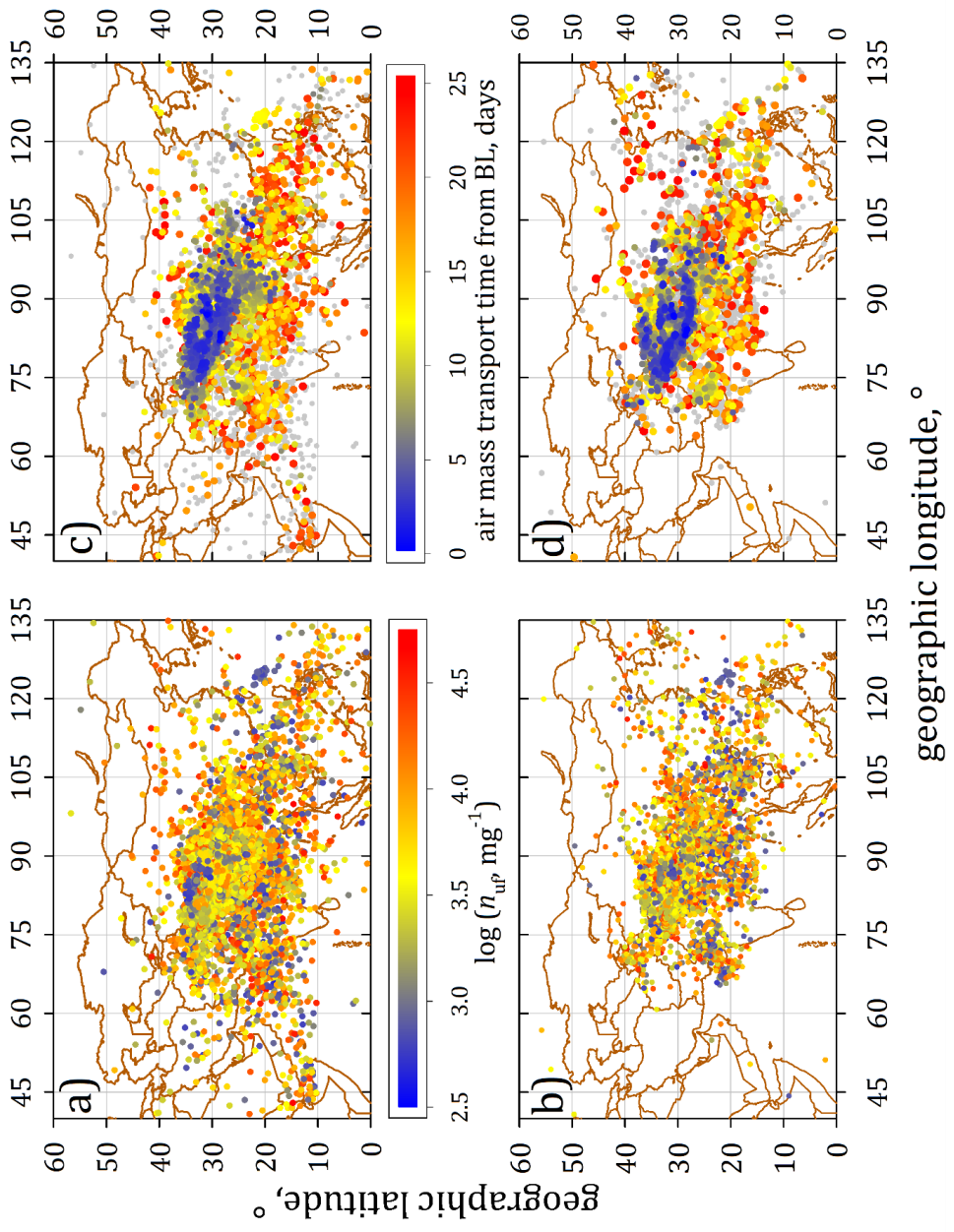

Figure 9

https://doi.org/10.5194/acp-2020-1158
Preprint. Discussion started: 2 December 2020

Atmospheric Chemistry and Physics Discussions

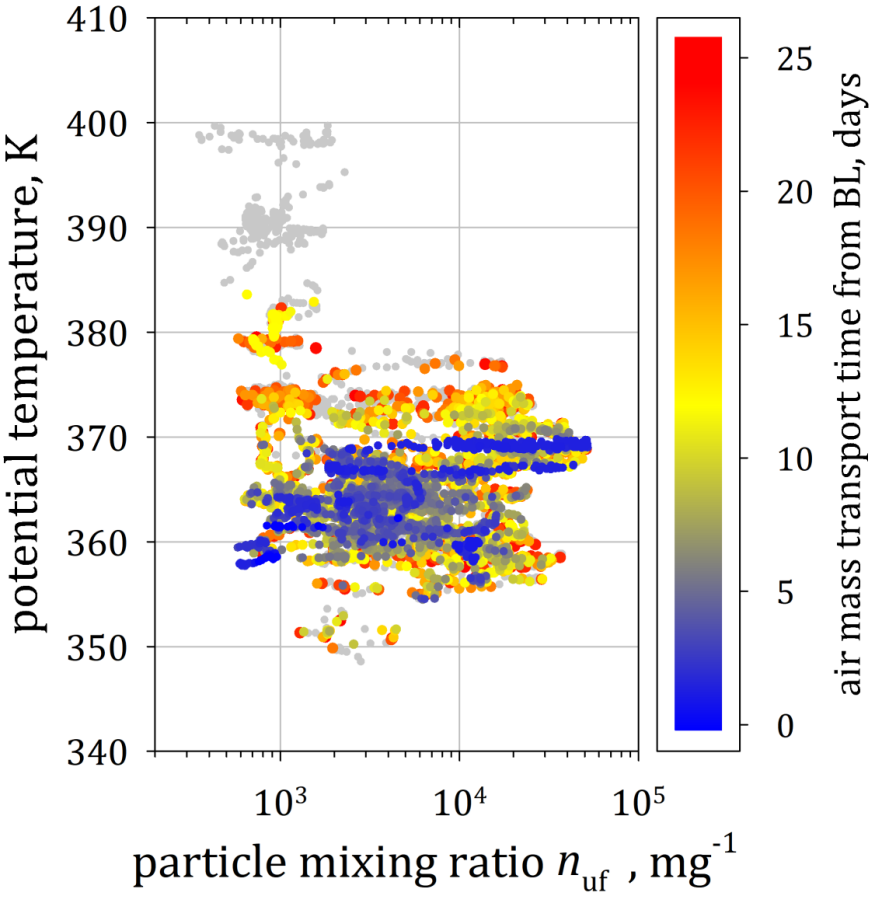

Figure 10

https://doi.org/10.5194/acp-2020-1158
Preprint. Discussion started: 2 December 2020

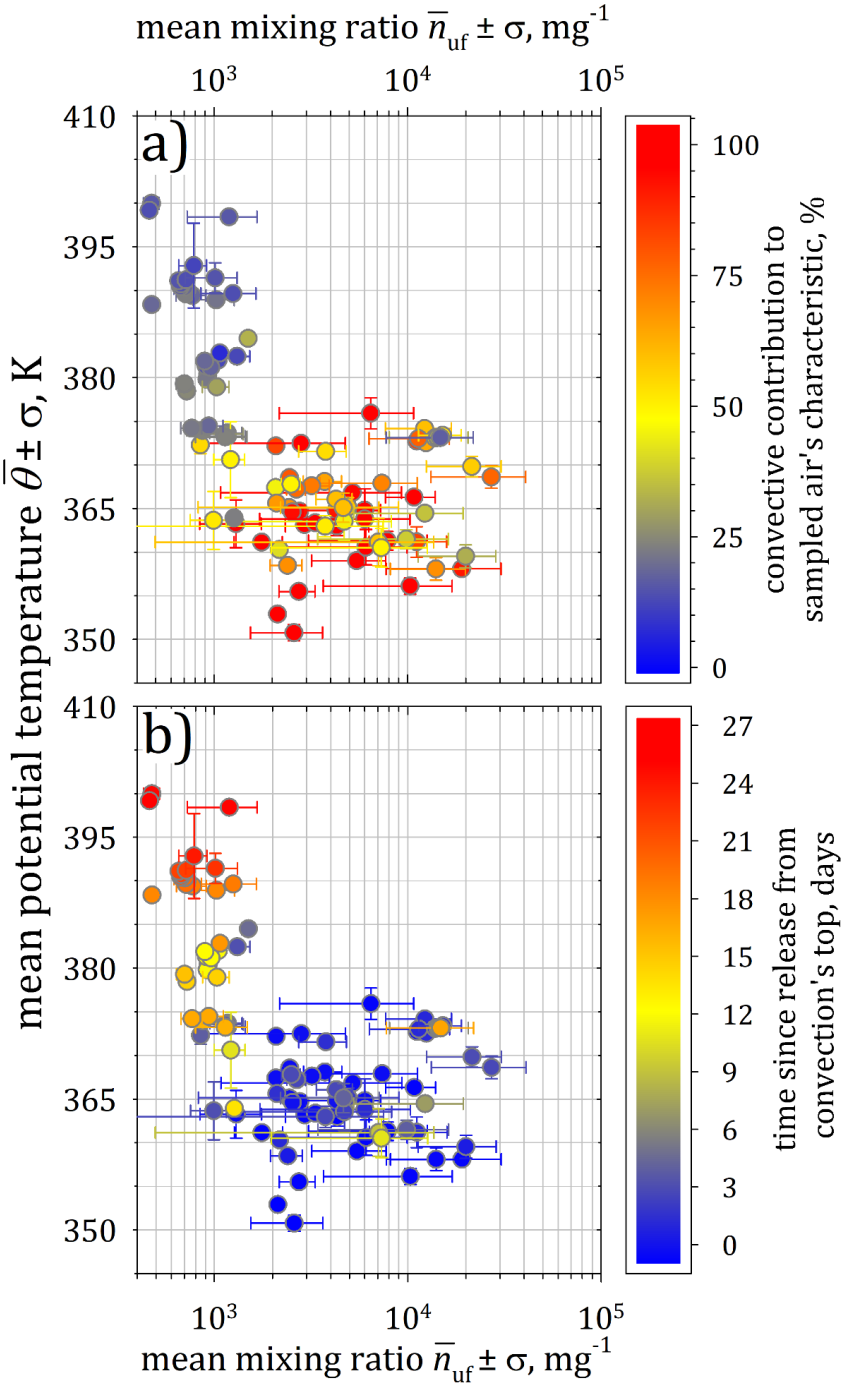

Figure 11

https://doi.org/10.5194/acp-2020-1158
Preprint. Discussion started: 2 December 2020

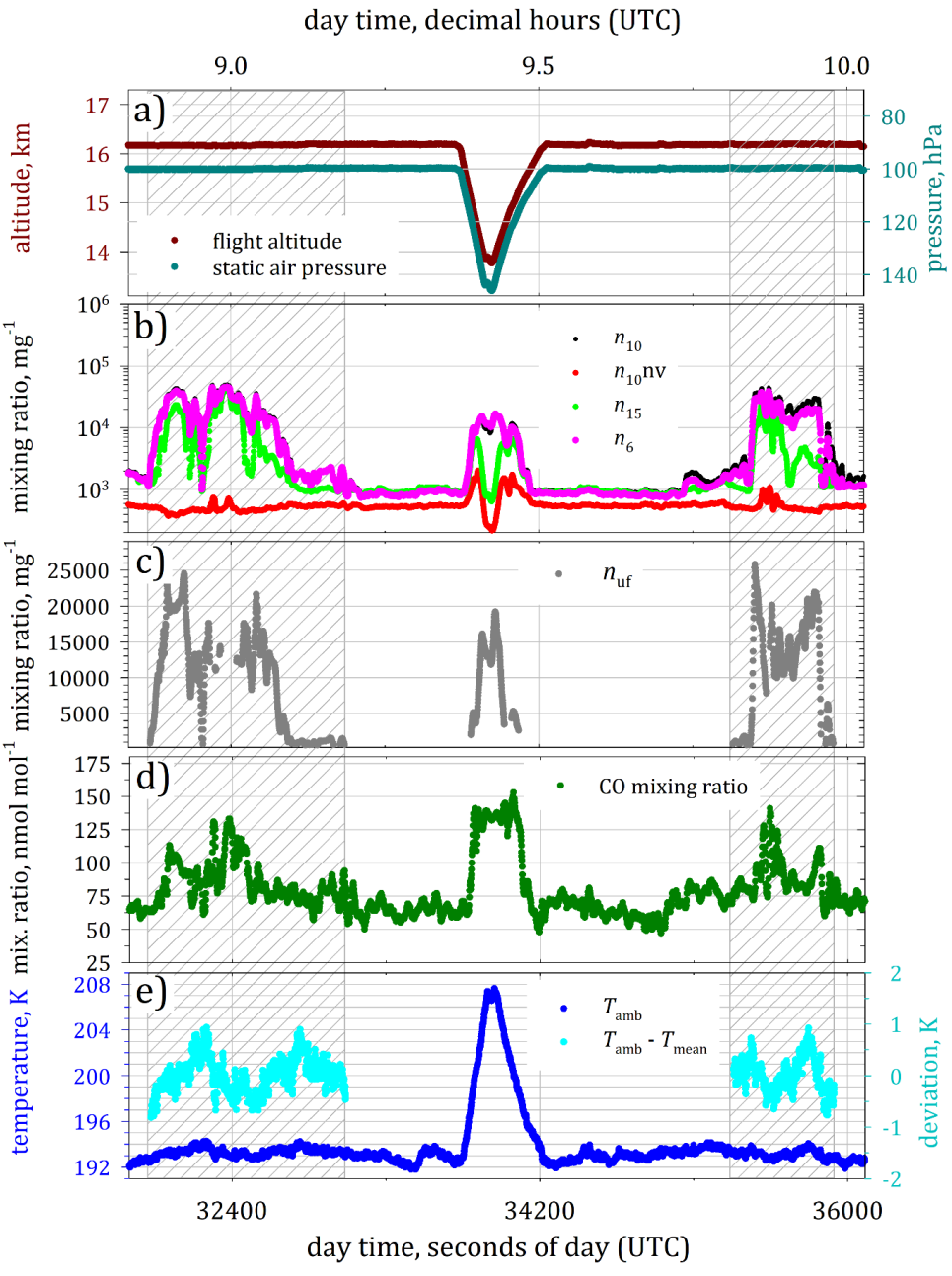

Figure 12

https://doi.org/10.5194/acp-2020-1158
Preprint. Discussion started: 2 December 2020

Atmospheric Chemistry and Physics Discussions

Tables

pressure, hPa	particle diameter, nm										$\bar{\Lambda}_{6\text{-}15}$, %	κ_L (dimensionless)
	6	7	8	9	10	11	12	13	14	15		
	particle size dependent transmission efficiency, %											
80	60	65	70	74	77	79	81	82.5	84	85	**24.25**	1.32
150	70	75	77.5	81	83	84.5	86.5	87.5	88.5	89	**17.75**	1.22
300	77.5	81.5	84	86.5	88	89.5	90.5	91.5	92	92.5	**12.65**	1.14
400	80	83	85	87.5	89	90.5	91.5	92	92.8	93.5	**11.52**	1.13

Table 1

Re-calculated pressure-dependent corrections κ_L for number concentrations of ultrafine particles due to particle losses ($\bar{\Lambda}_{6\text{-}15}$) in the aerosol line configuration (both COPAS instruments attached to a single aerosol inlet) as deployed during StratoClim 2017, by using the Particle Loss Calculator (von der Weiden et al., 2009) modified for low pressure applications. $\kappa_L = 100/(100-\bar{\Lambda}_{6\text{-}15})$, correspondingly to Weigel et al. (2009).